

# Pulse Design for Two-Qubit Gates in Superconducting Circuits

By

Qi Ding

B.E., Xi'an Jiaotong University (2020)

Submitted to the Department of Electrical Engineering and Computer Science in Partial  
Fulfillment of the Requirements for the Degree of

Master of Science

at the

MASSACHUSETTS INSTITUTE OF TECHNOLOGY

JUNE 2023

©2023 Qi Ding. All rights reserved.

The author hereby grants to MIT a nonexclusive, worldwide, irrevocable, royalty-free license to exercise any and all rights under copyright, including to reproduce, preserve, distribute and publicly display copies of the thesis, or release the thesis under an open-access license.

Authored by: Qi Ding  
Department of Electrical Engineering and Computer Science  
May 19, 2023

Certified by: William D. Oliver  
Henry Ellis Warren (1894) Professor of Electrical Engineering and  
Computer Science  
Professor of Physics  
Thesis Supervisor

Certified by: Alan V. Oppenheim  
Ford Professor of Engineering  
Professor of Electrical Engineering and Computer Science  
Thesis Supervisor

Accepted by: Leslie A. Kolodziejski  
Professor of Electrical Engineering and Computer Science  
Chair, Department Committee on Graduate Students

# Pulse Design for Two-Qubit Gates in Superconducting Circuits

by

Qi Ding

Submitted to the Department of Electrical Engineering and Computer Science  
on May 19, 2023, in partial fulfillment of the  
requirements for the degree of  
Master of Science in Electrical Engineering and Computer Science

## Abstract

Despite tremendous progress towards achieving low error rates with superconducting qubits, error-prone two-qubit gates remain a bottleneck in realizing large-scale quantum computers. To boost the two-qubit gate fidelity to the highest attainable levels given limited coherence time, it is essential to develop a systematic framework to optimize protocols for implementing two-qubit gates. In this thesis, we formulate the design of the control trajectory for baseband controlled phase gates in superconducting circuits into a pulse design problem. Our research indicates that the Chebyshev trajectories – the trajectories based on the Chebyshev pulse and weighted Chebyshev approximation – have the potential to outperform the Slepian trajectories based on the Slepian pulse, which are currently widely used in quantum experiments.

Thesis Supervisor: William D. Oliver

Title: Henry Ellis Warren (1894) Professor of Electrical Engineering and Computer Science

Professor of Physics

Thesis Supervisor: Alan V. Oppenheim

Title: Ford Professor of Engineering

Professor of Electrical Engineering and Computer Science

# Acknowledgments

I am immensely grateful for the support and guidance that I have received throughout my research journey. First and foremost, I would like to express my deepest appreciation to my co-supervisors, Professor William D. Oliver and Professor Alan V. Oppenheim, for their unwavering dedication, mentorship, and guidance. Their exceptional knowledge and expertise have been invaluable in shaping the direction and scope of this thesis. Their constructive criticism, thoughtful feedback, and thorough review of my work have challenged me to think critically and approach the research with a deeper understanding. And above all, their kindness, patience, and confidence in me, not just as a graduate student, but also as a true friend, are indispensable.

I am always grateful to my close colleagues and collaborators, Dr. Thomas A. Baran, Dr. Petros T. Boufounos, Dr. Simon Gustavsson, for all the discussions we had throughout the development of the thesis. Their advice in terms of the conceptual ideas and technical content is significant and has greatly contributed to the quality of this work. I would also like to extend my heartfelt thanks to the members of Quantum Mechanics & Signal Processing (QMSP) discussion group, including Professor Isaac L. Chuang, Professor William D. Oliver, Professor Alan V. Oppenheim, Professor Tess E. Smidt, Dr. Thomas A. Baran, Dr. Petros T. Boufounos, Dr. Alex (Ami) Greene, Dr. Catherine A. Lockton (Medlock), Dr. Roni Winik, for the fruitful and interesting discussions, which in part led to the beginning of the thesis. Special thanks are extended to Dr. Youngkyu Sung, who has taught me a great deal about quantum physics and experiments, and especially simulations which contribute to the major part of this work. I am also thankful to the members of the Digital Signal Processing Group (DSPG) and the Engineering Quantum Systems Group (EQuS) at MIT, for useful discussions, encouraging comments, and enjoyable moments. Also thanks to Dr. Chris Featherman who has helped in improving the writing of this thesis.

Last but not least, I am greatly appreciative of my family, partner and friends, who have been a constant source of unconditional love, belief, and support throughout my research journey. I am deeply grateful for their presence in my life.

# Contents

<b>1</b>	<b>Introduction</b>	<b>15</b>
1.1	Introduction to quantum computing . . . . .	15
1.2	Introduction to pulse design . . . . .	16
1.3	Thesis overview . . . . .	16
<b>2</b>	<b>Finite-length Discrete-time Pulses</b>	<b>18</b>
2.1	Definition and notation . . . . .	18
2.2	Examples of common finite-length discrete-time pulses . . . . .	19
2.2.1	Rectangular pulse . . . . .	19
2.2.2	Raised cosine pulse . . . . .	20
2.2.3	Slepian pulse . . . . .	22
2.2.4	Kaiser pulse . . . . .	25
2.2.5	Chebyshev pulse I . . . . .	26
2.3	Pulses based on weighted Chebyshev approximation . . . . .	29
2.3.1	Weighted Chebyshev approximation . . . . .	29
2.3.2	Chebyshev pulse II . . . . .	33
<b>3</b>	<b>Two-Qubit Gates in Superconducting Circuits</b>	<b>34</b>
3.1	Qubits . . . . .	34
3.2	Superconducting qubits . . . . .	38
3.2.1	Quantum LC circuit . . . . .	38
3.2.2	Josephson junction . . . . .	42

3.2.3	Transmon qubit . . . . .	43
3.3	Quantum gates . . . . .	46
3.3.1	Single-qubit gates . . . . .	46
3.3.2	Two-qubit gates . . . . .	47
3.3.3	Universal gate set . . . . .	47
3.4	The CPHASE gate in tunable transmon qubits . . . . .	48
3.5	Review of efforts on control trajectory design . . . . .	52
<b>4</b>	<b>Problem Formulation and Optimality Criterion</b>	<b>53</b>
4.1	A two-level system abstraction . . . . .	53
4.2	A formula for the accumulated phase . . . . .	56
4.3	A formula for the leakage error . . . . .	56
4.3.1	Geometric approach . . . . .	57
4.3.2	Analytical approach . . . . .	59
4.3.3	Relationship to the Landau-Zener formula . . . . .	63
4.4	Two scenarios . . . . .	64
4.4.1	Type-I process: Move through the avoided crossing . . . . .	65
4.4.2	Type-II process: Return from the avoided crossing . . . . .	66
4.5	Problem formulation . . . . .	66
4.5.1	Nomenclature . . . . .	66
4.5.2	Intuitive formulation: optimization over duration . . . . .	67
4.5.3	Time-frequency transformation: optimization over frequency . . . . .	69
4.5.4	Continuous time to discrete time transformation . . . . .	70
<b>5</b>	<b>Optimal Solutions and Comparisons</b>	<b>72</b>
5.1	Control trajectories based on some common finite-length discrete-time pulses . . . . .	72
5.2	Two scenarios . . . . .	73
5.2.1	Type-I process: Move through the avoided crossing . . . . .	74
5.2.2	Type-II process: Return from the avoided crossing . . . . .	76

5.3	Summary and discussion . . . . .	79
<b>6</b>	<b>Time-domain Simulation Using QuTiP</b>	<b>80</b>
6.1	Setting and procedure . . . . .	81
6.2	Simulation results . . . . .	84
6.2.1	Comparison example 1 . . . . .	87
6.2.2	Comparison example 2 . . . . .	89
6.2.3	More comparison examples . . . . .	89
6.3	Summary and discussion . . . . .	91
<b>7</b>	<b>Concluding Remarks and Future Work</b>	<b>93</b>
<b>A</b>	<b>Additional Simulation Results</b>	<b>95</b>

# List of Figures

2-1	Time-domain and frequency-domain representations of the rectangular pulse for $N = 25$ . . . . .	20
2-2	Time-domain and frequency-domain representations of the Hann pulse, the Hamming pulse and the Blackman pulse for $N = 25$ . . . . .	21
2-3	Time-domain and frequency-domain representations of the first and second Slepian pulses for $N = 25$ and $NW = 3$ . . . . .	24
2-4	Time-domain and frequency-domain representations of the Kaiser pulse for $N = 25$ and $\beta = 8$ , and the first Slepian pulse for $N = 25$ and $NW = 3$ . The two pulses share very similar characteristics for appropriately chosen parameters since the Kaiser pulse is developed to approximate the first Slepian pulse. . . . .	25
2-5	Plots of the Chebyshev polynomials of orders $n = 0, 1, 2, 3, 4$ . . . . .	27
2-6	Time-domain and frequency-domain representations of the Chebyshev pulses for $N = 25$ and sidelobe amplitudes specified to be $-60$ dB and $-80$ dB. . . . .	28
2-7	Time-domain and frequency-domain representations of a Case 1 pulse of length $N = 25$ using weighted Chebyshev approximation (WCA) to coincide with the Chebyshev pulse I for $N = 25$ with sidelobe amplitude specified to be $-60$ dB. . . . .	32
2-8	Time-domain and frequency-domain representations of a Case 3 pulse of length $N = 25$ using weighted Chebyshev approximation, which is referred to in this thesis as the Chebyshev pulse II. . . . .	33

3-1	A classical bit v.s. a quantum bit (qubit). (a) A classical bit can be in either the “0” state or the “1” state, represented by two ends of a stick. (b) A quantum bit can be in any superposition of the state $ 0\rangle$ and the state $ 1\rangle$ , graphically represented by the Bloch vector on a sphere known as the Bloch sphere. . . . .	35
3-2	Images of four physical hardware platforms for quantum computing. (From left to right, top to bottom) Superconducting circuits, trapped ions, quantum dots, and color centers. Figure from Ref. [28]. . . . .	37
3-3	Circuit diagram of a linear LC circuit comprising a capacitor with capacitance $C$ in parallel with an inductor with inductance $L$ . . . . .	38
3-4	Energy potential and levels of a quantum LC circuit (quantum harmonic oscillator, or QHO) v.s. a transmon with a Josephson junction. The energy potential of a QHO is of a quadratic form and the energy levels are separated equidistantly. By introducing a Josephson junction, the energy potential of a transmon is reshaped into a cosinusoidal form and the energy levels are no longer equidistant. Figure from Ref. [30]. . . . .	42
3-5	A transmon qubit v.s. a flux-tunable transmon qubit. (a) Circuit diagram of a transmon qubit comprising a capacitor with capacitance $C_s$ in parallel with a Josephson junction with inductance $L_J$ and self-capacitance $C_J$ . (b) Circuit diagram of a flux-tunable transmon comprising a capacitor in parallel with a SQUID loop. The SQUID loop comprises two Josephson junctions in parallel with some external magnetic flux $\Phi_{\text{ext}}$ threading the loop. . . . .	45
3-6	Circuit diagram of a flux-tunable transmon capacitively coupled to a fixed-frequency transmon. The flux-tunable transmon is referred to as QB1 and the fixed-frequency transmon is referred to as QB2. . . . .	48

- 3-7 An example of the energy spectrum diagram of two coupled transmons as depicted in Figure 3-6 as the frequency of QB1 is detuned by changing the local magnetic flux that threads its SQUID loop. The frequency detuning  $d\omega$  of QB1 is defined as  $d\omega = \omega_{\text{ini}} - \omega_1$ , where  $\omega_{\text{ini}}$  is the initial frequency of QB1 and  $\omega_1$  is the instantaneous frequency of QB1. The avoided crossing between the states  $|11\rangle$  and  $|20\rangle$  indicated in the orange box in the left plot is used to implement the CPHASE gate. The right plot is a zoom-in plot around the avoided crossing of interest, where  $l(t)$  represents a typical trajectory of the instantaneous energy of state  $|11\rangle$  during the process of the CPHASE gate. The parameters used to generate this energy diagram are  $\omega_1 = 5.2$ ,  $\omega_2 = 4.7$ ,  $\alpha_1 = \alpha_2 = -0.3$ ,  $g = 0.033$  (GHz). . . . . 50
- 4-1 Eigenenergies of the two-level system with Hamiltonian  $H$  as a function of  $\varepsilon(t)$ . In the upper plot, the dashed lines represent the states  $|11\rangle$  and  $|20\rangle$  when they are uncoupled, i.e.,  $\Delta = 0$  (we may also refer to the states as diabatic states in this case); the solid lines represent the states  $|11\rangle$  and  $|20\rangle$  when they are coupled, i.e.,  $\Delta > 0$ . The lower plot shows an example of a typical trajectory for  $\varepsilon(t)$  to implement a CPHASE gate in the abstracted two-level system. . . . . 55
- 4-2 The geometric definition of  $\theta(t)$  and the Bloch sphere picture of an infinitesimal step of evolution. (a) A control vector  $\vec{\theta}$  representing the control variable  $\theta(t)$  in a coordinate in terms of  $\Delta$  and  $\varepsilon(t)$ . (b) An instantaneous basis vector  $|11'\rangle$  parallel to the control vector  $\vec{\theta}$ . In an infinitesimal time  $\delta t$ , the state vector  $|\psi\rangle$  deviates from the instantaneous basis vector  $|11'\rangle$  by  $-\delta\theta$  and precesses around it. . . . . 57

4-3	Type-I process v.s. Type-II process. (a) In the Type-I process, $\varepsilon(t)$ varies from $-\epsilon_0$ to $+\epsilon_1$ where $\epsilon_0 > 0$ and $\epsilon_1 > 0$ . A typical trajectory for $\varepsilon(t)$ is depicted. (b) In the Type-II process, $\varepsilon(t)$ varies from $-\epsilon_0$ to $\epsilon_2$ and return to $-\epsilon_0$ where $\epsilon_0 > 0$ and $\epsilon_2 \approx 0$ . A typical trajectory for $\varepsilon(t)$ is depicted. . . . .	65
5-1	Frequency-domain representations of the rectangular trajectory, the Blackman trajectory, the Kaiser trajectory, the first Slepian trajectory and the Chebyshev trajectory I for $N = 25$ . Their first sidelobe amplitudes match one another and are equal to the given threshold $\gamma = 10^{-2.9} \approx 0.0013$ (except for the rectangular trajectory). The dashed gray box area is where we compare the different trajectories. See a zoom-in plot in Figure 5-2. . . . .	74
5-2	A zoom-in plot of the dashed gray box area in Figure 5-1. We find that $\omega_{\text{ch1}}^* < \omega_{\text{sl1}}^* < \omega_{\text{ka}}^* < \omega_{\text{bkm}}^*$ . . . . .	75
5-3	(a) The frequency-domain representations of the second Slepian trajectory and the Chebyshev trajectory II for $N = 25$ , where their first sidelobe amplitudes match each other and are equal to the given threshold $\gamma = 10^{-2.35} \approx 0.0045$ . (b) A zoom-in plot of the dashed gray box area in (a). We find that $\omega_{\text{ch2}}^* < \omega_{\text{sl2}}^*$ . . . . .	77
5-4	The frequency-domain representations of the second Slepian trajectory and the Chebyshev trajectory II for $N = 25$ , where their sidelobe amplitudes match each other at the 7th sidelobe. The threshold is set to be $\gamma = 10^{-2.86} \approx 0.0014$ . We find that $\omega_{\text{ch2}}^* < \omega_{\text{sl2}}^*$ . . . . .	78
6-1	Circuit diagram of a flux-tunable transmon capacitively coupled to a fixed-frequency transmon. The flux-tunable transmon is referred to as QB1 and the fixed-frequency transmon is referred to as QB2. Same figure as Figure 3-6. . . . .	80

6-2	Energy spectrum diagram of two coupled transmons as depicted in Figure 6-1 as the frequency of QB1 is detuned by changing the local magnetic flux that threads its SQUID loop. The avoided crossing between the states $ 11\rangle$ and $ 20\rangle$ is used to implement the CPHASE gate. The upper plot shows an example of a Slepian-based pulse to vary $\omega_1$ from $\omega_1 = 5.2$ GHz to $\omega_1 = 5.0$ GHz and then back to $\omega_1 = 5.2$ GHz.	82
6-3	(a) An example of $g_i[n]$ and (b) the corresponding $\varepsilon_i[n]$ based on a second Slepian trajectory. In simulation, $\varepsilon_i[n]$ and its linearly scaled versions indicate how the frequency detuning of QB1 varies through time, as shown in Figure 6-2.	83
6-4	(a) Time-domain and (b) frequency-domain representations of the specified second Slepian trajectory $g_{sl2}[n]$ . The red horizontal line $y = -2.5$ in (b) indicates the first sidelobe amplitude of the specified second Slepian trajectory.	85
6-5	Simulation results of (a) phase accumulation $\phi$ and (b) leakage error $P_e$ as a function of control pulse duration $t_d$ and amplitude $A$ using the specified second Slepian trajectory $g_{sl2}[n]$ . The red curve in (a) indicates the data points where the phase accumulation reaches $\pi$ for the first time. The red curve in (b) indicates the corresponding leakage error data points.	85
6-6	Leakage error $P_e$ as a function of pulse duration $t_d$ with phase accumulation of $\phi = \pi$ .	86
6-7	Comparison example 1. (a) Time-domain and (b) frequency-domain representations of the chosen Chebyshev trajectory II $g_{ch2}[n]$ compared with the specified second Slepian trajectory $g_{sl2}[n]$ . $g_{ch2}[n]$ is chosen for its sidelobe amplitude to match the first sidelobe amplitude of $g_{sl2}[n]$ . The red horizontal line in (b) indicates a given threshold $\gamma = 10^{-2.5} \approx 0.32\%$ .	86

6-8	Comparison example 1. Simulation results of (a) phase accumulation $\phi$ and (b) leakage error $P_e$ as a function of control pulse duration $t_d$ and amplitude $A$ using the chosen Chebyshev trajectory II $g_{\text{ch2}}[n]$ . . .	87
6-9	Comparison example 1. Leakage error $P_e$ as a function of pulse duration $t_d$ with phase accumulation of $\phi = \pi$ . For leakage error threshold $P_e = 10^{-4.1} \approx 0.008\%$ , we find that $t_{d-\text{ch2}} = 33.6 \text{ ns} < t_{d-\text{sl2}} = 37.6 \text{ ns}$ .	88
6-10	Comparison example 2. (a) Time-domain and (b) frequency-domain representations of the chosen Chebyshev trajectory II $g_{\text{ch2}}[n]$ compared with the specified second Slepian trajectory $g_{\text{sl2}}[n]$ . $g_{\text{ch2}}[n]$ is chosen for its sidelobe amplitude to match the 16th sidelobe amplitude of $g_{\text{sl2}}[n]$ . The red horizontal line in (b) indicates a given threshold $\gamma = 10^{-3.4} \approx 0.04\%$ . . . . .	88
6-11	Comparison example 2. Simulation results of (a) phase accumulation $\phi$ and (b) leakage error $P_e$ as a function of control pulse duration $t_d$ and amplitude $A$ using the chosen Chebyshev trajectory II $g_{\text{ch2}}[n]$ . . .	89
6-12	Comparison example 2. Leakage error $P_e$ as a function of pulse duration $t_d$ with phase accumulation of $\phi = \pi$ . For leakage error threshold $P_e = 10^{-5.8} \approx 0.00016\%$ , we find that $t_{d-\text{ch2}} = 50.6 \text{ ns} < t_{d-\text{sl2}} = 68.5 \text{ ns}$ .	90
6-13	Comparisons of $t_{d-\text{sl2}}$ and $t_{d-\text{ch2}}$ for different leakage error thresholds $P_e$ specified. . . . .	90
A-1	Example 1. (a) Time-domain and (b) frequency-domain representations of the chosen Chebyshev trajectory II $g_{\text{ch2}}[n]$ compared with the specified second Slepian trajectory $g_{\text{sl2}}[n]$ . $g_{\text{ch2}}[n]$ is chosen for its sidelobe amplitude to match the 3rd sidelobe amplitude of $g_{\text{sl2}}[n]$ . The red horizontal line in (b) indicates a given threshold $\gamma = 10^{-2.8} \approx 0.16\%$ . (c) Leakage error $P_e$ as a function of pulse duration $t_d$ with phase accumulation of $\phi = \pi$ . For leakage error threshold $P_e = 10^{-4.3} \approx 0.005\%$ , we find that $t_{d-\text{ch2}} = 31.0 \text{ ns} < t_{d-\text{sl2}} = 38.0 \text{ ns}$ . . . . .	96

A-2 Example 2. (a) Time-domain and (b) frequency-domain representations of the chosen Chebyshev trajectory II  $g_{\text{ch2}}[n]$  compared with the specified second Slepian trajectory  $g_{\text{sl2}}[n]$ .  $g_{\text{ch2}}[n]$  is chosen for its sidelobe amplitude to match the 6th sidelobe amplitude of  $g_{\text{sl2}}[n]$ . The red horizontal line in (b) indicates a given threshold  $\gamma = 10^{-2.97} \approx 0.11\%$ . (c) Leakage error  $P_e$  as a function of pulse duration  $t_d$  with phase accumulation of  $\phi = \pi$ . For leakage error threshold  $P_e = 10^{-4.9} \approx 0.0013\%$ , we find that  $t_{d-\text{ch2}} = 45.5 \text{ ns} = t_{d-\text{sl2}} = 45.5 \text{ ns}$ . . . . . 97

A-3 Example 3. (a) Time-domain and (b) frequency-domain representations of the chosen Chebyshev trajectory II  $g_{\text{ch2}}[n]$  compared with the specified second Slepian trajectory  $g_{\text{sl2}}[n]$ .  $g_{\text{ch2}}[n]$  is chosen for its sidelobe amplitude to match the 7th sidelobe amplitude of  $g_{\text{sl2}}[n]$ . The red horizontal line in (b) indicates a given threshold  $\gamma = 10^{-3.05} \approx 0.089\%$ . (c) Leakage error  $P_e$  as a function of pulse duration  $t_d$  with phase accumulation of  $\phi = \pi$ . For leakage error threshold  $P_e = 10^{-5.25} \approx 0.00056\%$ , we find that  $t_{d-\text{ch2}} = 49.7 \text{ ns} < t_{d-\text{sl2}} = 55.2 \text{ ns}$ . . . . . 98

A-4 Example 4. (a) Time-domain and (b) frequency-domain representations of the chosen Chebyshev trajectory II  $g_{\text{ch2}}[n]$  compared with the specified second Slepian trajectory  $g_{\text{sl2}}[n]$ .  $g_{\text{ch2}}[n]$  is chosen for its sidelobe amplitude to match the 12th sidelobe amplitude of  $g_{\text{sl2}}[n]$ . The red horizontal line in (b) indicates a given threshold  $\gamma = 10^{-3.26} \approx 0.055\%$ . (c) Leakage error  $P_e$  as a function of pulse duration  $t_d$  with phase accumulation of  $\phi = \pi$ . For leakage error threshold  $P_e = 10^{-5.6} \approx 0.00025\%$ , we find that  $t_{d-\text{ch2}} = 50.5 \text{ ns} < t_{d-\text{sl2}} = 60.0 \text{ ns}$ . . . . . 99

# List of Tables

2.1	Values of $C$ and forms of $A(\omega)$ for the four cases of pulses. Here, $a[n], b[n], c[n], d[n]$ are coefficients that can be determined given $h[n]$ .	30
2.2	Forms of $Q(\omega)$ and $P(\omega)$ for the four cases of pulses. Here, $\bar{a}[n], \bar{b}[n], \bar{c}[n], \bar{d}[n]$ are coefficients that can be determined given $h[n]$ . For Case 1, we have $\bar{a}[n] = a[n]$ .	31

# Chapter 1

## Introduction

### 1.1 Introduction to quantum computing

The idea of quantum computing was first proposed by Richard Feynman [1], who postulated that a quantum computer is necessary to efficiently simulate large quantum systems. Quantum computing harnesses the power of quantum mechanics to perform computation and is fundamentally different than classical computing. Quantum computing holds the promise of solving certain problems that are believed to be classically hard. In particular, when a problem is referred to as being classically hard, it generally means that the problem requires an amount of computational sources that grows exponentially with the size of the problem. Examples of such problems are the travelling salesman problem [2] and the integer factorization problem. Over the past few decades, there has been tremendous progress on both experimental and theoretical work in the pursuit of the ultimate goal of realizing fault-tolerant quantum computing. Experimentally, we have witnessed demonstrations in quantum systems comprising tens to hundreds of noisy qubits [3, 4, 5]. On the theory side, many quantum algorithms have been proposed with the purpose of exploiting the computational power of quantum computing for real-world applications [6]. For example, Shor's algorithm [7] offers the potential to factor large composite integers into their constituent primes in reasonable time, and Grover's algorithm [8] provides a quantum solution to unstructured database search problems.

While researchers have made great achievements building upon the amazing foundational idea of Richard Feynman, there still exist challenges towards realizing large-scale fault-tolerant quantum computing. One of the challenges is how to improve the operational fidelity of a quantum gate, and how to systematically tackle this problem. These important questions guide this thesis, which aims to improve the pulse design for baseband controlled phase gates in superconducting circuits.

## 1.2 Introduction to pulse design

Pulse design is the process of designing pulses for various applications in science and engineering, which requires a combination of physical principles, mathematical analysis, and computational techniques. Pulses can be designed with specific properties, such as frequency, amplitude, duration, and shape, to achieve different goals in different applications. These applications include spectrum analysis, filter design, radar and sonar systems, magnetic resonance imaging (MRI), quantum computing and engineering. Examples of approaches widely used in pulse design problems include Fourier analysis, and mathematical and numerical optimization methods. In this thesis, we explore the pulse design problem in the context of quantum computing and engineering. To be more specific, we investigate the pulse design problem of a particular flux-based two-qubit gate in superconducting circuits.

## 1.3 Thesis overview

We first introduce several common finite-length discrete-time pulses in Chapter 2, and then review, in Chapter 3, the physical background on how baseband flux-based two-qubit gates, in particular the CPHASE gate, are implemented in superconducting qubits. In Chapter 4 we formulate the problem using a two-level system abstraction and state explicitly the optimality criterion to be investigated. Then, in Chapter 5 we present multiple candidates for the control trajectory of the pulse design problem based on common finite-length discrete-time pulses, and propose the Chebyshev pulse

I and II as alternative solutions compared to the Slepian counterparts. In Chapter 6 we discuss time-domain simulation results using QuTiP [9, 10] and demonstrate the advantage of the Chebyshev pulse II when implementing a CZ gate. Finally, in Chapter 7 we conclude the thesis and discuss thoughts on potential future work.

# Chapter 2

## Finite-length Discrete-time Pulses

In order to establish some background information in the pulse design problem, we introduce the definition and notation of finite-length discrete-time pulses in Section 2.1. We review some common and useful finite-length discrete-time pulses that have been extensively studied in literature in Section 2.2 and Section 2.3. We show the time-domain and frequency-domain representations of the pulses.

### 2.1 Definition and notation

In this thesis, we focus on the design of finite-length discrete-time pulses, which we will refer to as pulses for brevity if no confusion is caused. Finite-length discrete-time pulses take on certain values over some chosen finite-length discrete-time interval and are zero-valued outside the interval. Mathematically, we define a finite-length discrete-time pulse  $w[n]$  as

$$w[n] = \begin{cases} \hat{w}[n], & 0 \leq n \leq N - 1 \\ 0, & \text{otherwise} \end{cases} \quad (2.1)$$

where  $\hat{w}[n]$  denotes the values over the finite-length discrete-time interval  $[0, N - 1]$ , and  $N$  is a finite positive integer referred to as the length of the pulse  $w[n]$ . The

discrete-time Fourier transform of the pulse  $w[n]$  is given by

$$W(e^{i\omega}) = \sum_{n=0}^{N-1} w[n]e^{-i\omega n} \quad (2.2)$$

## 2.2 Examples of common finite-length discrete-time pulses

### 2.2.1 Rectangular pulse

The rectangular pulse of length  $N$  is defined as

$$w_{\text{rec}}[n] = \begin{cases} 1, & 0 \leq n \leq N - 1 \\ 0, & \text{otherwise} \end{cases} \quad (2.3)$$

The Fourier transform of the rectangular pulse can then be written as

$$W_{\text{rec}}(e^{i\omega}) = \sum_{n=0}^{N-1} e^{-i\omega n} = e^{-i\frac{N-1}{2}\omega} \frac{\sin \frac{N\omega}{2}}{\sin \frac{\omega}{2}} \quad (2.4)$$

The time-domain and frequency-domain representations of the rectangular pulse for  $N = 25$  are shown in Figure 2-1. The magnitude of the Fourier transform is normalized to be 0 dB at  $\omega = 0$ . As we can observe from the frequency-domain representations of the rectangular pulse and other pulses to be introduced in the following sections, the amplitude of the sidelobes of the rectangular pulse is relatively large while the width of the mainlobe is typically small. In this thesis, the mainlobe is defined as the region between the first zero-crossing and the origin, and the sidelobes are defined as the regions between adjacent zero-crossings beyond the first zero-crossing.

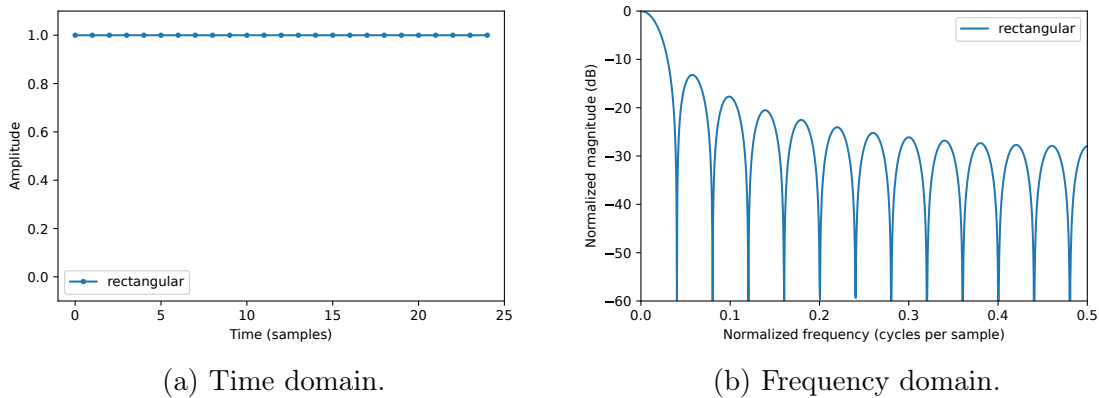


Figure 2-1: Time-domain and frequency-domain representations of the rectangular pulse for  $N = 25$ .

## 2.2.2 Raised cosine pulse

The raised cosine pulses are of particular interest when a smooth change in the interval is desired. There are many variations of a raised cosine pulse. Here we review the Hann pulse, the Hamming pulse, and the Blackman pulse [11].

The Hann pulse is simply one period of a single cosine function defined as

$$w_{\text{hann}}[n] = \begin{cases} 0.5 - 0.5 \cos \frac{2\pi n}{N-1}, & 0 \leq n \leq N-1 \\ 0, & \text{otherwise} \end{cases} \quad (2.5)$$

The Hamming pulse is a slight variation to the Hann pulse in which coefficients are adjusted. It is defined as

$$w_{\text{hamm}}[n] = \begin{cases} 0.54 - 0.46 \cos \frac{2\pi n}{N-1}, & 0 \leq n \leq N-1 \\ 0, & \text{otherwise} \end{cases} \quad (2.6)$$

The Blackman pulse uses a sum of two cosine terms defined as

$$w_{\text{bkm}}[n] = \begin{cases} 0.42 - 0.5 \cos \frac{2\pi n}{N-1} + 0.08 \cos \frac{4\pi n}{N-1}, & 0 \leq n \leq N-1 \\ 0, & \text{otherwise} \end{cases} \quad (2.7)$$

These examples of raised cosine pulses can be written in the generalized form of a sum of multiple cosine terms

$$w_{\cos}[n] = \begin{cases} \alpha_0 + \sum_{k=1}^K \alpha_k \cos \frac{2\pi kn}{N-1}, & 0 \leq n \leq N-1 \\ 0, & \text{otherwise} \end{cases} \quad (2.8)$$

where  $K$  denotes the number of cosine terms included and  $\alpha_k$ ,  $0 \leq k \leq K$  are constant coefficients.

The time-domain and frequency-domain representations of the Hann pulse, the Hamming pulse, and the Blackman pulse for  $N = 25$  are shown in Figure 2-2. The magnitude of the Fourier transform is normalized to be 0 dB at  $\omega = 0$ .

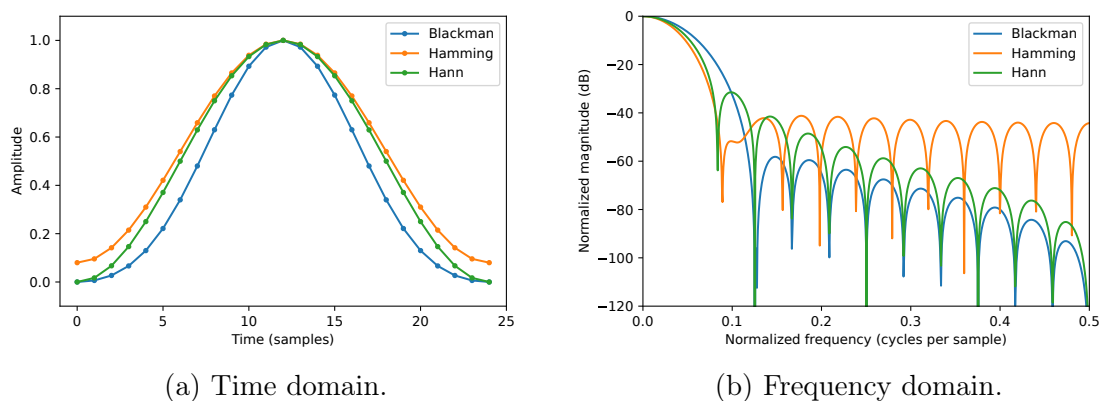


Figure 2-2: Time-domain and frequency-domain representations of the Hann pulse, the Hamming pulse and the Blackman pulse for  $N = 25$ .

As we can observe from the comparisons in Figures 2-1 and 2-2, when the pulses taper more quickly in the time domain, the mainlobe width in the frequency domain becomes larger with the sidelobe amplitudes smaller. In the family of raised cosine pulses, including more cosine terms, i.e., increasing  $K$  in Eq. 2.8, could potentially lead to smaller sidelobe amplitudes but larger mainlobe width with proper choices of coefficients  $\alpha_k$ .

### 2.2.3 Slepian pulse

The Slepian pulses, also known as discrete prolate spheroidal sequences (DPSSs), are a set of orthogonal pulses intended for the problem of maximal concentration in both the time domain and the frequency domain. The relevant discussions date back to the Fourier analysis and its uncertainty [12]. In a sense similar to Heisenberg's uncertainty principle [13] in quantum mechanics, pulses cannot be confined in both the time domain and the frequency domain (except for the trivial all-zero pulse). Then a fundamental problem arose: how to optimally concentrate the energy in one domain if the pulse is strictly confined in the other domain. This problem, both in continuous time and in discrete time, was pursued and solved by Slepian, Landau, and Pollack in a series of papers [12, 14, 15, 16, 17, 18]. Here we briefly review the development and analysis of the Slepian pulses. In particular, we focus on the analysis of the discrete-time case.

Consider a finite-length discrete-time pulse  $x[n]$ ,  $n = 0, 1, \dots, N - 1$ , which is specified to have finite energy, i.e.,

$$E = \sum_{n=0}^{N-1} |x[n]|^2 < \infty \quad (2.9)$$

where  $E$  denotes the energy of the pulse  $x[n]$ .

The discrete-time Fourier transform of the pulse  $x[n]$  is given by

$$X(e^{i\omega}) = \sum_{n=0}^{N-1} x[n]e^{-i\omega n} \quad (2.10)$$

Let  $0 < W < \pi$ . The goal is to find the maximum value of the ratio  $\lambda$  defined as

$$\lambda = \frac{\int_{-W}^W |X(e^{i\omega})|^2 d\omega}{\int_{-\pi}^{\pi} |X(e^{i\omega})|^2 d\omega} \quad (2.11)$$

for all pulses  $x[n]$ ,  $n = 0, 1, \dots, N - 1$  of length  $N$ , and ask for the pulse  $x_{\text{opt}}[n]$  that

obtain the maximum value  $\lambda_{\text{opt}}$ . The ratio  $\lambda \in [0, 1]$  measures the percentage of the energy contained in the frequency band  $[-W, W]$  over the total energy.

The Slepian pulses  $\{v_n^{(k)}(N, W), k = 0, 1, \dots, N - 1\}$  are the solutions to the optimization problem stated above [17], where  $n = 0, 1, \dots, N - 1$  is the index of the pulse,  $k$  is the order of each pulse, and  $N$  and  $W$  are parameters referred to as the length and mainlobe width (as defined in this thesis) of the pulse, respectively. The Slepian pulses can be derived from the real solutions to the system of equations

$$\sum_{m=0}^{N-1} \frac{\sin 2\pi W(n-m)}{\pi(n-m)} v_m^{(k)}(N, W) = \lambda_k(N, W) v_n^{(k)}(N, W), \quad n = 0, 1, \dots, N - 1 \quad (2.12)$$

for each  $k = 0, 1, \dots, N - 1$ . Note that when  $n = m$ , we have

$$\frac{\sin 2\pi W(n-m)}{\pi(n-m)} = 2W \quad (2.13)$$

Eqs. 2.12 can also be written in the matrix form

$$\mathbf{A} \mathbf{v}^{(k)} = \lambda_k \mathbf{v}^{(k)} \quad (2.14)$$

where

$$\mathbf{A}_{n,m} = \frac{\sin 2\pi W(n-m)}{\pi(n-m)}, \quad n, m = 0, 1, \dots, N - 1 \quad (2.15a)$$

$$\mathbf{v}^{(k)} = [v_0^{(k)}(N, W), v_1^{(k)}(N, W), \dots, v_{N-1}^{(k)}(N, W)]^T \quad (2.15b)$$

with  $T$  denoting the matrix transpose.

Eq. 2.14 is essentially an eigenvalue problem, where  $\lambda_k$ 's are the  $N$  distinct eigenvalues and  $\mathbf{v}^{(k)}$ 's are the corresponding eigenvectors. By convention the eigenvalues are ranked as  $1 > \lambda_0 > \lambda_1 > \dots > \lambda_{N-1} > 0$ . Therefore, the sequence  $v_n^{(0)}(N, W)$  that corresponds to the largest eigenvalue  $\lambda_0$  is referred to as the first Slepian pulse that maximizes the ratio  $\lambda$  in Eq. 2.11. The second Slepian pulse  $v_n^{(1)}(N, W)$  maximizes the ratio  $\lambda$  and is orthogonal to the first Slepian pulse  $v_n^{(0)}(N, W)$ . The third Slepian pulse  $v_n^{(2)}(N, W)$  maximizes the ratio  $\lambda$  and is orthogonal to the first and second Slepian pulse,  $v_n^{(0)}(N, W)$  and  $v_n^{(1)}(N, W)$ . And so forth.

The first and second Slepian pulses are considered in this thesis, as we will elaborate further in Section 5.2 for the Type-I and Type-II processes, respectively. The time-domain and frequency-domain representations of the first and second Slepian pulses for  $N = 25$  and  $NW = 3$  are shown in Figure 2-3. The magnitude of the Fourier transform is normalized to be 0 dB at  $\omega = 0$  for the first Slepian pulse, while for the second Slepian pulse, it is normalized so that the peak magnitude of the mainlobe is 0 dB. Compared to the rectangular pulse and raised cosine pulses, we find that the Slepian pulses have a relatively low sidelobe amplitude with a relatively small mainlobe width, which makes them a good candidate when a compromise between the two characteristics is desired.

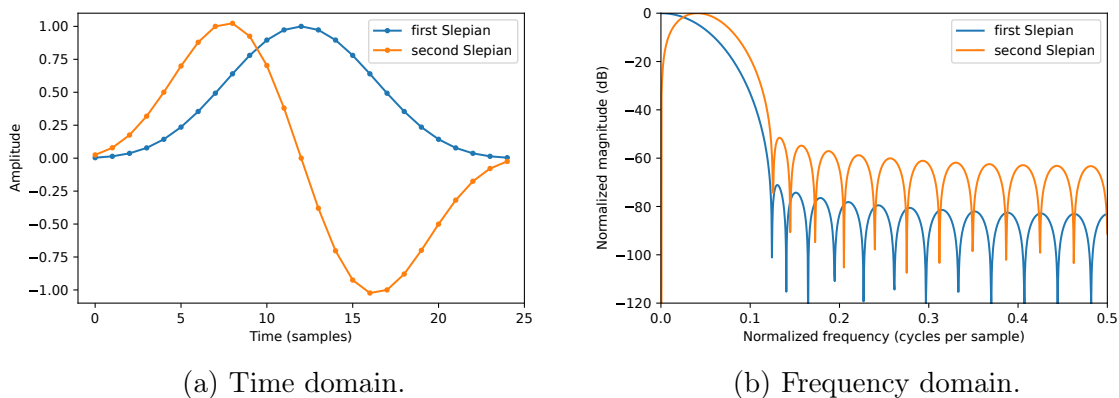


Figure 2-3: Time-domain and frequency-domain representations of the first and second Slepian pulses for  $N = 25$  and  $NW = 3$ .

In this thesis, to keep the notation consistent, we denote the first Slepian pulse as

$$w_{\text{sl1}}[n] = \begin{cases} v_n^{(0)}(N, W), & 0 \leq n \leq N - 1 \\ 0, & \text{otherwise} \end{cases} \quad (2.16)$$

and the second Slepian pulse as

$$w_{\text{sl2}}[n] = \begin{cases} v_n^{(1)}(N, W), & 0 \leq n \leq N - 1 \\ 0, & \text{otherwise} \end{cases} \quad (2.17)$$

## 2.2.4 Kaiser pulse

The Kaiser pulse [19, 20] is a good approximation to the first Slepian pulse, but simpler to compute. The Kaiser pulse is defined as

$$w_{\text{ka}}[n] = \begin{cases} \frac{I_0[\beta(1 - [(n - \alpha)/\alpha]^2)^{1/2}]}{I_0(\beta)}, & 0 \leq n \leq N - 1 \\ 0, & \text{otherwise} \end{cases} \quad (2.18)$$

where  $\alpha = (N - 1)/2$  and  $I_0(\cdot)$  represents the zeroth-order modified Bessel function of the first kind, and  $\beta$  is a real-valued parameter that determines the shape of the Kaiser pulse. When  $\beta = 0$ , the Kaiser pulse reduces to the rectangular pulse.

The time-domain and frequency-domain representations of the Kaiser pulse for  $N = 25$  and  $\beta = 8$ , and the first Slepian pulses for  $N = 25$  and  $NW = 3$  are shown in Figure 2-4. The magnitude of the Fourier transform is normalized to be 0 dB at  $\omega = 0$ . Since the Kaiser pulse is developed to approximate the first Slepian pulse, it is expected that they share similar frequency-domain characteristics for an appropriate set of parameters, i.e.,  $W$  for the first Slepian pulse and  $\beta$  for the Kaiser pulse.

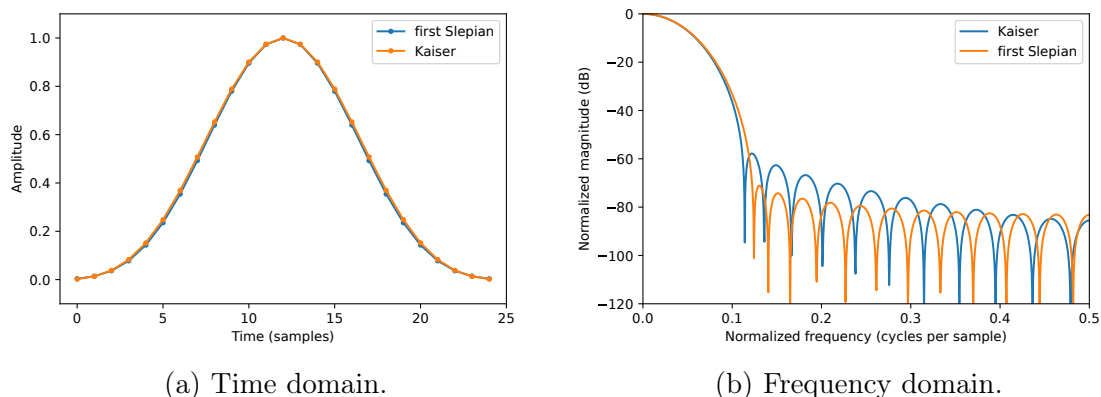


Figure 2-4: Time-domain and frequency-domain representations of the Kaiser pulse for  $N = 25$  and  $\beta = 8$ , and the first Slepian pulse for  $N = 25$  and  $NW = 3$ . The two pulses share very similar characteristics for appropriately chosen parameters since the Kaiser pulse is developed to approximate the first Slepian pulse.

## 2.2.5 Chebyshev pulse I

Dolph formulated and solved the problem of finding a pulse that minimizes the main-lobe width given a specified sidelobe amplitude, or equivalently, minimizes the sidelobe amplitude given a specified mainlobe width in the context of antenna array design [21]. The optimal solution to this problem is known as the Chebyshev pulse.

The Chebyshev pulse is based on the Chebyshev polynomials defined as

$$T_n(x) = \begin{cases} \cos(n \arccos(x)) & |x| \leq 1 \\ \cosh(n \operatorname{arccosh}(x)) & x \geq 1 \\ (-1)^n \cosh(n \operatorname{arccosh}(-x)) & x \leq -1 \end{cases} \quad (2.19)$$

where  $n$  denotes the order of the Chebyshev polynomials. Plugging in the values  $n = 0$  and  $n = 1$ , we have  $T_0(x) = 1$  and  $T_1(x) = x$ . Using the double angle trigonometric identity, i.e.,  $\cos 2\theta = 2\cos^2\theta - 1$  or  $\cosh 2\theta = 2\cosh^2\theta - 1$ , the following recurrence relation can be verified

$$T_n(x) = 2xT_{n-1}(x) - T_{n-2}(x), \quad n \geq 2 \quad (2.20)$$

It can be further shown that  $T_n(x)$  is an  $n$ th-order polynomial in  $x$ , i.e.,  $T_n(x)$  can be equivalently written as the ordinary polynomial

$$T_n(x) = \sum_{k=0}^n b[k]x^k \quad (2.21)$$

for some coefficients  $b[k]$ ,  $k = 0, 1, \dots, n$ .  $T_n(x)$  is even or odd according to whether  $n$  is even or odd.  $T_n(x)$  oscillates between  $-1$  and  $1$  when  $-1 \leq x \leq 1$  and is monotonic when  $x \geq 1$  or  $x \leq -1$ . The first few Chebyshev polynomials of orders  $n = 0, 1, 2, 3, 4$  are shown in Figure 2-5.

The Chebyshev pulse  $w_{\text{ch1}}[n]$  can be defined through its Fourier transform

$$W_{\text{ch1}}(e^{i\omega}) = e^{-i\omega \frac{N-1}{2}} \frac{T_{N-1}(x_0 \cos(\omega/2))}{T_{N-1}(x_0)} \quad (2.22)$$

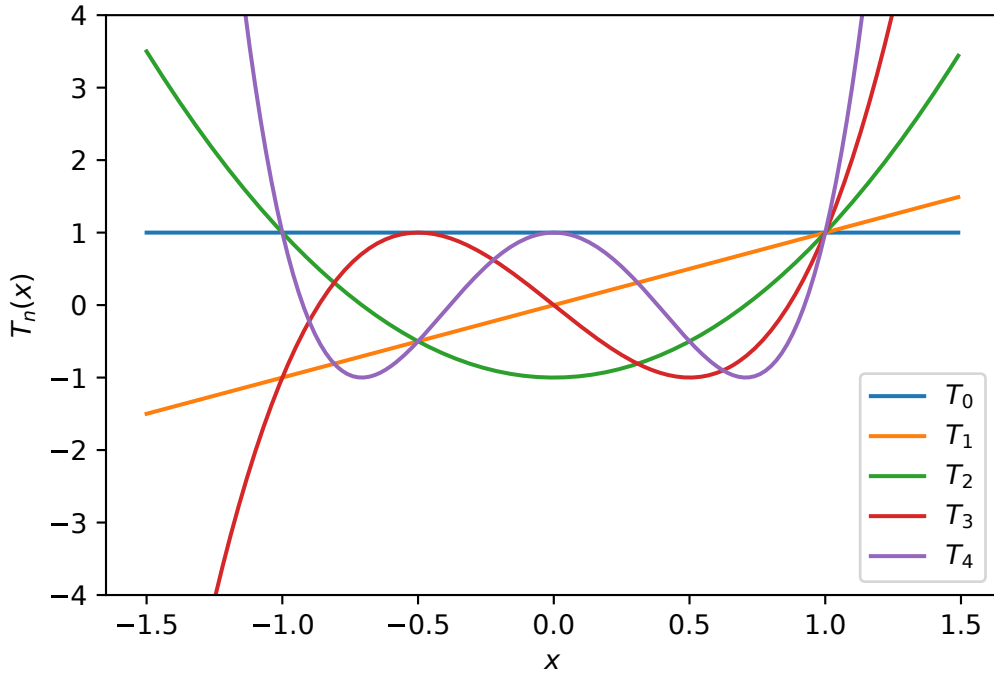


Figure 2-5: Plots of the Chebyshev polynomials of orders  $n = 0, 1, 2, 3, 4$ .

where  $N$  denotes the length of the pulse, and  $x_0 > 1$  is a parameter related to the sidelobe amplitude of  $W_{\text{ch1}}(e^{i\omega})$ . Let  $\omega_s$  be such that  $x_0 \cos(\omega_s/2) = 1$ . As  $\omega$  increases from 0 to  $\omega_s$ , the argument of the numerator in Eq. 2.22, i.e.,  $x_0 \cos(\omega/2)$ , decreases from  $x_0$  to 1, and thus  $W_{\text{ch1}}(e^{i\omega})$  decreases from 1 to  $\frac{1}{T_{N-1}(x_0)} := r$ . As  $\omega$  increases from  $\omega_s$  to  $\pi$ ,  $W_{\text{ch1}}(e^{i\omega})$  will oscillate between  $-r$  and  $r$ .

Utilizing basic trigonometric identities and considering that  $T_n(x)$  is an  $n$ th-order polynomial in  $x$ , it can be shown that Eq. 2.22 can further be written in a more structured form

$$W_{\text{ch1}}(e^{i\omega}) = \sum_{n=0}^{N-1} w_{\text{ch1}}[n] e^{-i\omega n} \quad (2.23)$$

where  $w_{\text{ch1}}[n]$ ,  $n = 0, 1, \dots, N - 1$  are the coefficients of the Chebyshev pulse. The Chebyshev pulse coefficients can also be evaluated from the inverse Fourier transform

of Eq. 2.22. The explicit analytical formula is given by

$$w_{\text{ch1}}[n] = \frac{1}{N} \left[ 1 + 2r \sum_{k=0}^{N_s} (-1)^k T_{N-1} \left( x_0 \cos \frac{\pi k}{N} \right) \cos \left( \frac{2\pi k}{L} \left( n + \frac{1}{2} \right) \right) \right], \quad n = 0, 1, \dots, N-1 \quad (2.24)$$

where  $r = \frac{1}{T_{N-1}(x_0)}$  is as defined earlier, and

$$N_s = \begin{cases} \frac{N-1}{2} & N \text{ odd} \\ \frac{N}{2} - 1 & N \text{ even} \end{cases} \quad (2.25)$$

The time-domain and frequency-domain representations of the Chebyshev pulses for  $N = 25$  and different specified sidelobe amplitudes ( $-60$  dB and  $-80$  dB) are shown in Figure 2-6. The magnitude of the Fourier transform is normalized to be 0 dB at  $\omega = 0$ . One important characteristic of the Chebyshev pulse is the equiripple sidelobe amplitude for all sidelobes. From Figure 2-6, we can observe that as the sidelobe amplitude of the Chebyshev pulse is specified to be lower, its mainlobe width will be larger. In Section 2.3.1 we will show that the Chebyshev pulse is a special case of the result of the weighted Chebyshev approximation. In later chapters, when it is necessary to discriminate between the Chebyshev pulse discussed in this section and the Chebyshev pulse II to be introduced in Section 2.3.2, we will refer to the Chebyshev pulse as the Chebyshev pulse I to avoid confusion.

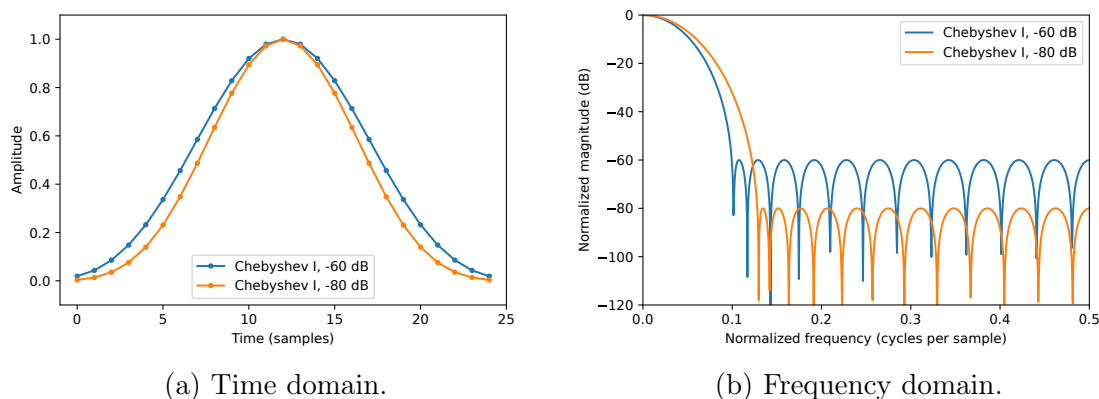


Figure 2-6: Time-domain and frequency-domain representations of the Chebyshev pulses for  $N = 25$  and sidelobe amplitudes specified to be  $-60$  dB and  $-80$  dB.

## 2.3 Pulses based on weighted Chebyshev approximation

In Section 2.2 we have discussed a few examples of some common finite-length discrete-time pulses. However, this is not the whole story. In fact, all the pulses we have mentioned so far (except the second Slepian pulse) are symmetric. In Section 2.3.1, we will review the weighted Chebyshev approximation, which can be used to design both symmetric and anti-symmetric pulses. Then in Section 2.3.2, we will show examples of pulses designed through the weighted Chebyshev approximation.

### 2.3.1 Weighted Chebyshev approximation

In Section 2.3.1, we review the basics of the weighted Chebyshev approximation (WCA) in the context of finite-length discrete-time pulse design.

Let  $h[n]$ ,  $n = 0, 1, \dots, N - 1$ , be a real-valued finite-length discrete-time pulse of length  $N$  defined over the discrete-time interval  $0 \leq n \leq N - 1$ . The Fourier transform of  $h[n]$  is

$$H(e^{i\omega}) = \sum_{n=0}^{N-1} h[n]e^{-i\omega n} \quad (2.26)$$

$H(e^{i\omega})$  can also be written in terms of its amplitude and phase, i.e.,

$$H(e^{i\omega}) = A(\omega)e^{i\phi(\omega)} \quad (2.27)$$

where  $A(\omega)$  and  $\phi(\omega)$  are both real-valued functions of  $\omega$ .

We then further require that  $h[n]$  be symmetric or anti-symmetric. Here, when  $h[n]$  is referred to as being symmetric, it means

$$h[n] = h[N - 1 - n], \quad n = 0, 1, \dots, N - 1 \quad (2.28)$$

Similarly, when  $h[n]$  is referred to as being anti-symmetric, it means

$$h[n] = -h[N - 1 - n], \quad n = 0, 1, \dots, N - 1 \quad (2.29)$$

Depending on the value of  $N$  being odd or even and  $h[n]$  being symmetric or anti-symmetric, there exist four cases of pulses  $h[n]$ . With the symmetry constraints, it can be shown that  $\phi(\omega)$  can be written in the form of  $\phi(\omega) = C + B\omega$ , which is a linear function of  $\omega$ , where  $C$  and  $B = -\frac{N-1}{2}$  are real-valued. Therefore, the Fourier transform of the four cases of pulses can be written in the form

$$H(e^{i\omega}) = A(\omega)e^{iC}e^{iB\omega} \quad (2.30)$$

Values of  $C$  and forms of  $A(\omega)$  are given in Table 2.1.

	$C$	$A(\omega)$
Case 1: $N$ odd, $h[n]$ symmetric	0	$\sum_{n=0}^{\frac{N-1}{2}} a[n] \cos(\omega n)$
Case 2: $N$ even, $h[n]$ symmetric	0	$\sum_{n=0}^{\frac{N}{2}} b[n] \cos(\omega(n - 1/2))$
Case 3: $N$ odd, $h[n]$ anti-symmetric	1	$\sum_{n=0}^{\frac{N-1}{2}} c[n] \sin(\omega n)$
Case 4: $N$ even, $h[n]$ anti-symmetric	1	$\sum_{n=0}^{\frac{N}{2}} d[n] \sin(\omega(n - 1/2))$

Table 2.1: Values of  $C$  and forms of  $A(\omega)$  for the four cases of pulses. Here,  $a[n], b[n], c[n], d[n]$  are coefficients that can be determined given  $h[n]$ .

Note that the forms of  $A(\omega)$  are either a sum of cosines or sines, with the argument being either  $\omega n$  or  $\omega(n - 1/2)$ . Utilizing basic trigonometric identities, the forms of  $A(\omega)$  for all four cases can be rewritten in the form  $A(\omega) = Q(\omega)P(\omega)$ , where  $Q(\omega)$  is specific to each case and  $P(\omega)$  is always a sum of cosines. Forms of  $Q(\omega)$  and  $P(\omega)$  are given in Table 2.2.

Having established the notations, the Chebyshev approximation problem may be stated as follows. Given a disjoint union of frequency bands of interest  $\mathcal{F} \subset [0, \pi]$ , a desired function  $D(\omega)$  defined and continuous on  $\mathcal{F}$ , a positive weighting function  $W(\omega)$  defined and continuous on  $\mathcal{F}$ , and a desired choice of one of the four cases of

	$Q(\omega)$	$P(\omega)$
Case 1: $N$ odd, $h[n]$ symmetric	1	$\sum_{n=0}^{\frac{N-1}{2}} \bar{a}[n] \cos(\omega n)$
Case 2: $N$ even, $h[n]$ symmetric	$\cos(\omega/2)$	$\sum_{n=0}^{\frac{N}{2}-1} \bar{b}[n] \cos(\omega n)$
Case 3: $N$ odd, $h[n]$ anti-symmetric	$\sin(\omega)$	$\sum_{n=0}^{\frac{N-3}{2}} \bar{c}[n] \cos(\omega n)$
Case 4: $N$ even, $h[n]$ anti-symmetric	$\sin(\omega/2)$	$\sum_{n=0}^{\frac{N}{2}-1} \bar{d}[n] \cos(\omega n)$

Table 2.2: Forms of  $Q(\omega)$  and  $P(\omega)$  for the four cases of pulses. Here,  $\bar{a}[n], \bar{b}[n], \bar{c}[n], \bar{d}[n]$  are coefficients that can be determined given  $h[n]$ . For Case 1, we have  $\bar{a}[n] = a[n]$ .

$h[n]$ , the minimum of the following quantity

$$\|E(\omega)\| := \max_{\omega \in \mathcal{F}} W(\omega) |D(\omega) - A(\omega)| \quad (2.31)$$

and the corresponding  $h[n]$  are desired. Here,  $E(\omega) := W(\omega) |D(\omega) - A(\omega)|$  is referred to as the weighted approximation error and the optimization problem is essentially a minimax problem.

Considering we have the form  $A(\omega) = Q(\omega)P(\omega)$ , we can rewrite the weighted approximation error as

$$E(\omega) = W(\omega) |D(\omega) - A(\omega)| \quad (2.32)$$

$$= W(\omega) |D(\omega) - Q(\omega)P(\omega)| \quad (2.33)$$

$$= W(\omega) Q(\omega) \left| \frac{D(\omega)}{Q(\omega)} - P(\omega) \right| \quad (2.34)$$

Note that Eq. 2.34 is valid except possibly at  $\omega = 0$  or  $\pi$ . To avoid those scenarios where  $Q(\omega) = 0$ , it suffices to restrict that  $\mathcal{F} \subset [0, \pi)$  for Case 2 problems,  $\mathcal{F} \subset (0, \pi)$  for Case 3 problems, and  $\mathcal{F} \subset (0, \pi]$  for Case 4 problems.

Let  $\hat{W}(\omega) = W(\omega)Q(\omega)$  and  $\hat{D}(\omega) = D(\omega)/Q(\omega)$ , and we have

$$E(\omega) = \hat{W}(\omega)|\hat{D}(\omega) - P(\omega)| \quad (2.35)$$

With the form of weighted approximation error in Eq. 2.35, the algorithmic solution to the above mentioned problem makes use of the alternation theorem and the Remez exchange algorithm, or the Parks-McClellan algorithm [22, 23, 24]. We refer the readers to the included references for more details.

The solution for designing pulses in the minimax sense as in Eq. 2.31 is often in a numerical form without explicit analytical form. However, with a special set of  $\mathcal{F} \subset [0, \pi]$ ,  $D(\omega)$  and  $W(\omega)$ , and with  $h[n]$  specified to be Case 1 or 2, the solution coincides with the Chebyshev pulse I as discussed in Section 2.2.5. In other words, the Chebyshev pulse I is a special case in the weighted Chebyshev approximation problem. We refer the readers to Chapter 3 of Ref. [25] for more details. Figure 2-7 shows the time-domain and frequency-domain representations of an example of using the weighted Chebyshev approximation (WCA) to design a pulse, which coincides with the Chebyshev pulse I with sidelobe amplitude specified to be  $-60$  dB in Figure 2-6. Note that there is only one ripple in the passband, which is otherwise referred to as the mainlobe.

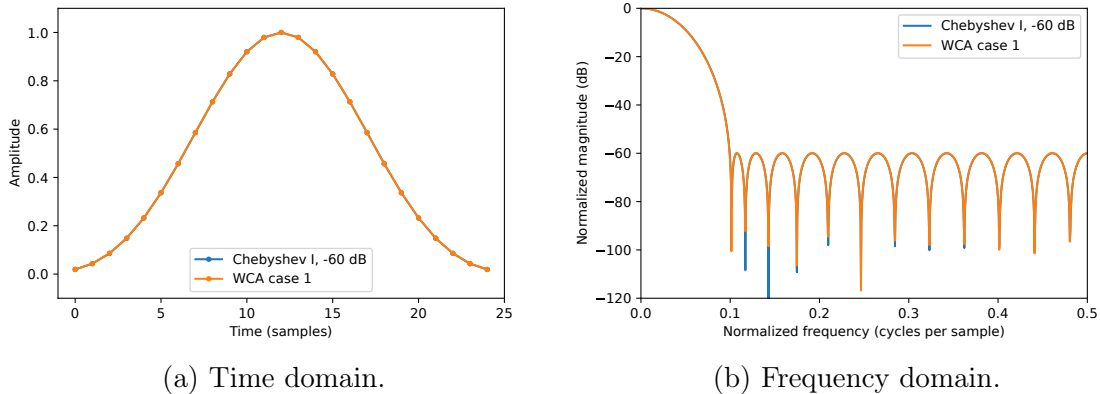


Figure 2-7: Time-domain and frequency-domain representations of a Case 1 pulse of length  $N = 25$  using weighted Chebyshev approximation (WCA) to coincide with the Chebyshev pulse I for  $N = 25$  with sidelobe amplitude specified to be  $-60$  dB.

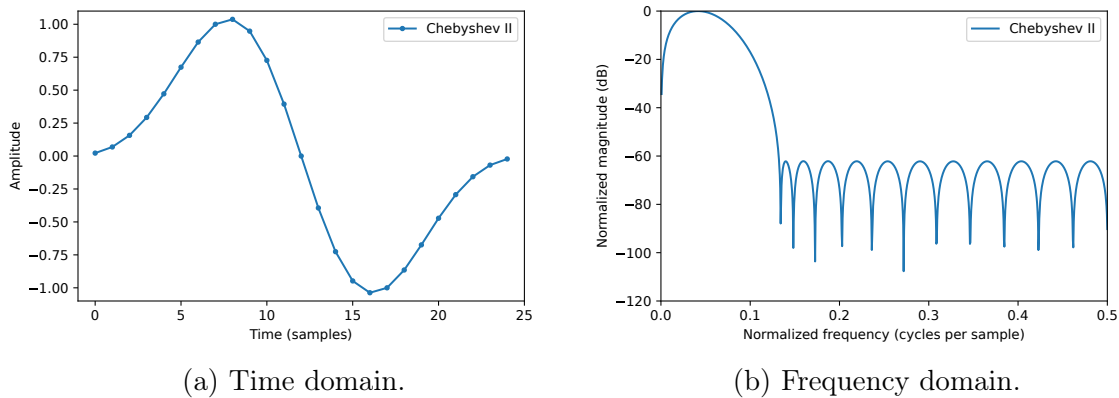


Figure 2-8: Time-domain and frequency-domain representations of a Case 3 pulse of length  $N = 25$  using weighted Chebyshev approximation, which is referred to in this thesis as the Chebyshev pulse II.

### 2.3.2 Chebyshev pulse II

We define the Chebyshev pulse II  $w_{\text{ch2}}[n]$  using the weighted Chebyshev approximation. If we provide an appropriate set of  $\mathcal{F} \subset [0, \pi]$ ,  $D(\omega)$  and  $W(\omega)$ , but specify  $h[n]$  to be Case 3 or 4, the optimal solution to the weighted Chebyshev approximation problem will be an anti-symmetric counterpart of the Chebyshev pulse I  $w_{\text{ch1}}$ , which we refer to as the Chebyshev pulse II  $w_{\text{ch2}}[n]$ . The Chebyshev pulse II shares the same characteristics of equiripple sidelobe amplitude and only one ripple in the passband as the Chebyshev pulse I. Note that it is not necessarily true that the solution given by the weighted Chebyshev approximation will always be an instance of the Chebyshev pulse II, for any set of  $\mathcal{F} \subset [0, \pi]$ ,  $D(\omega)$  and  $W(\omega)$ . In order to find an appropriate Chebyshev pulse II  $w_{\text{ch2}}[n]$ , the parameters need to be properly chosen. The time-domain and frequency-domain representations of an example of the Chebyshev pulse II are shown in Figure 2-8. The magnitude of the Fourier transform is normalized so that the peak magnitude of the mainlobe is 0 dB.

# Chapter 3

## Two-Qubit Gates in Superconducting Circuits

Having established some background of finite-length discrete-time pulses in Chapter 2, we continue to review the basics of quantum computing in Chapter 3. In Section 3.1 and Section 3.2, we first introduce the definition of qubits on a conceptual level and then discuss the physical realization of qubits using superconducting circuits. In Section 3.3, we briefly introduce single-qubit gates and two-qubit gates, which are sufficient to form a universal gate set. We discuss in detail one approach to implementing the CPHASE gate in tunable transmon qubits in Section 3.4. Finally, in Section 3.5 we review the efforts in the literature on the baseband control trajectory design of the CPHASE gate.

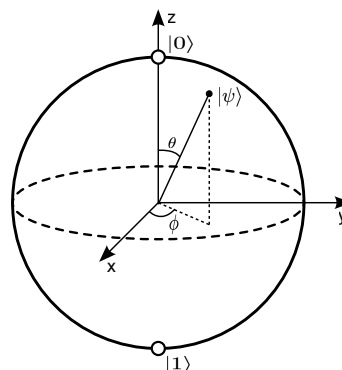
### 3.1 Qubits

Qubits, short for “quantum bits,” are a counterpart in the realm of quantum computing to bits, which are used to represent data encoding in classical computing. There exists a fundamental difference between bits and qubits as depicted in Figure 3-1. In the classical world, a bit can only take on definite values, either 0 or 1, at a time, as indicated by two ends of a stick in Figure 3-1a. However, in the quantum world, a qubit can take on not only  $|0\rangle$  or  $|1\rangle$ , but also an arbitrary superposition of both.

Here we utilize the bra-ket notation, or Dirac notation [26] to ubiquitously denote quantum states.



(a) A classical bit.



(b) A quantum bit (qubit).

Figure 3-1: A classical bit v.s. a quantum bit (qubit). (a) A classical bit can be in either the “0” state or the “1” state, represented by two ends of a stick. (b) A quantum bit can be in any superposition of the state  $|0\rangle$  and the state  $|1\rangle$ , graphically represented by the Bloch vector on a sphere known as the Bloch sphere.

The Bloch sphere plays an important role in representing the quantum state of a qubit. Figure 3-1b shows a Bloch vector on the Bloch sphere representing the quantum state  $|\psi\rangle = \alpha|0\rangle + \beta|1\rangle$ , where  $\alpha$  and  $\beta$  are probability amplitudes for the states  $|0\rangle$  and  $|1\rangle$ , and  $|\psi\rangle$  is referred to as the state vector. It is intuitive to view the Bloch sphere as the planet earth, with the north pole representing state  $|0\rangle$  and the south pole representing state  $|1\rangle$  by convention. To represent a pure state  $|\psi\rangle$  on the Bloch sphere, we further constrain that  $|\alpha|^2 + |\beta|^2 = 1$ , i.e., the corresponding Bloch vector has its endpoint on the surface of the Bloch sphere.

If the Cartesian coordinate system as depicted in Figure 3-1b is utilized to describe a Bloch vector representing the pure state  $|\psi\rangle$ , the coordinates are  $[\sin \theta \cos \phi, \sin \theta \sin \phi, \cos \theta]$ . Here,  $0 \leq \theta \leq \pi$  is the polar angle and  $0 \leq \phi \leq 2\pi$  is the azimuthal angle. It can be shown that state  $|\psi\rangle$  can also be written as

$$|\psi\rangle = \alpha|0\rangle + \beta|1\rangle = \cos \frac{\theta}{2} |0\rangle + e^{i\phi} \sin \frac{\theta}{2} |1\rangle \quad (3.1)$$

Alternatively, we could use the density matrix formalism [27] to represent qubit states. The density matrix of a single qubit can be written as a linear combination

of the 2-by-2 identity matrix  $I$  and the Pauli matrices  $\sigma_x, \sigma_y, \sigma_z$

$$\rho = \frac{1}{2}(I + r_x\sigma_x + r_y\sigma_y + r_z\sigma_z) \quad (3.2)$$

where  $r_x, r_y$  and  $r_z$  correspond to the Cartesian coordinates of the Bloch vector that represents the qubit state, and

$$\sigma_x = \begin{bmatrix} 0 & 1 \\ 1 & 0 \end{bmatrix}, \quad \sigma_y = \begin{bmatrix} 0 & -i \\ i & 0 \end{bmatrix}, \quad \sigma_z = \begin{bmatrix} 1 & 0 \\ 0 & -1 \end{bmatrix} \quad (3.3)$$

Let  $\rho_1$  and  $\rho_2$  be the density matrices representing the states of two qubits. Then the density matrix representing the two-qubit system can be written as

$$\rho_{12} = \rho_1 \otimes \rho_2 \quad (3.4)$$

where  $\otimes$  denotes tensor product.

In order to realize universal quantum computing, at least one entangling gate comprising at least two qubits is required. Therefore, it is of great significance to be able to manipulate a quantum system with multiple qubits. A quantum computer with  $n$  qubits can represent a single quantum superposition state comprising  $2^n$  aspects (classical states) and weight coefficients (probability amplitudes). Quantum parallelism and quantum interference are the foundation for a potentially exponential speed-up compared to classical computing. However, we note one caveat in quantum computing: in order to obtain a final classically readable result, one needs to perform a measurement on the system, which will collapse the quantum superposition state into only one of its constituent classical states (aspects) probabilistically associated with the measurement, and hence some information is lost. Therefore, it is challenging to develop new quantum algorithms that truly manifest the powerful advantage of a quantum computer. We refer the readers to Ref. [27] for more details.

There is a major effect that limits the capability of today's quantum computers, which is commonly referred to as decoherence. If a qubit is completely isolated from

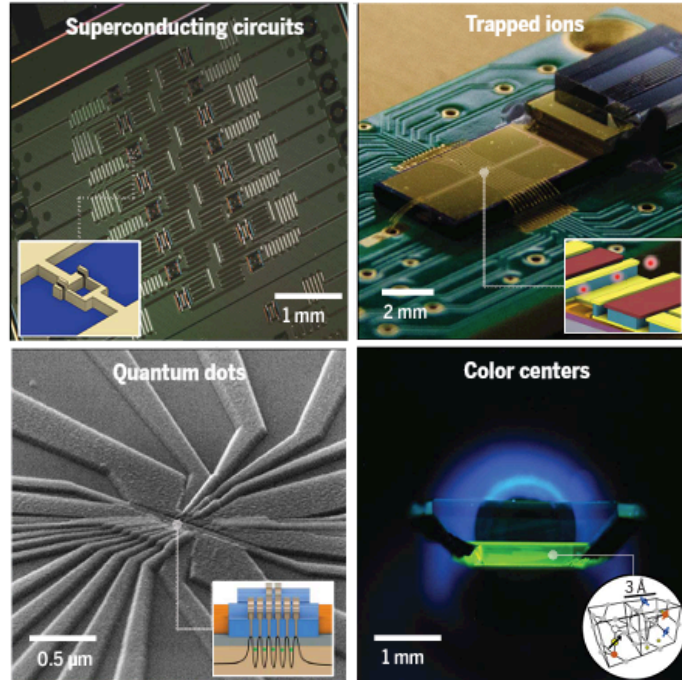


Figure 3-2: Images of four physical hardware platforms for quantum computing. (From left to right, top to bottom) Superconducting circuits, trapped ions, quantum dots, and color centers. Figure from Ref. [28].

its environment, it will preserve its quantum state and quantum information, i.e., maintaining its coherence. However, in practice, a qubit lives in a noisy environment and can never be completely isolated. In addition, control and measurement of a qubit requires the qubit to interact with the control environment. Consequently, the qubit will become entangled with its environment, thereby seemingly losing its information and coherence to uncontrolled degrees of freedom. A qubit's decoherence characteristics can vary depending on the physical realization of the qubit. Figure 3-2 (from Ref. [28]) shows images of several physical realizations, namely superconducting circuits, trapped ions, quantum dots, and color centers. This thesis focuses on the superconducting circuit modality, a leading technology platform in today's quantum computers because of its compatibility with existing microwave engineering and microelectronics fabrication techniques. Relative to trapped ions and other natural atomic systems, the superconducting circuit modality is strongly coupled to its electromagnetic environment, which leads to both faster gates and faster decoherence. For technologies such as superconducting qubits that are essentially limited by their

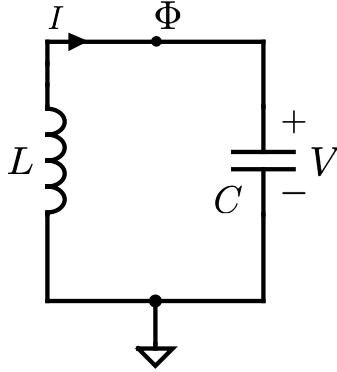


Figure 3-3: Circuit diagram of a linear LC circuit comprising a capacitor with capacitance  $C$  in parallel with an inductor with inductance  $L$ .

decoherence rates, implementing faster gate operations in a proper way directly leads to lower gate error rates. Achieving a faster two-qubit gate without sacrificing the gate fidelity is the goal of this thesis.

## 3.2 Superconducting qubits

In Section 3.2, we explain the basics of using a superconducting circuit to physically realize a qubit. In order to realize a qubit, a quantum system is required to have discrete quantum energy levels corresponding to quantum states that encode logical information and can be controlled. One method is to use a superconducting LC circuit with some additional physical engineering.

### 3.2.1 Quantum LC circuit

An LC circuit is an electrical circuit comprising an inductor  $L$  and capacitor  $C$  in parallel. Figure 3-3 shows the circuit diagram of an LC circuit. Prior to the quantum picture of an LC circuit, we first review the classical picture, or more specifically, the classical Hamiltonian picture of an LC circuit.

In classical mechanics, the Hamiltonian  $H$  is defined through the Legendre transformation applied to the Lagrangian  $L$ , where the Lagrangian  $L$  is defined as the ex-

cess of the kinetic energy  $T$  with respect to the potential energy  $U$ , i.e.,  $L = T - U$  [29]. The procedure to derive the Hamiltonian  $H$  of a classical system is as follows:

1. Choose  $n$  generalized position coordinates  $q_i$ ,  $i = 1, 2, \dots, n$  and their time derivatives,  $n$  generalized velocity coordinates  $\dot{q}_i$ ,  $i = 1, 2, \dots, n$ , that classically specify the state of the system.
2. Write the potential and kinetic energies as functions of the chosen coordinates and (implicitly) time  $t$ , and therefore the Lagrangian  $L = T - U = L(q_1, q_2, \dots, q_n; \dot{q}_1, \dot{q}_2, \dots, \dot{q}_n; t)$ .
3. Introduce the generalized momentum coordinates  $p_i = \frac{\partial L}{\partial \dot{q}_i}$ ,  $i = 1, 2, \dots, n$ .
4. Define the Hamiltonian as  $H = \sum_{i=1}^n p_i \dot{q}_i - L$  and write the Hamiltonian as a function of  $q_i$ ,  $i = 1, 2, \dots, n$ ,  $p_i$ ,  $i = 1, 2, \dots, n$  and (implicitly) time  $t$ , by substituting  $\dot{q}_i$ ,  $i = 1, 2, \dots, n$  through solving  $p_i = \frac{\partial L}{\partial \dot{q}_i}$ .

As depicted in Figure 3-3, in the LC circuit, the node flux  $\Phi(t)$  is chosen as the position coordinate and  $V(t) = \dot{\Phi}(t)$  as the velocity coordinate.  $\Phi(t)$  and  $V(t)$  are related through

$$\Phi(t) = \int_{-\infty}^t V(t') dt' \quad \Leftrightarrow \quad V(t) = \frac{d\Phi(t)}{dt} = \dot{\Phi}(t) \quad (3.5)$$

where  $V(t)$  is the voltage across the inductor (and the capacitor) and  $\Phi(t)$  is associated with the magnetic flux in the inductor.  $I(t)$  is the current in the circuit. For a capacitor with capacitance  $C$  and an inductor with inductance  $L$ , the voltage  $V(t)$  and current  $I(t)$  are related through

$$V(t) = L \frac{dI(t)}{dt} \quad (3.6)$$

$$I(t) = C \frac{dV(t)}{dt} \quad (3.7)$$

With the instantaneous, time-dependent energy  $E(t)$  in each electrical element derived

from its current  $I(t)$  and voltage  $V(t)$

$$E(t) = \int_{-\infty}^t V(t')I(t')dt' \quad (3.8)$$

we can express the energy of the inductor and capacitor as

$$E_L(t) = \frac{1}{2L}\Phi(t)^2 = U(t) \quad (3.9)$$

$$E_C(t) = \frac{C}{2}\dot{\Phi}(t)^2 = T(t) \quad (3.10)$$

which can be referred to as the potential energy and kinetic energy. Note that here the assignment of kinetic and potential energy terms can be arbitrary.

Therefore, the Lagrangian  $L$  of the LC circuit can be written as

$$L(t) = \frac{C}{2}\dot{\Phi}(t)^2 - \frac{1}{2L}\Phi(t)^2 \quad (3.11)$$

and the conjugate momentum  $Q$  is defined as

$$Q(t) = \frac{\partial L(t)}{\partial \dot{\Phi}(t)} = C\dot{\Phi}(t) \quad (3.12)$$

where  $Q(t)$  corresponds to the charge on the capacitor.

Finally, the Hamiltonian  $H$  of the LC circuit can be written as

$$H(t) = Q(t)\dot{\Phi}(t) - L(t) = \frac{1}{2C}Q(t)^2 + \frac{1}{2L}\Phi(t)^2 \quad (3.13)$$

From this point on, we will drop the implicit time variable  $t$  for brevity. Having derived the Hamiltonian of a classical LC circuit, we would like to further quantize the Hamiltonian in a quantum picture. In experiments, if we cool an LC circuit below a critical temperature of certain metals, the metals that comprise the circuit become superconducting, that is, they exhibit zero direct current (DC) resistance (no dissipation). Provided the intrinsic and extrinsic dissipation is sufficiently low, the LC circuit exhibits discrete, quantized energy levels. In the Hamiltonian formalism, it is

intuitive to extend a classical Hamiltonian to a quantum Hamiltonian by substituting quantum operators for the classical variables  $Q$  and  $\Phi$ : the charge operator  $\hat{Q}$  and the flux operator  $\hat{\Phi}$ , which satisfy the commutation relation [26]

$$[\hat{\Phi}, \hat{Q}] = \hat{\Phi}\hat{Q} - \hat{Q}\hat{\Phi} = i\hbar \quad (3.14)$$

where  $\hbar$  denotes the reduced Planck constant.

By defining the reduced flux operator  $\hat{\phi} = 2\pi\hat{\Phi}/\Phi_0$  and the reduced charge operator  $\hat{n} = \hat{Q}/2e$ , we can rewrite the quantum Hamiltonian as

$$\hat{H} = \frac{1}{2C}\hat{Q}^2 + \frac{1}{2L}\hat{\Phi}^2 = 4E_C\hat{n}^2 + E_L\hat{\phi}^2 \quad (3.15)$$

where  $E_C = e^2/2C$  is the capacitive charging energy required to add a single electron to one side of the capacitor, and  $E_L = (\Phi_0/2\pi)^2/L$  is the inductive energy required to add a single magnetic flux quantum  $\Phi_0 = h/2e$  to the inductor. Here,  $h$  denotes the Planck constant. The commutation relation  $[\hat{n}, \hat{\phi}] = i$  is satisfied.

We can further express the quantum Hamiltonian in the basis of the raising (creation) and lowering (annihilation) operators  $a^\dagger$ ,  $a$

$$\hat{H} = \hbar\omega_r(a^\dagger a + \frac{1}{2}) \quad (3.16)$$

where  $\omega_r = 1/\sqrt{LC}$  denotes the resonant frequency of the LC circuit and  $a^\dagger$ ,  $a$  are related to  $\hat{n}$ ,  $\hat{\phi}$  through

$$\hat{\phi} = \left(\frac{2E_C}{E_L}\right)^{\frac{1}{4}}(a + a^\dagger) \quad (3.17)$$

$$\hat{n} = \frac{i}{2}\left(\frac{E_L}{2E_C}\right)^{\frac{1}{4}}(a - a^\dagger) \quad (3.18)$$

If we diagonalize the Hamiltonian of the quantum LC circuit, the solution is a series of eigenstates whose corresponding eigenenergies  $E_k$ ,  $k = 0, 1, 2, \dots$  are spaced by equal distance, i.e.,  $E_{k+1} - E_k = \hbar\omega_r$ , as shown in the left plot of Figure 3-4

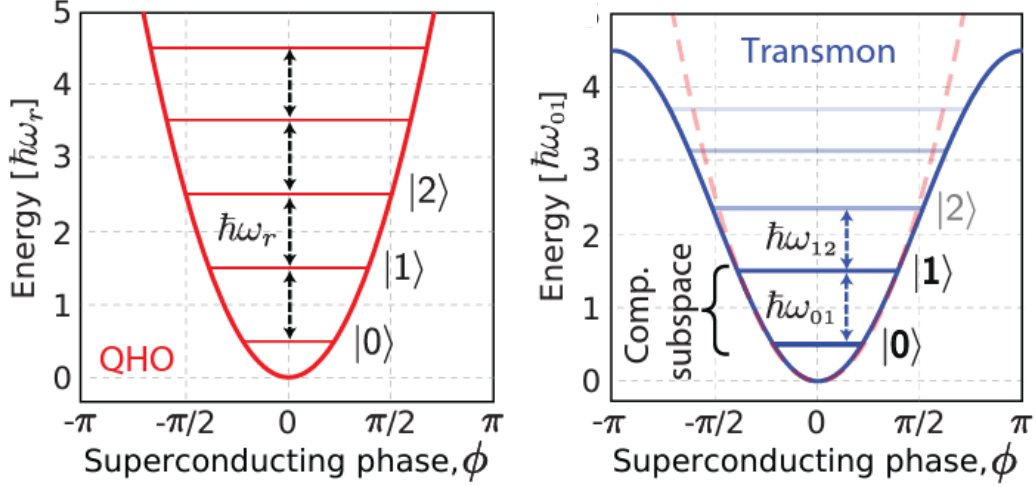


Figure 3-4: Energy potential and levels of a quantum LC circuit (quantum harmonic oscillator, or QHO) v.s. a transmon with a Josephson junction. The energy potential of a QHO is of a quadratic form and the energy levels are separated equidistantly. By introducing a Josephson junction, the energy potential of a transmon is reshaped into a cosinusoidal form and the energy levels are no longer equidistant. Figure from Ref. [30].

(from Ref. [30]). In practice, the quantum LC circuit, also known as the quantum harmonic oscillator (QHO), is not a good candidate for a qubit, because it is difficult to address only the transition between a particular pair of levels (in particular  $|0\rangle$  and  $|1\rangle$ ) without addressing other transitions. Therefore, a computational subspace cannot be uniquely defined and addressed. In the next few sections, we describe how physicists have resolved this problem by replacing the linear inductor in the LC circuit with a nonlinear inductor known as the Josephson junction.

### 3.2.2 Josephson junction

A Josephson junction [31] is a tunnel junction realized by a thin insulating barrier between two superconducting electrodes. The Josephson junction is described by the

Josephson current-phase and voltage-phase relationships

$$I(t) = I_c \sin \phi(t) \quad (3.19)$$

$$V(t) = \frac{\hbar}{2e} \frac{d\phi(t)}{dt} \quad (3.20)$$

where  $I_c$  is the critical current of the junction, i.e., the maximum sustainable current before Cooper pairs are broken.  $I(t)$  is the supercurrent through the junction, and  $V(t)$  is the voltage across the junction.  $\phi(t)$  is the reduced flux, as mentioned earlier, and is referred to as the superconducting phase difference across the junction in the context of superconductivity [32].

The effective inductance of the Josephson junction can then be written as

$$L_J = \frac{V(t)}{dI(t)/dt} = \frac{\frac{\hbar}{2e} \frac{d\phi(t)}{dt}}{I_c \cos \phi(t) \frac{d\phi(t)}{dt}} = \frac{\Phi_0}{2\pi I_c \cos \phi(t)} \quad (3.21)$$

where  $\Phi_0 = h/2e$ . The effective inductance is a function of  $\phi(t)$  and, therefore, the Josephson junction is a nonlinear inductor, which can be used to impart nonlinearity in the LC circuit. The energy of the Josephson junction is

$$E_{JJ}(t) = \int_{-\infty}^t V(t')I(t')dt' = \frac{I_c\Phi_0}{2\pi}(1 - \cos \phi(t)) = E_J(1 - \cos \phi(t)) \quad (3.22)$$

where  $E_J = I_c\Phi_0/2\pi$  is referred to as the Josephson energy. This cosine potential corresponds to an anharmonic oscillator and should be contrasted with the parabolic potential of the quantum harmonic oscillator (the linear LC circuit).

### 3.2.3 Transmon qubit

A transmon qubit can be built by replacing the linear inductor in an LC circuit with a Josephson junction. The circuit parameters are chosen such that  $E_J/E_C \gg 1$  ( $E_J/E_C \approx 50$  in common cases) [33]. The circuit diagram of a transmon qubit is shown in Figure 3-5a. The quantum Hamiltonian of a transmon qubit can then be written as follows by replacing the kinetic energy term associated with the linear

inductor in Eq. 3.15 with Eq. 3.22

$$\hat{H} = 4E_C \hat{n}^2 + E_J(1 - \cos \hat{\phi}) \quad (3.23)$$

where  $E_C = 2e/C_\Sigma$  and  $C_\Sigma = C_s + C_J$  is a sum of the shunt capacitance  $C_s$  and the capacitance of the Josephson junction  $C_J$ . Note that the kinetic energy term is no longer a quadratic form of  $\hat{\phi}$  as in the LC circuit, but a cosinusoidal function of  $\hat{\phi}$ , which breaks the equidistantly spaced energy levels as shown in the right plot of Figure 3-4 (from Ref. [30]). In terms of constructing a transmon qubit, we are particularly interested in the lowest two energy levels, namely the ground state  $|0\rangle$  and the first excited state  $|1\rangle$ . The qubit frequency  $\omega_q$  is given by

$$\omega_q = \omega_1 - \omega_0 \approx \frac{\sqrt{8E_J E_C} - E_C}{\hbar} \quad (3.24)$$

where  $\omega_1 - \omega_0$  is the transition frequency between states  $|0\rangle$  and  $|1\rangle$ , and  $\omega_k$  denotes the energy of state  $|k\rangle$ . We define the anharmonicity  $\alpha = \omega_q - \omega_{12}$  as the difference between the qubit frequency  $\omega_q = \omega_1 - \omega_0$  and the transition frequency  $\omega_{12} = \omega_2 - \omega_1$  between the first and second excited states  $|1\rangle$  and  $|2\rangle$ .

Eq. 3.23 can be rewritten by performing a Taylor series expansion of the cosine term

$$\hat{H} = 4E_C \hat{n}^2 + \frac{1}{2} E_J \hat{\phi}^2 - \frac{1}{24} E_J \hat{\phi}^4 + \mathcal{O}(\hat{\phi}^6) \quad (3.25)$$

which can be viewed as a modification to the quantum Hamiltonian of the LC circuit in Eq. 3.15. Including up to terms of  $\hat{\phi}^4$  and writing in terms of the same eigenbasis as the Hamiltonian in Eq. 3.16 using the raising (creation) and lowering (annihilation) operators  $a^\dagger$ ,  $a$ , we have

$$\hat{H} = \hbar\omega_q a^\dagger a + \frac{\hbar\alpha}{2} a^\dagger a^\dagger a a \quad (3.26)$$

To further simplify, the quantum Hamiltonian of a transmon qubit in its own basis (along its own quantization axis  $z$ ) can be written for a two level system as

$$\hat{H} = \frac{\hbar\omega_q}{2} \sigma_z \quad (3.27)$$

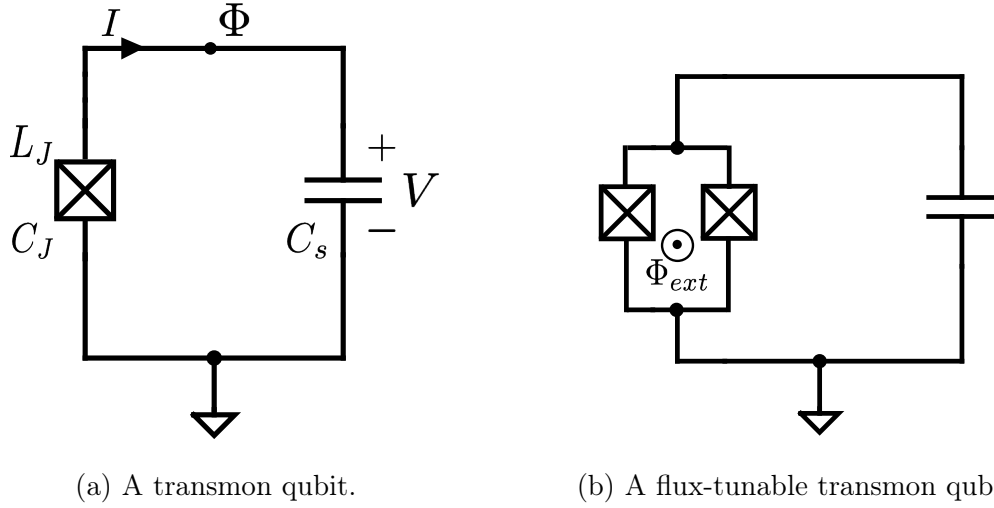


Figure 3-5: A transmon qubit v.s. a flux-tunable transmon qubit. (a) Circuit diagram of a transmon qubit comprising a capacitor with capacitance  $C_s$  in parallel with a Josephson junction with inductance  $L_J$  and self-capacitance  $C_J$ . (b) Circuit diagram of a flux-tunable transmon comprising a capacitor in parallel with a SQUID loop. The SQUID loop comprises two Josephson junctions in parallel with some external magnetic flux  $\Phi_{\text{ext}}$  threading the loop.

where  $\sigma_z$  is the Pauli- $z$  operator.

A frequency-tunable transmon qubit can be obtained by replacing the Josephson junction in the circuit of a transmon qubit with a SQUID loop comprising two Josephson junctions in parallel, where SQUID is short for superconducting quantum interference device. The magnetic flux  $\Phi_{\text{ext}}$  threading the SQUID loop changes the effective Josephson energy and thus tunes the frequency of the qubit. For example, for a symmetric SQUID loop, which comprises two same Josephson junction in parallel, the qubit frequency is given by

$$\omega(\Phi_{\text{ext}}) \approx \frac{1}{\hbar} \left( \sqrt{8E'_J E_C \left| \cos\left(\pi \frac{\Phi_{\text{ext}}}{\Phi_0}\right) \right|} - E_C \right) \quad (3.28)$$

where  $E'_J$  is the sum of the Josephson energies of the two symmetric junctions,  $E_C$  is the charging energy, and  $\Phi_0$  is the superconducting flux quantum. Figure 3-5b shows the circuit diagram of a flux-tunable transmon qubit.

## 3.3 Quantum gates

As Boolean logic gates are used as the basic computation units in classical computing, so are quantum gates used as the basic computation units in quantum computing. In Section 3.3 we briefly introduce single-qubit gates and two-qubit gates. We will comment that a small number of single-qubit gates and two-qubit gates are sufficient for universal quantum computing.

### 3.3.1 Single-qubit gates

As discussed in Section 3.1, a pure quantum state can be represented by a point (endpoint of the Bloch vector) on the surface of the Bloch sphere. Single-qubit gates are rotations of the Bloch vector around the Bloch sphere, which translates an arbitrary quantum state from a point to another point on the Bloch sphere by rotating a certain angle about a particular axis. Here, we review the single-qubit rotations by angle  $\theta$  around the  $x$ ,  $y$  and  $z$  axes, represented by 2-by-2 matrices written in terms of the eigenbasis of the  $\sigma_z$  operator, i.e.,  $|0\rangle = [1, 0]^T$ ,  $|1\rangle = [0, 1]^T$

$$R_x(\theta) = \begin{bmatrix} \cos \theta/2 & -i \sin \theta/2 \\ -i \sin \theta/2 & \cos \theta/2 \end{bmatrix} \quad (3.29)$$

$$R_y(\theta) = \begin{bmatrix} \cos \theta/2 & -\sin \theta/2 \\ \sin \theta/2 & \cos \theta/2 \end{bmatrix} \quad (3.30)$$

$$R_z(\theta) = \begin{bmatrix} e^{-i\theta/2} & 0 \\ 0 & e^{i\theta/2} \end{bmatrix} \quad (3.31)$$

When  $\theta = \pi$ , these three single-qubit gates are referred to as the X gate, Y gate and Z gate, respectively, up to a global phase difference. If a single-qubit gate is represented by a matrix  $U_{\text{rot}}$ , then state  $|\psi\rangle$  is transformed into  $U_{\text{rot}}|\psi\rangle$  after the single-qubit gate operation.

### 3.3.2 Two-qubit gates

Two-qubit entangling gates are operations between two qubits that can create entanglement between them, depending on the initial qubit states. The operation can be represented by 4-by-4 matrices that serve as rotations around some higher dimension axes. For example, one notable two-qubit gate is the controlled-Z (CZ) gate, a specific case of the controlled phase (CPHASE) gate, which is the focus of this thesis. The CZ gate can be obtained by a  $z \otimes z$  axis interaction followed by single-qubit gates to correct any residual single-qubit phase offsets inadvertently acquired during the implementation of the two-qubit gate

$$\text{CZ} = e^{i\frac{\pi}{4}(\sigma_z \otimes \sigma_z - \sigma_z \otimes I - I \otimes \sigma_z + I \otimes I)} = \begin{bmatrix} 1 & 0 & 0 & 0 \\ 0 & 1 & 0 & 0 \\ 0 & 0 & 1 & 0 \\ 0 & 0 & 0 & -1 \end{bmatrix} \quad (3.32)$$

Other two-qubit gates include iSWAP gate, the CNOT gate, etc. Note that the CNOT gate can be built from either the CZ gate or the iSWAP gate. We refer the readers to Ref. [30] for more details. Similarly, if a two-qubit gate is represented by a matrix  $U_{\text{rot2}}$ , then state  $|\psi\rangle$  is transformed into  $U_{\text{rot2}}|\psi\rangle$  after the two-qubit gate operation. Implementation of fast and high-fidelity two-qubit gates is of significance and remains a challenge in today's quantum computers.

### 3.3.3 Universal gate set

According to the Solvay-Kitaev theorem [34, 35], an arbitrary quantum operation can be realized to arbitrary accuracy with a generally small set of single-qubit and two-qubit gates, referred to as a universal gate set. There are many such universal gate sets,  $\{\text{R}_x(\theta), \text{R}_y(\theta), \text{R}_z(\theta), \text{Ph}(\theta), \text{CZ}\}$  being one of those, where  $\text{Ph}(\theta) = e^{i\theta} I$  gives an overall phase  $\theta$  to a single qubit.

### 3.4 The CPHASE gate in tunable transmon qubits

Having introduced the physics of transmon qubits and the concepts of quantum gates, we will focus on the CPHASE gate and describe in detail a common implementation using baseband pulses applied to tunable qubits in Section 3.4. We then discuss some characteristics of the CPHASE gate.

The CPHASE gate is a two-qubit gate whose operation is represented by the unitary matrix

$$U_{\text{CPHASE}} = \begin{bmatrix} 1 & 0 & 0 & 0 \\ 0 & 1 & 0 & 0 \\ 0 & 0 & 1 & 0 \\ 0 & 0 & 0 & e^{i\phi} \end{bmatrix} \quad (3.33)$$

The CPHASE gate adds a term  $e^{i\phi}$  to the qubits only when both are in the excited state, namely  $|11\rangle$ . To be more specific, if the original state of the qubits is  $|00\rangle$ ,  $|01\rangle$  or  $|10\rangle$ , the CPHASE gate effectively does nothing. If the original state of the qubits is  $|11\rangle$ , it will be transformed into  $e^{i\phi}|11\rangle$  after the CPHASE gate operation.

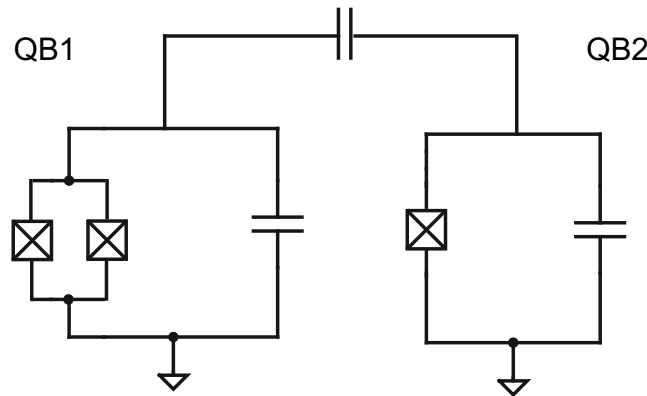


Figure 3-6: Circuit diagram of a flux-tunable transmon capacitively coupled to a fixed-frequency transmon. The flux-tunable transmon is referred to as QB1 and the fixed-frequency transmon is referred to as QB2.

One implementation of the CPHASE gate relies on the avoided crossing between states  $|11\rangle$  and  $|20\rangle$  that occurs when two transmon qubits are coupled to each other.

Consider a system of two capacitively coupled qubits as depicted in Figure 3-6, where QB1 is a flux-tunable transmon qubit while QB2 is a fixed-frequency transmon qubit. The Hamiltonian - including states with two excitations in addition to the four computational states - can be written in the  $|00\rangle, |01\rangle, |10\rangle, |11\rangle, |02\rangle, |20\rangle$ -basis as

$$H = \begin{bmatrix} E_{00} & 0 & 0 & 0 & 0 & 0 \\ 0 & E_{01} & g & 0 & 0 & 0 \\ 0 & g & E_{10} & 0 & 0 & 0 \\ 0 & 0 & 0 & E_{11} & \sqrt{2}g & \sqrt{2}g \\ 0 & 0 & 0 & \sqrt{2}g & E_{02} & 0 \\ 0 & 0 & 0 & \sqrt{2}g & 0 & E_{20} \end{bmatrix} \quad (3.34)$$

where  $E_{ij}$  is the energy of state  $|ij\rangle$  and  $g$  is the coupling strength with a factor of  $\sqrt{n}$  corresponding to the number of qubit excitations ( $n = 1, 2$ ). Note that the frequency of QB1, and therefore the energies  $E_{ij}$ , depend on the external magnetic flux threading the SQUID loop. Figure 3-7 shows an example of the energy spectrum diagram of the system described by the Hamiltonian in Eq. 3.34 as a function of the frequency detuning of QB1.

The CPHASE gate is implemented by detuning the frequency of QB1 such that the instantaneous energy of state  $|11\rangle$  follows the trajectory  $l(t)$  in Figure 3-7. To be more specific, we shift the frequency of QB1, in particular the energy of state  $|11\rangle$ , bringing it into resonance with state  $|20\rangle$ , which opens an avoided crossing due to the coupling. We then rewind the trajectory and return to the starting point. We note that due to the presence of the avoided crossing, the energy of state  $|11\rangle$  is pushed lower than would be expected in an uncoupled system. This is the origin of an additional phase accumulation that only occurs for state  $|11\rangle$ , leading to the conditional phase accumulation. The frequency detuning  $d\omega$  of QB1 is defined as  $d\omega = \omega_{\text{ini}} - \omega_1$ , where  $\omega_{\text{ini}}$  is the initial frequency of QB1 and  $\omega_1$  is the instantaneous frequency of

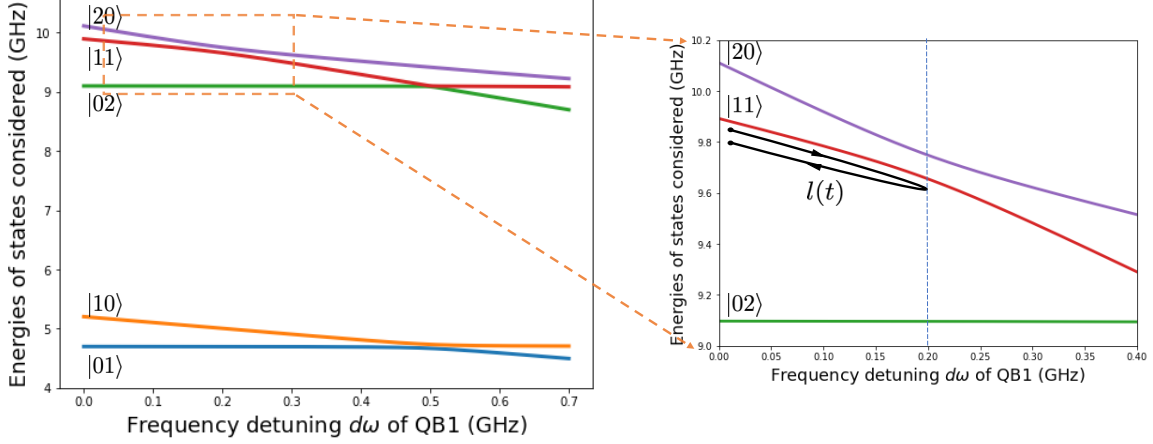


Figure 3-7: An example of the energy spectrum diagram of two coupled transmons as depicted in Figure 3-6 as the frequency of QB1 is detuned by changing the local magnetic flux that threads its SQUID loop. The frequency detuning  $d\omega$  of QB1 is defined as  $d\omega = \omega_{\text{ini}} - \omega_1$ , where  $\omega_{\text{ini}}$  is the initial frequency of QB1 and  $\omega_1$  is the instantaneous frequency of QB1. The avoided crossing between the states  $|11\rangle$  and  $|20\rangle$  indicated in the orange box in the left plot is used to implement the CPHASE gate. The right plot is a zoom-in plot around the avoided crossing of interest, where  $l(t)$  represents a typical trajectory of the instantaneous energy of state  $|11\rangle$  during the process of the CPHASE gate. The parameters used to generate this energy diagram are  $\omega_1 = 5.2$ ,  $\omega_2 = 4.7$ ,  $\alpha_1 = \alpha_2 = -0.3$ ,  $g = 0.033$  (GHz).

QB1. This process can be represented by a unitary matrix in the computational basis

$$U_{\text{raw}} = \begin{bmatrix} 1 & 0 & 0 & 0 \\ 0 & e^{i\phi_{01}} & 0 & 0 \\ 0 & 0 & e^{i\phi_{10}} & 0 \\ 0 & 0 & 0 & e^{i\phi_{11}} \end{bmatrix} \quad (3.35)$$

where  $\phi_{ij}$  is the accumulated phase

$$\phi_{ij} = \int_0^\tau \omega_{ij}(t) dt \quad (3.36)$$

with  $\tau$  denoting the duration of the process.

In order to obtain the CPHASE gate as in Eq. 3.33, two single-qubit gates  $R_z(-\phi_{01})$  and  $R_z(-\phi_{10})$  need to be implemented to each qubit to cancel the phase ac-

cumulated by states  $|01\rangle$  and  $|10\rangle$ . Therefore, the whole operation can be represented by

$$U'_{\text{CPHASE}} = \begin{bmatrix} 1 & 0 & 0 & 0 \\ 0 & 1 & 0 & 0 \\ 0 & 0 & 1 & 0 \\ 0 & 0 & 0 & e^{i\phi'} \end{bmatrix} \quad (3.37)$$

where  $\phi' = \phi_{11} - \phi_{01} - \phi_{10}$ . If there were no coupling between the two qubits,  $\phi' = 0$ . Because of the effect of the coupling between the two qubits, a nonzero phase will be acquired. The way the instantaneous energy of state  $|11\rangle$  is varied determines the value of  $\phi'$ . By choosing a suitable  $l(t)$  as depicted in Figure 3-7, in principle we can always have  $\phi' = \phi$  for any arbitrary desired phase  $\phi$ .

Two important factors in this process are the leakage error and gate duration. Leakage error refers to unwanted leakage of the qubit population outside of the computational subspace, especially in this context the leakage from  $|11\rangle$  to  $|20\rangle$  since they are intentionally brought into resonance. Therefore, the trajectory must be designed to be sufficiently slow in order for the leakage error to be sufficiently small. This is true if we want to implement the CPHASE gate adiabatically, or in the adiabatic limit. There are other approaches, which are different from the one studied in this thesis, referred to as non-adiabatic implementations, where leakage and quantum interference is intentionally leveraged to realize a faster two-qubit gate. On the other hand, due to the decoherence and limited coherence of the qubits, faster gates are desired so that more gates with high fidelity can be implemented within a certain time. In other words, the process is also expected to be fast and the gate duration should be small. Furthermore, as these two factors are somewhat contradictory, a compromise needs to be made at some point, which will be discussed in more detail in Chapter 4. Now the problem is transformed to design a pulse to tune the frequency of QB1 and thus design the trajectory  $l(t)$  as depicted in Figure 3-7. In this thesis, as we will explain in more detail in Section 4.5, we refer to this problem as the pulse design or control trajectory design problem. An immediate question to ask is whether there exists an optimal control trajectory for this problem and if so under which optimality

criterion. We will provide a perspective and solution in this thesis.

### 3.5 Review of efforts on control trajectory design

Previous research has explored multiple methods to design pulses to implement the flux-based CZ gate in the adiabatic limit, some of which have been experimentally shown to be effective.

One of the widely implemented pulses is detailed in Ref. [36], where the authors propose an adiabatic CZ gate that is fast and incurs low error. The associated control trajectory is designed based on the Slepian pulse. The method is experimentally demonstrated to reach a CZ gate fidelity up to 99.4% in Ref. [37]. In Ref. [38], Rol et al. develop a bipolar flux pulse named the “Net Zero (NZ)” pulse, which is more robust to long time distortions in the control line compared to unipolar ones such as in Ref. [36]. Building upon Ref. [38], Ref. [39] develops a variation of the NZ CZ gate, which achieves more tune-up simplicity. Ref. [40] utilizes the Slepian-based control trajectory to implement the (non-adiabatic) CZ gate in a more sophisticated system consisting of two transmon qubits coupled with a tunable coupler. Ref. [41] also studies the CZ gate in a system with a tunable coupler and proposed a modified control trajectory by adding prefactor weights to the Slepian-based control trajectory. Another general approach, e.g., as demonstrated in Ref. [42], is to perform experiments using closed-loop feedback to evaluate the current gate performance according to some metrics and then numerically optimize the pulse.

# Chapter 4

## Problem Formulation and Optimality Criterion

In Chapter 4, we mathematically formulate the CPHASE gate design in superconducting qubits as a pulse design problem, and further as a control trajectory design problem. Specifically, we discuss the abstraction of the multi-level physical process into a two-level system evolution in Section 4.1. We derive a formula for the accumulated phase and leakage error in the context of the two-level system in Section 4.2 and 4.3. We then characterize two scenarios of the problem considered in Section 4.4. In Section 4.5 we propose a preliminary optimization problem over the pulse duration and transform the optimization problem into the frequency domain, which becomes more tractable. Additionally, we comment on the conversion from a continuous-time problem, which is intrinsic to the physical world, into a discrete-time problem, which is required for digital processing and implementation.

### 4.1 A two-level system abstraction

The ultimate goal of this research is to design optimized baseband flux pulses to implement fast and high-fidelity CPHASE gates in superconducting qubits. We are mainly concerned about the leakage error taking place from  $|11\rangle$  to  $|20\rangle$  throughout the process. Therefore, we abstract the problem involving multiple energy levels to a

problem with two energy levels  $|11\rangle$  and  $|20\rangle$  while omitting other weaker interactions that may take place in the larger space. In Chapter 6, however, we will simulate the whole system including other relevant energy levels. In the remaining chapters, we will drop the “hat” notation and write the quantum Hamiltonian  $\hat{H}$  as  $H$  for brevity without causing confusion.

Consider a two-level system whose Hamiltonian is defined as

$$H = \frac{\varepsilon(t)}{2}\sigma_z + \frac{\Delta}{2}\sigma_x = \frac{1}{2} \begin{bmatrix} \varepsilon(t) & \Delta \\ \Delta & -\varepsilon(t) \end{bmatrix} \quad (4.1)$$

where  $\Delta$  is a constant denoting the coupling strength, and  $\varepsilon(t)$  is a function of time, which dictates the difference between the two eigenenergies. Of particular interest are the two eigenstates  $|\psi_{11}\rangle$ ,  $|\psi_{20}\rangle$  and the corresponding eigenenergies  $E_{11}$ ,  $E_{20}$  of this system. Solve for the eigen-problem of  $H$ , and we will have

$$|\psi_{11}\rangle = \begin{bmatrix} \cos(\theta(t)/2) \\ \sin(\theta(t)/2) \end{bmatrix} \quad (4.2a)$$

$$|\psi_{20}\rangle = \begin{bmatrix} -\sin(\theta(t)/2) \\ \cos(\theta(t)/2) \end{bmatrix} \quad (4.2b)$$

$$E_{11} = -\sqrt{\varepsilon(t)^2 + \Delta^2}/2 \quad (4.2c)$$

$$E_{20} = \sqrt{\varepsilon(t)^2 + \Delta^2}/2 \quad (4.2d)$$

where  $\theta(t)$  is defined as

$$\theta(t) = \arctan \frac{\Delta}{\varepsilon(t)} \quad (4.3)$$

Later, in Section 4.3.1, it turns out that  $\theta(t)$  has a geometric meaning in the picture of the Bloch sphere.  $\theta(t)$  is also an intermediate control variable whose trajectory is to be designed, as we will reveal in Section 4.5.

Figure 4-1 depicts the eigenenergies of the two-level system with Hamiltonian  $H$  as a function of  $\varepsilon(t) \in [-\infty, +\infty]$ .  $\varepsilon(t)$  can be interpreted as the energy difference

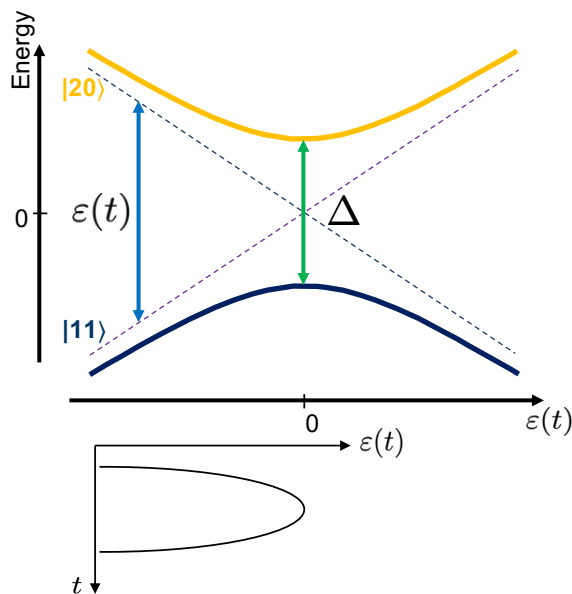


Figure 4-1: Eigenenergies of the two-level system with Hamiltonian  $H$  as a function of  $\varepsilon(t)$ . In the upper plot, the dashed lines represent the states  $|11\rangle$  and  $|20\rangle$  when they are uncoupled, i.e.,  $\Delta = 0$  (we may also refer to the states as diabatic states in this case); the solid lines represent the states  $|11\rangle$  and  $|20\rangle$  when they are coupled, i.e.,  $\Delta > 0$ . The lower plot shows an example of a typical trajectory for  $\varepsilon(t)$  to implement a CPHASE gate in the abstracted two-level system.

between  $|11\rangle$  and  $|20\rangle$  when  $\Delta = 0$ , i.e., when the two energy levels are uncoupled (we may also refer to the states as diabatic states in this case).  $\Delta$  can be interpreted as the energy difference between the eigenstates of the coupled states  $|11\rangle$  and  $|20\rangle$  at the avoided crossing when  $\varepsilon(t) = 0$ .

In Section 3.4, we briefly mentioned the design of a pulse to tune the instantaneous energy of state  $|11\rangle$  and thus the design of the trajectory  $l(t)$  as depicted in Figure 3-7. In this abstracted two-level system, the problem transforms into preparing the system in the initial state  $|11\rangle$  and designing  $\varepsilon(t)$  to vary the instantaneous energy as depicted in the lower plot of Figure 4-1. Conceptually speaking, the process is expected to incur low leakage error while being preferably fast. However, these two properties are generally contradictory: if the process is too fast, it will typically induce a larger leakage error. We will discuss details, especially which optimality criterion to consider in this abstracted two-level system, in Section 4.5.

## 4.2 A formula for the accumulated phase

As mentioned in Section 3.4, a first characteristic of the CPHASE gate is to accumulate some phase  $\phi$ . We show a formula for the accumulated phase  $\phi$  in the abstracted two-level system.

Recall that in Section 4.1, the Hamiltonian is defined as in Eq. 4.1 and the eigenenergies are given in Eq. 4.2. Now let  $\Delta = 0$  and we will have a Hamiltonian where no coupling exists between the two levels. The eigenenergies are  $E'_{11} = -\varepsilon(t)/2$  and  $E'_{20} = \varepsilon(t)/2$ , as depicted by the dashed lines in Figure 4-1. The difference between the eigenenergies of the ground state  $\Delta E = E_{11} - E'_{11}$  with and without coupling is what contributes to the phase accumulation in the CPHASE gate. Recall that in Eq. 4.3, we defined an intermediate variable  $\theta(t) = \arctan(\Delta/\varepsilon(t))$ . We can then rewrite the eigenenergy difference as

$$\begin{aligned}
 \Delta E &= E_{11} - E'_{11} = \frac{1}{2}(\varepsilon(t) - \sqrt{\varepsilon(t)^2 + \Delta^2}) \\
 &= \frac{\Delta}{2} \left( \frac{\varepsilon(t)}{\Delta} - \sqrt{\frac{\varepsilon(t)^2}{\Delta^2} + 1} \right) \\
 &= \frac{\Delta}{2} \left( \frac{1}{\tan \theta(t)} - \sqrt{\frac{1}{\tan^2 \theta(t)} + 1} \right) \\
 &= -\frac{\Delta}{2} \tan \frac{\theta(t)}{2}
 \end{aligned} \tag{4.4}$$

The accumulated phase  $\phi$  is the integral of the energy difference  $\Delta E$  through the process

$$\phi = \int \Delta E dt = - \int \frac{\Delta}{2} \tan \frac{\theta(t)}{2} dt \tag{4.5}$$

By designing the shape of the control trajectory for  $\theta(t)$  along with its amplitude and duration, we can in principle apply an arbitrary CPHASE gate.

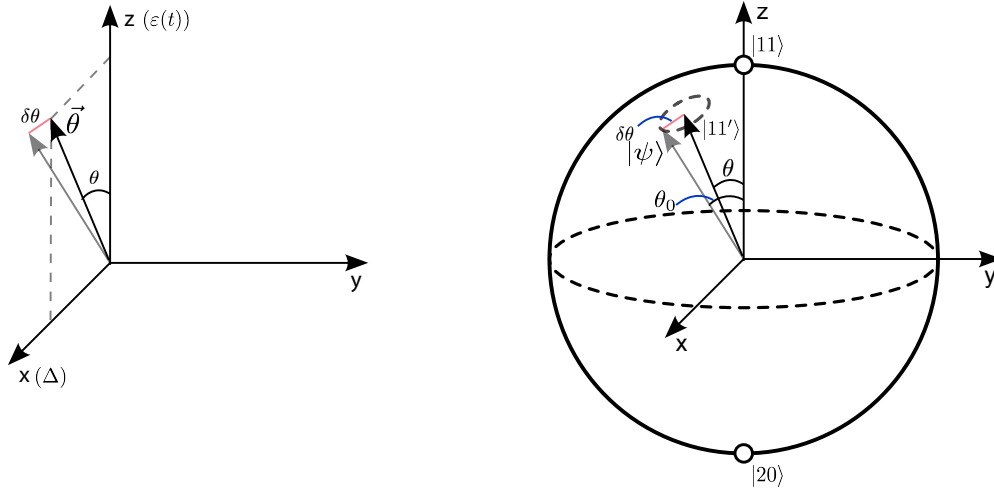
## 4.3 A formula for the leakage error

In Section 4.3, two approaches to calculating the leakage error are presented based on the discussions in Ref. [36]. We first take advantage of the Bloch sphere representation

and give an approximate but more intuitive solution from a geometric perspective. Then we go through a mathematical derivation and provide an analytical formula. We will comment on the efficacy of the formula by discussing the relationship of this formula to the more general Landau-Zener formulation [43, 44].

### 4.3.1 Geometric approach

Recall that in Eq. 4.3,  $\theta(t)$  is defined as  $\theta(t) = \arctan(\Delta/\varepsilon(t))$ . In Figure 4-2a we introduce a control vector  $\vec{\theta}$  representing the control variable  $\theta(t)$  in terms of  $\Delta$  and  $\varepsilon(t)$ . Correspondingly, in Figure 4-2b we show an instantaneous basis vector  $|11'\rangle$ , which represents the ground state of the instantaneous Hamiltonian  $H$  as  $\theta(t)$  varies, in parallel to the control vector  $\vec{\theta}$ . As time progresses, we change our frame reference to coincide with the frame whose basis vectors are the eigenstates of the instantaneous Hamiltonian  $H$ .



(a) Geometry of  $\theta(t)$ .

(b) Bloch sphere picture of the evolution.

Figure 4-2: The geometric definition of  $\theta(t)$  and the Bloch sphere picture of an infinitesimal step of evolution. (a) A control vector  $\vec{\theta}$  representing the control variable  $\theta(t)$  in a coordinate in terms of  $\Delta$  and  $\varepsilon(t)$ . (b) An instantaneous basis vector  $|11'\rangle$  parallel to the control vector  $\vec{\theta}$ . In an infinitesimal time  $\delta t$ , the state vector  $|\psi\rangle$  deviates from the instantaneous basis vector  $|11'\rangle$  by  $-\delta\theta$  and precesses around it.

We first show how the state evolves in an infinitesimal time  $\delta t$ . Suppose the angle between the initial state  $|\psi\rangle$  at time  $t_0$ , represented by the gray Bloch vector in

Figure 4-2b, and the  $z$ -axis is  $\theta_0$ . Ideally,  $|\psi\rangle$  is aligned with the instantaneous ground vector  $|11'\rangle$  at time  $t_0$ . After  $\delta t$ , a  $\delta\theta$  change in the angle between instantaneous ground vector  $|11'\rangle$  and the  $z$ -axis takes place. If we switch into the new reference frame, the state vector  $|\psi\rangle$  deviates from the basis vector by  $-\delta\theta$  and therefore starts to precess around the basis vector at frequency  $\omega$ , where  $\omega$  refers to the eigenenergy difference of the instantaneous Hamiltonian. Therefore, during the infinitesimal time  $\delta t$ , the state vector  $|\psi\rangle$  will pick up a deviation from the ground vector  $|11'\rangle$  by  $\theta_j = -\delta\theta e^{-i\omega_j\delta t}$ .

Next we consider a series of infinitesimal time  $\delta t$ 's. A simple approach is to move into the reference frame along with the control vector  $\vec{\theta}$  and correspondingly the instantaneous ground vector  $|11'\rangle$ . Thus, the whole process can be viewed as the state vector  $|\psi\rangle$  deviating from the basis vector by a series of  $-\delta\theta$ 's with an angle rotation  $-\omega_j\delta t$ . Since the angle rotation is orthogonal to the  $-\delta\theta$  deviation, we can accumulate them independently, i.e.,

$$\theta_{\text{sum}} = \sum_j -\delta\theta_j e^{-i\sum_j \omega_j \delta t} \quad (4.6)$$

Change the  $\sum$  symbol into the  $\int$  symbol and the  $\delta$  symbol into the  $d$  symbol, as in elementary calculus, and we have

$$\theta_{\text{sum}} = - \int d\theta e^{-i \int^t \omega(t') dt'} \quad (4.7)$$

$$= - \int \frac{d\theta}{dt} e^{-i \int^t \omega(t') dt'} dt \quad (4.8)$$

Therefore, the leakage error rate  $P_e$  can be calculated as 1 minus the probability of measuring the state  $|\psi\rangle$  in the instantaneous ground state  $|11'\rangle$

$$P_e = 1 - \left( \cos \frac{|\theta_{\text{sum}}|}{2} \right)^2 = \left( \sin \frac{|\theta_{\text{sum}}|}{2} \right)^2 \approx |\theta_{\text{sum}}|^2/4 \quad (4.9)$$

where the approximation holds valid when  $\theta_{\text{sum}}$  is sufficiently small.

Note that in this geometric derivation we assume that the changes at different

infinitesimal time  $\delta t$ 's can be summed linearly. This approximation holds valid so long as the net overall change  $\theta_{\text{sum}}$  is small. In fact, in this thesis we concentrate on adiabatic control, and therefore, we are always interested in small leakage error rate  $P_e$  incurred throughout the process. This small  $P_e$  corresponds to the fact that  $\theta_{\text{sum}}$  should be small.

### 4.3.2 Analytical approach

We continue to provide an analytical approach to deriving the leakage error. Recall that in Section 4.1, the abstracted two-level system can be described by the Hamiltonian in Eq. 4.1. We have also defined a control variable  $\theta(t) = \arctan(\Delta/\varepsilon(t))$ .

We further require that, first, as  $\varepsilon(t)$  varies from  $-\infty$  to 0,  $\theta(t)$  varies from  $\pi$  to  $\pi/2$  and, second, as  $\varepsilon(t)$  varies from 0 to  $\infty$ ,  $\theta(t)$  varies from  $\pi/2$  to 0. In this way, a one-to-one corresponding relationship is established between  $\varepsilon(t)$  and  $\theta(t)$ . A pictorial representation of the control variable  $\theta(t)$  in terms of  $\Delta$  and  $\varepsilon(t)$  is shown in Figure 4-2a.

Consider a state  $|\psi\rangle$  given by  $|\psi\rangle = \cos \frac{\theta_0}{2} |11\rangle + \sin \frac{\theta_0}{2} |20\rangle$ , where  $|11\rangle$  and  $|20\rangle$  denote the basis vectors of the  $\sigma_z$ -basis ( $z$ -axis). Suppose there exists another basis which rotates around the  $y$ -axis by an angle  $\theta$  relative to the  $\sigma_z$ -basis ( $z$ -axis). In this new basis, the state  $|\psi\rangle$  can be rewritten as

$$|\psi\rangle = \cos \frac{\theta_0 - \theta}{2} |11'\rangle + \sin \frac{\theta_0 - \theta}{2} |20'\rangle = \bar{\alpha} |11'\rangle + \bar{\beta} |20'\rangle \quad (4.10)$$

where

$$\bar{\alpha} = \cos \frac{\theta_0 - \theta}{2} = \cos \frac{\theta_0}{2} \cos \frac{\theta}{2} + \sin \frac{\theta_0}{2} \sin \frac{\theta}{2} \quad (4.11a)$$

$$\bar{\beta} = \sin \frac{\theta_0 - \theta}{2} = \sin \frac{\theta_0}{2} \cos \frac{\theta}{2} - \cos \frac{\theta_0}{2} \sin \frac{\theta}{2} \quad (4.11b)$$

and  $|11'\rangle$  and  $|20'\rangle$  are the basis vectors of the new basis, which we now refer to as the  $\theta$ -rotated basis. Correspondingly, we refer to the Bloch sphere with the  $\theta$ -rotated basis as the  $\theta$ -rotated Bloch sphere.

In the  $\theta$ -rotated basis, we denote the eigenvalues of the basis states as  $\pm\omega$ . In a static (non-rotating) frame, the Bloch vector will precess around the  $\theta$ -rotated basis axis, which results in a phase accumulation

$$|\psi\rangle = \bar{\alpha}e^{-i\phi/2} |11'\rangle + \bar{\beta}e^{i\phi/2} |20'\rangle = \alpha |11'\rangle + \beta |20'\rangle \quad (4.12)$$

where we denote

$$\alpha = \bar{\alpha}e^{-i\phi/2} = \cos \frac{\theta_0 - \theta}{2} e^{-i\phi/2} \quad (4.13)$$

and

$$\beta = \bar{\beta}e^{i\phi/2} = \sin \frac{\theta_0 - \theta}{2} e^{i\phi/2} \quad (4.14)$$

Here,  $\phi = \phi' + \int^t \omega(t')dt'$  is the accumulated phase up to time  $t$ , where  $\phi'$  is some initial reference phase, and  $\pm\omega(t)$  are the instantaneous eigenvalues as  $\theta(t)$  varies. Note that  $d\phi/dt = \omega$ .

The goal is to calculate the leakage error throughout the process where  $\theta(t)$  varies as a function of time. For a static process where  $\theta(t) = \theta$  is a constant, it suffices to calculate the probability  $P_e$  of measuring the state  $|\psi\rangle$  in  $|20'\rangle$  in the  $\theta$ -rotated basis

$$P_e = |\beta|^2 = \left| \sin \frac{\theta_0 - \theta}{2} \right|^2 \approx \left| \frac{\theta_0 - \theta}{4} \right|^2 \approx \left| \frac{\sin(\theta_0 - \theta)}{2} \right|^2 \quad (4.15)$$

where the third and fourth equations hold valid when  $\theta_0 - \theta$  is sufficiently small.

However, when  $\theta(t)$  varies as a function of time, we need to see how the component within  $|\cdot|$  in Eq. 4.15 evolves over time, and we seek for a formula that depends more directly on  $\theta(t)$ . Therefore, we first look at how  $\alpha$  and  $\beta$  evolve over time by taking a time derivative

$$\dot{\alpha} = -i\frac{\omega}{2}\alpha - \sin \frac{\theta_0 - \theta}{2} e^{-i\phi/2} \left(-\frac{1}{2}\dot{\theta}\right) = \frac{-i\omega\alpha + \beta\dot{\theta}}{2} \quad (4.16)$$

$$\dot{\beta} = i\frac{\omega}{2}\beta + \cos \frac{\theta_0 - \theta}{2} e^{i\phi/2} \left(-\frac{1}{2}\dot{\theta}\right) = \frac{i\omega\beta - \alpha\dot{\theta}}{2} \quad (4.17)$$

where we use the ‘‘dot’’ notation  $\dot{x}$  as a shorthand to denote the time derivative of  $x$ .

Note that

$$\begin{aligned}\alpha^*\beta &= \cos\frac{\theta_0 - \theta}{2}e^{i\phi/2} \sin\frac{\theta_0 - \theta}{2}e^{i\phi/2} \\ &= \frac{\sin(\theta_0 - \theta)}{2}e^{i\phi}\end{aligned}\tag{4.18}$$

which is directly related to the fourth equation in Eq. 4.15. It is interesting to see how  $\alpha^*\beta$  evolves over time. We proceed by taking the time derivative of  $\alpha^*\beta$

$$\frac{d}{dt}(\alpha^*\beta) = \dot{\alpha}^*\beta + \alpha^*\dot{\beta}\tag{4.19}$$

$$= \left[\frac{-i\omega\alpha + \beta\dot{\theta}}{2}\right]^*\beta + \alpha^*\frac{i\omega\beta - \alpha\dot{\theta}}{2}\tag{4.20}$$

$$= \frac{i\omega\alpha^* + \beta^*\dot{\theta}}{2}\beta + \alpha^*\frac{i\omega\beta - \alpha\dot{\theta}}{2}\tag{4.21}$$

$$= i\omega\alpha^*\beta + \frac{|\beta|^2 - |\alpha|^2}{2}\dot{\theta}\tag{4.22}$$

Since

$$\begin{aligned}(|\beta|^2 - |\alpha|^2)^2 &= |\beta|^4 + |\alpha|^4 - 2|\beta|^2|\alpha|^2 \\ &= |\beta|^4 + |\alpha|^4 + 2|\beta|^2|\alpha|^2 - 4|\alpha^*\beta|^2 \\ &= 1 - 4|\alpha^*\beta|^2\end{aligned}\tag{4.23}$$

we then have

$$|\beta|^2 - |\alpha|^2 = \pm\sqrt{1 - 4|\alpha^*\beta|^2}\tag{4.24}$$

Substituting Eq. 4.24 into Eq. 4.22, we have

$$\frac{d}{dt}(\alpha^*\beta) = i\omega\alpha^*\beta \pm \frac{\dot{\theta}}{2}\sqrt{1 - 4|\alpha^*\beta|^2}\tag{4.25}$$

If we substitute  $\alpha^*\beta = \sin(\theta_0 - \theta)e^{i\phi}/2$  as in Eq. 4.18, we will have

$$\frac{d}{dt}(\sin(\theta_0 - \theta)e^{i\phi}) = i\omega \sin(\theta_0 - \theta)e^{i\phi} \pm \dot{\theta} \cos(\theta_0 - \theta)\tag{4.26}$$

Substituting  $\phi = \phi' + \int^t \omega(t') dt'$  in Eq. 4.26, we have

$$\text{LHS} = \frac{d}{dt}(\sin(\theta_0 - \theta)e^{i\phi'})e^{\int^t \omega(t') dt'} + i\omega \sin(\theta_0 - \theta)e^{i\phi} \quad (4.27)$$

$$\text{RHS} = i\omega \sin(\theta_0 - \theta)e^{i\phi} \pm \dot{\theta} \cos(\theta_0 - \theta) \quad (4.28)$$

Therefore, we can derive

$$\frac{d}{dt}(\sin(\theta_0 - \theta)e^{i\phi'})e^{\int^t \omega(t') dt'} = \pm \dot{\theta} \cos(\theta_0 - \theta) \quad (4.29)$$

which can be rewritten as

$$d(\sin(\theta_0 - \theta)e^{i\phi'}) = \pm \dot{\theta} \cos(\theta_0 - \theta)e^{-\int^t \omega(t') dt'} dt \quad (4.30)$$

If we integrate both sides of Eq. 4.30, we will have

$$\sin(\theta_0 - \theta)e^{i\phi'} = \pm \int \cos(\theta_0 - \theta) \frac{d\theta}{dt} e^{-\int^t \omega(t') dt'} dt \quad (4.31)$$

Now we can write the leakage error  $P_e$  throughout the whole dynamic process as

$$P_e = \left| \frac{\sin(\theta_0 - \theta)}{2} \right|^2 = \frac{\left| \int \cos(\theta_0 - \theta) \frac{d\theta}{dt} e^{-\int^t \omega(t') dt'} dt \right|^2}{4} \quad (4.32)$$

Note that Eq. 4.31 and Eq. 4.8 differ by a factor of  $\cos(\theta_0 - \theta)$ . Here, the term  $\cos(\theta_0 - \theta)$  is due to the geometry of the  $\theta$ -rotated Bloch sphere relative to the original Bloch sphere whose basis vectors are  $|11\rangle$  and  $|20\rangle$ . When  $\theta_0 - \theta$  is sufficiently small, the approximation of Eq. 4.8 and Eq. 4.9 to Eq. 4.31 and Eq. 4.32 is valid, respectively.

As we will also discuss in Section 4.5, we make one further assumption that  $\omega(t)$  is approximated as a constant  $\omega(t) = \omega_0$  where  $\omega_0 = \Delta/\hbar$  is the eigenenergy difference precisely at the avoided crossing, as depicted in Figure 4-1. This approximation is not exact but makes intuitive sense if we assume most of the leakage error takes place around the avoided crossing. In Ref. [36], the authors develop a way to compensate for this approximation, a method which is not considered in this thesis. As the discussion

in Section 4.3.3 and simulation results in Chapter 6 indicate, this approximation provides great brevity while keeping its validity.

Finally, the formula for the leakage error  $P_e$  considered in this thesis is

$$P_e = \frac{\left| \int \frac{d\theta}{dt} e^{-i\omega_0 t} dt \right|^2}{4} \quad (4.33)$$

Note that the integral term within  $|\cdot|$  can be viewed as the Fourier transform of  $d\theta/dt$  evaluated at  $\omega_0$ .

### 4.3.3 Relationship to the Landau-Zener formula

Consider a two-level system described by the Hamiltonian in Eq. 4.1 and the energy diagram shown in Figure 4-1. Consider that the system is initially prepared in state  $|11\rangle$  with  $\varepsilon(t) \rightarrow -\infty$ . Then  $\varepsilon(t)$  increases in time and sweeps through the avoided crossing and eventually  $\varepsilon(t) \rightarrow +\infty$ . According to the Landau-Zener probability of transition given in Ref. [45], we can derive the probability that the system will undergo a transition to  $|20\rangle$  for the simple case where  $\varepsilon(t) = \alpha t$  with  $\alpha$  being a positive constant

$$P_{LZ} = e^{-\pi\Delta^2/2\alpha} \quad (4.34)$$

In Eq. 4.33, we do not assume that  $\varepsilon(t) = \alpha t$  increases linearly with time. However, if we were to make this assumption, we could compute the transition probability  $P_{eLZ}$  from Eq. 4.33 and compare it to  $P_{LZ}$  in Eq. 4.34.

First we compute the time derivative of  $\theta(t)$

$$\begin{aligned} \frac{d\theta}{dt} &= \frac{1}{1 + (\Delta/\alpha t)^2} \times \frac{-\Delta}{\alpha t^2} \\ &= \frac{-\Delta}{\alpha t^2 + \Delta^2/\alpha} \\ &= \frac{-\Delta/\alpha}{t^2 + (\Delta/\alpha)^2} \end{aligned} \quad (4.35)$$

Then we compute the integral within  $|\cdot|$  in Eq. 4.33 and substitute  $\omega_0 = \Delta/\hbar$  (let

$\hbar = 1$ )

$$\begin{aligned}
\int \frac{d\theta}{dt} e^{-i\omega_0 t} dt &= \int \frac{-\Delta/\alpha}{t^2 + (\Delta/\alpha)^2} e^{-i\omega_0 t} dt \\
&= -\pi e^{-\Delta\omega_0/\alpha} \\
&= -\pi e^{-\Delta^2/\alpha}
\end{aligned} \tag{4.36}$$

Therefore, we have

$$P_{\text{eLZ}} = \frac{\pi^2}{4} e^{-2\Delta^2/\alpha} \tag{4.37}$$

The relationship between  $P_{\text{LZ}}$  in Eq. 4.34 and  $P_{\text{eLZ}}$  in Eq. 4.37 can be written as

$$\log P_{\text{LZ}} = \frac{\pi}{4} (\log P_{\text{eLZ}} - C) \tag{4.38}$$

where  $C = \log \frac{\pi^2}{4}$  is some constant.

The outcomes differ for the two approaches because the formula for the transition probability in Eq. 4.33 is derived under certain (different) assumptions. However, it can be seen that  $P_{\text{eLZ}}$  is a good indicator of  $P_{\text{LZ}}$  if the exact value of the transition probability is not desired. More specifically, we show that  $\log P_{\text{LZ}}$  is a linear function of  $\log P_{\text{eLZ}}$  with a positive slope  $\pi/4$  in Eq. 4.38. Because a logarithmic function  $\log(\cdot)$  is always a monotonic function, minimizing  $P_{\text{eLZ}}$  is equivalent to minimizing  $P_{\text{LZ}}$ . In this thesis, what we really care about is the comparison between different control trajectories in the problem of control trajectory design in CZ gates. Therefore, we argue that the formula for the leakage error  $P_e$  in Eq. 4.33 is sufficient for our purpose.

## 4.4 Two scenarios

In Section 4.4, we discuss the two scenarios considered in this thesis, which we refer to as the Type-I process (Section 4.4.1) and the Type-II process (Section 4.4.2). The main difference between the two scenarios is whether we move through the avoided crossing region, or return from the avoided crossing region. We note that when we say the avoided crossing region, we mean anywhere near the avoided crossing, but

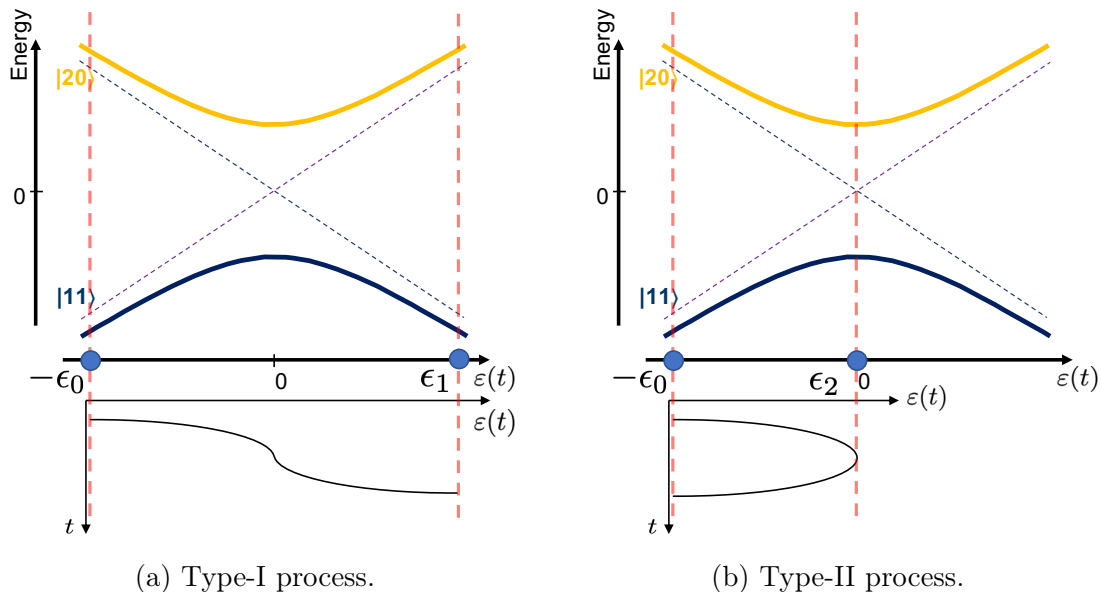


Figure 4-3: Type-I process v.s. Type-II process. (a) In the Type-I process,  $\varepsilon(t)$  varies from  $-\epsilon_0$  to  $+\epsilon_1$  where  $\epsilon_0 > 0$  and  $\epsilon_1 > 0$ . A typical trajectory for  $\varepsilon(t)$  is depicted. (b) In the Type-II process,  $\varepsilon(t)$  varies from  $-\epsilon_0$  to  $\epsilon_2$  and return to  $-\epsilon_0$  where  $\epsilon_0 > 0$  and  $\epsilon_2 \approx 0$ . A typical trajectory for  $\varepsilon(t)$  is depicted.

not necessarily exactly the the avoided crossing point.

#### 4.4.1 Type-I process: Move through the avoided crossing

The Type-I process is referred to as the type of evolution where we move through the avoided crossing, as depicted in Figure 4-3a. Recall that in Section 4.1 the Hamiltonian describing the two-level system is given in Eq. 4.1. In the Type-I process,  $\varepsilon(t)$  varies from  $-\epsilon_0$  to  $+\epsilon_1$  where  $\epsilon_0 > 0$  and  $\epsilon_1 > 0$ . In terms of  $\theta(t) = \arctan(\Delta/\varepsilon(t))$ ,  $\theta(t)$  varies from  $\theta_0 = -\arctan(\Delta/\epsilon_0)$  to  $\theta_1 = \arctan(\Delta/\epsilon_1)$  where  $\pi/2 < \theta_0 < \pi$  and  $0 < \theta_1 < \pi/2$ . In the following discussions, we ask that  $\epsilon_0 = \epsilon_1$ , i.e.,  $\theta_0 + \theta_1 = \pi$  for simplicity.

Usually the CPHASE gate is not an example of this process due to the effects of other energy levels in the system and operation convenience, but we keep the discussion for completeness of this thesis.

### 4.4.2 Type-II process: Return from the avoided crossing

The Type-II process refers to the scenario where we move into the avoided crossing region and then return to the initial point, as depicted in Figure 4-3b. The CPHASE gate implementation considered in this thesis falls under the category of the Type-II process. In the Type-II process,  $\varepsilon(t)$  varies from  $-\epsilon_0$  to  $\epsilon_2$  and returns to  $-\epsilon_0$  where  $\epsilon_0 > 0$  and  $\epsilon_2 \approx 0$ . In terms of  $\theta(t) = \arctan(\Delta/\varepsilon(t))$ ,  $\theta(t)$  varies from  $\theta_0 = -\arctan(\Delta/\epsilon_0)$  to  $\theta_2 = \arctan(\Delta/\epsilon_2)$  and returns to  $\theta_0$  where  $\pi/2 < \theta_0 < \pi$  and  $\theta_2 \approx \pi/2$ .

## 4.5 Problem formulation

In Section 4.5, we propose an optimization formulation with an explicit optimality criterion. We start by describing the straightforward idea that the shortest pulse is desired given a specified constraint on the allowable leakage error in Section 4.5.2. Then, taking advantage of the time and frequency scaling property, we transform the problem into an optimization performed over frequency in Section 4.5.3. Finally, in Section 4.5.4, we comment on the continuous time to discrete time transformation.

### 4.5.1 Nomenclature

In the previous chapters, we have ambiguously used “pulse design” or “control trajectory design” to refer to the problem considered in this thesis. Prior to the problem formulation, we shall first address issues of nomenclature. In this thesis, the ultimate goal is to design a baseband flux pulse that changes the external flux that threads the SQUID loop of QB1 so that a CPHASE gate with desired characteristics is obtained. Since the baseband flux pulse is directly related to the energy of the diabatic state corresponding to state  $|11\rangle$ , it suffices to design a pulse to describe how the energy of the diabatic state varies. In the abstracted two-level system discussed in Section 4.1, the goal is further transformed into designing a way to describe how  $\varepsilon(t)$  varies. Then, an intermediate control variable  $\theta(t) = \arctan(\Delta/\varepsilon(t))$  is defined,

which has a one-to-one correspondence to  $\varepsilon(t)$  by definition. Therefore, the goal of designing an optimal  $\varepsilon(t)$  is in practice indistinguishable with designing an optimal  $\theta(t)$ . Finally, in Eq. 4.33, the formula for the leakage error (as defined in this thesis) is written in terms of the Fourier transform of  $d\theta/dt$ . The goal of designing an optimal flux pulse further transforms into finding an optimal trajectory  $d\theta/dt$ , which we refer to as “control trajectory design.” In Section 4.5, we denote  $g(t) = d\theta/dt$  for brevity. A discrete form of  $g(t)$  is  $g[n]$ , a correspondence which we will elaborate on in Section 4.5.4.

## 4.5.2 Intuitive formulation: optimization over duration

In Section 4.3, we concluded with a formula for the leakage error  $P_e$  in Eq. 4.33. We can rewrite the formula in terms of the Fourier transform of  $g(t) = d\theta/dt$

$$\begin{aligned}
 P_e &= \frac{\left| \int g(t) e^{-i\omega_0 t} dt \right|^2}{4} \\
 &= \frac{|G(i\omega_0)|^2}{4}
 \end{aligned}
 \tag{4.39}$$

where  $G(i\omega_0)$  is the Fourier transform of  $g(t)$  evaluated at  $\omega_0$ .

In the implementation of a high-fidelity CPHASE gate, we especially care about three factors: phase accumulation, leakage error, and gate duration. Phase accumulation is directly related to  $\theta(t)$  as discussed in Section 4.2. We assume that we can approximately obtain a desired phase accumulation with the same amplitude for different shapes of  $\theta(t)$ . In Chapter 6, we will show that we can impose a desired phase accumulation by tuning the amplitude. It turns out that the simulation results are slightly distorted, but the advantage of the optimal control trajectory derived from our analysis achieving shorter gate duration still holds. Now we focus on the two remaining convoluted factors: leakage error and gate duration. We are interested in designing a  $g(t)$  with as short a duration as possible, given some acceptable leakage error threshold. Here the parameters to be optimized are the shape and duration of  $g(t)$ . In addition, in cases where  $g(t)$  has the same shape but a longer duration, we

desire that the leakage error remain below the error threshold. This makes intuitive sense, because a longer  $g(t)$  generally corresponds to a slower evolution and therefore should induce no more (and often less) leakage error. Furthermore, in experiments, pulses can be longer than expected due to nonidealities in hardware, and we would like to include this situation in our consideration.

In this formulation, we consider two scenarios, the Type-I process and the Type-II process, as discussed in Section 4.4. Let  $t_d$  be the duration of  $g(t)$ . The Type-I process is where  $\theta(t)$  evolves from some initial value  $\theta_0$  to some final value  $\theta_1$ , i.e.,  $\int_0^{t_d} g(t)dt = \int_{t_d/2}^{t_d} g(t)dt = (\theta_1 - \theta_0)/2$ . For convenience of design, we further normalize the control trajectory so that  $\int_0^{t_d/2} g(t)dt = \int_{t_d/2}^{t_d} g(t)dt = 1$ . Here, we implicitly assume that  $\theta(t) = \pi/2$  (exactly at the avoided crossing) at exactly half of the duration. The Type-II process is where  $\theta(t)$  starts from some initial value  $\theta_0$  to some intermediate value  $\theta_2$  and then returns to the initial value  $\theta_0$ . We implicitly assume that  $\theta(t)$  equals the intermediate value  $\theta_2$  at exactly half of the duration, i.e.,  $\int_0^{t_d/2} g(t)dt = \theta_2 - \theta_0$  and  $\int_{t_d/2}^{t_d} g(t)dt = \theta_0 - \theta_2$ . The validity of this restriction will become clear when the optimal solution is presented in Section 5.2. We further normalize the control trajectory so that  $\int_0^{t_d/2} g(t)dt = -\int_{t_d/2}^{t_d} g(t)dt = 1$ .

Now  $g(t)$  is time limited to the interval  $[0, t_d]$ , i.e.,  $g(t) = 0$ , when  $t < 0$  or  $t > t_d$ . Consider the leakage error in Eq. 4.33 and pay specific attention to  $|G(i\omega_0)|$ , which is the magnitude of the Fourier transform of  $g(t)$  of duration  $t_d$ . The optimization problem can be stated as follows. Given an error threshold  $P_e \leq \gamma^2/4$ , i.e.,  $|G(i\omega_0)| \leq \gamma$ , the goal is to find the  $g(t)$  of duration  $t_d^*$  with  $t_d^* = \min(t_{dc})$ , where for any  $t_d \geq t_{dc}$ ,  $|G(i\omega_0)| \leq \gamma$  is satisfied. At first glance, this problem is not easily solvable, because the minimization is also interdependent on the trajectory duration in a manner. In order to compute  $|G(i\omega_0)|$ , it is always required to determine  $t_d$  first, but the minimization is also over  $t_d$ . An intuitive program would be to create and compare trial cases with different  $t_d$ 's, which is computationally expensive and may not converge to the optimal solution.

### 4.5.3 Time-frequency transformation: optimization over frequency

We first introduce a dummy alphabet  $\mathcal{A}$  with infinite elements corresponding to an infinite number of control trajectory shapes and use  $g^a(t)$  where  $a \in \mathcal{A}$  to denote a control trajectory normalized in time to the interval  $[0, 1]$ , i.e.,  $g^a(t) = 0$ , when  $t < 0$  or  $t > 1$ . We further impose normalization so that for the Type-I process, we have  $\int_0^{1/2} g^a(t)dt = \int_{1/2}^1 g^a(t)dt = 1$ , and for the Type-II process, we have  $\int_0^{1/2} g^a(t)dt = -\int_{1/2}^1 g^a(t)dt = 1$ . We refer to  $g^a(t)$  as a control trajectory shape labelled by  $a$ .

For any  $g(t)$  of duration  $t_d$ , there must exist some  $a \in \mathcal{A}$  such that  $g(t) = g^a(t/t_d)/t_d$ . With the time and frequency scaling property of the Fourier transform, we have  $G(i\omega_0) = G^a(i\omega_0 t_d)$ , where  $G^a(i\omega_0 t_d)$  is the Fourier transform of  $g^a(t)$  evaluated at  $\omega_0 t_d$ . The original statement in Section 4.5.2 then is transformed into finding a control trajectory shape  $g^a(t)$  such that  $t_d^*$  is minimized, i.e.,  $t_d^* = \min(t_{dc})$ , where for any  $t_d \geq t_{dc}$ ,  $|G(i\omega_0 t_d)| \leq \gamma$  is satisfied.

Note that in the expression  $G^a(i\omega_0 t_d)$ ,  $\omega_0$  and  $t_d$  are nominally on an equivalent footing. Therefore, it would be equivalent to construct the problem with  $t_d$  given and  $\omega_0$  varied and to be minimized, instead of fixing  $\omega_0$  and minimizing over  $t_d$ . For convenience, we set  $t_d = 1$  and use  $\omega$  instead of  $\omega_0$ . In this way, we reformulate the problem into finding a trajectory shape  $g^a(t)$  such that  $\omega^*$  is minimized, where  $\omega^*$  is defined as the minimum frequency such that for any  $\omega \geq \omega^*$ ,  $|G^a(i\omega)| \leq \gamma$  is satisfied.

Based on the notation and optimality criterion derived above, we state the problem formulation more explicitly as follows:

1. Type-I process:

A control trajectory  $g(t)$  is desired, where  $g(t)$  is normalized:

- (a)  $g(t) = 0$  when  $t < 0$  or  $t > 1$ ,
- (b)  $\int_0^{t_d/2} g(t)dt = \int_{t_d/2}^{t_d} g(t)dt = 1$ ,

such that  $\omega^*$  is minimized, where  $\omega^*$  is defined as  $\omega^* = \min(\omega_c)$  such that

$$\text{for any } \omega \geq \omega_c, |G(i\omega)| \leq \gamma,$$

where  $G(i\omega)$  is the Fourier transform of  $g(t)$  and  $\gamma$  is given.

2. Type-II process:

A control trajectory  $g(t)$  is desired, where  $g(t)$  is normalized:

- (a)  $g(t) = 0$  when  $t < 0$  or  $t > 1$ ,
- (b)  $\int_0^{1/2} g(t)dt = -\int_{1/2}^1 g(t)dt = 1$ ,

such that  $\omega^*$  is minimized, where  $\omega^*$  is defined as  $\omega^* = \min(\omega_c)$  such that

$$\text{for any } \omega \geq \omega_c, |G(i\omega)| \leq \gamma,$$

where  $G(i\omega)$  is the Fourier transform of  $g(t)$  and  $\gamma$  is given.

#### 4.5.4 Continuous time to discrete time transformation

The formulation so far has been stated in continuous time. However, in experiments, a discrete-time pulse needs to be specified for the digital controller of the pulse generation hardware (arbitrary waveform generator), followed by a certain interpolation scheme in order to output a continuous-time pulse when the baseband flux pulse is implemented. Therefore, in this thesis, we consider specifically the design in discrete time. Let  $T_s$  be the sampling frequency. Then we have  $g[n] = g(nT_s)$  for  $n = 0, 1, \dots, N - 1$  where  $N - 1 = 1/T_s$ . We refer to  $N$  as the length of  $g[n]$ . We determine the problem formulation in discrete time as follows:

1. Type-I process:

A control trajectory  $g[n]$  of length  $N$  is desired, where  $g[n]$  is normalized:

- (a)  $g[n] = 0$  when  $n < 0$  or  $n > N - 1$ ,

- (b)  $\sum_0^{N/2-1} g[n] = 1 = \sum_{N/2}^{N-1} g[n]$  for even  $N$ , or  $\sum_0^{(N-1)/2} g[n] = 1 = \sum_{(N-1)/2}^{N-1} g[n]$  for odd  $N$ ,

such that  $\omega^*$  is minimized, where  $\omega^*$  is defined as  $\omega^* = \min(\omega_c)$  such that

$$\text{for any } \omega \geq \omega_c, |G(e^{i\omega})| \leq \gamma,$$

where  $G(e^{i\omega})$  is the discrete time Fourier transform of  $g[n]$  and  $\gamma$  is given.

## 2. Type-II process:

A control trajectory  $g[n]$  of length  $N$  is desired, where  $g[n]$  is normalized:

- (a)  $g[n] = 0$  when  $n < 0$  or  $n > N - 1$ ,
- (b)  $\sum_0^{N/2-1} g[n] = 1 = -\sum_{N/2}^{N-1} g[n]$  for even  $N$ , or  $\sum_0^{(N-1)/2} g[n] = 1 = -\sum_{(N-1)/2}^{N-1} g[n]$  for odd  $N$ ,

such that  $\omega^*$  is minimized, where  $\omega^*$  is defined as  $\omega^* = \min(\omega_c)$  such that

$$\text{for any } \omega \geq \omega_c, |G(e^{j\omega})| \leq \gamma,$$

where  $G(e^{i\omega})$  is the discrete time Fourier transform of  $g[n]$  and  $\gamma$  is given.

# Chapter 5

## Optimal Solutions and Comparisons

In Section 4.5, we reformulated the CPHASE gate design problem into a pulse design problem and further transformed it into the design of a control trajectory  $g[n]$ . In Chapter 5, we propose multiple candidates for the control trajectory of the pulse design problem considered in this thesis based on finite-length discrete-time pulses discussed in Chapter 2. We study the two scenarios illustrated in Section 4.4 and compare different potential solutions in Section 5.2. Special attention is paid to the comparisons between the optimal solutions derived in this thesis, i.e., the Chebyshev trajectories I and II, and the first and second Slepian trajectories widely used in current quantum experiments.

### 5.1 Control trajectories based on some common finite-length discrete-time pulses

The control trajectory  $g[n]$  needs to satisfy the normalization constraints as discussed in Section 4.5. Specifically, for the Type-I process, the constraints are

$$g[n] = 0 \text{ when } n < 0 \text{ or } n > N - 1 \tag{5.1a}$$

$$\sum_0^{N/2-1} g[n] = 1 = \sum_{N/2}^{N-1} g[n] \text{ for even } N, \text{ or } \sum_0^{(N-1)/2} g[n] = 1 = \sum_{(N-1)/2}^{N-1} g[n] \text{ for odd } N \quad (5.1b)$$

and for the Type-II process the constraints are

$$g[n] = 0 \text{ when } n < 0 \text{ or } n > N - 1 \quad (5.2a)$$

$$\sum_0^{N/2-1} g[n] = 1 = -\sum_{N/2}^{N-1} g[n] \text{ for even } N, \text{ or } \sum_0^{(N-1)/2} g[n] = 1 = -\sum_{(N-1)/2}^{N-1} g[n] \text{ for odd } N \quad (5.2b)$$

The Type-I process and the Type-II process correspond to the symmetric and anti-symmetric control trajectories, respectively. The finite length constraint in Eqs. 5.1a and 5.2a are naturally satisfied by the finite-length discrete-time pulses. Therefore, the control trajectories can be derived through a straightforward normalization of the finite-length discrete-time pulses as discussed in Chapter 2. For the Type-I process, we define the control trajectories  $g_{\text{sym}}[n]$  by scaling and normalizing the corresponding symmetric pulses  $w_{\text{sym}}[n]$  such that  $\sum_0^{N/2-1} g_{\text{sym}}[n] = 1 = \sum_{N/2}^{N-1} g_{\text{sym}}[n]$  for even  $N$ , or  $\sum_0^{(N-1)/2} g_{\text{sym}}[n] = 1 = \sum_{(N-1)/2}^{N-1} g_{\text{sym}}[n]$  for odd  $N$ , where ‘‘sym’’ is an index denoting which symmetric finite-length discrete-time pulse is considered. Similarly, for the Type-II process, we define the control trajectories by scaling and normalizing the corresponding anti-symmetric pulses  $w_{\text{asym}}[n]$  such that  $\sum_0^{N/2-1} g_{\text{asym}}[n] = 1 = -\sum_{N/2}^{N-1} g_{\text{asym}}[n]$  for even  $N$ , or  $\sum_0^{(N-1)/2} g_{\text{asym}}[n] = 1 = -\sum_{(N-1)/2}^{N-1} g_{\text{asym}}[n]$  for odd  $N$ , where ‘‘asym’’ is an index denoting which anti-symmetric finite-length discrete-time pulse is considered. In this thesis, we have  $\text{sym} \in \{\text{rec}, \text{hann}, \text{hamm}, \text{bkm}, \text{cos}, \text{sl1}, \text{ka}, \text{ch1}\}$  and  $\text{asym} \in \{\text{sl2}, \text{ch2}\}$ . The abbreviations are associated with the finite-length discrete-time pulses discussed in Chapter 2.

## 5.2 Two scenarios

In Section 4.4, we discussed the characteristics of the Type-I and Type-II processes. In Section 5.2, we propose the Chebyshev I and II trajectories as an alternative solution

for the Type-I and Type-II processes. We will in particular compare the Chebyshev I and II trajectories with the first and second Slepian trajectories, respectively. We show that under the optimality criterion formulated in this thesis the Chebyshev trajectories can outperform their Slepian counterparts.

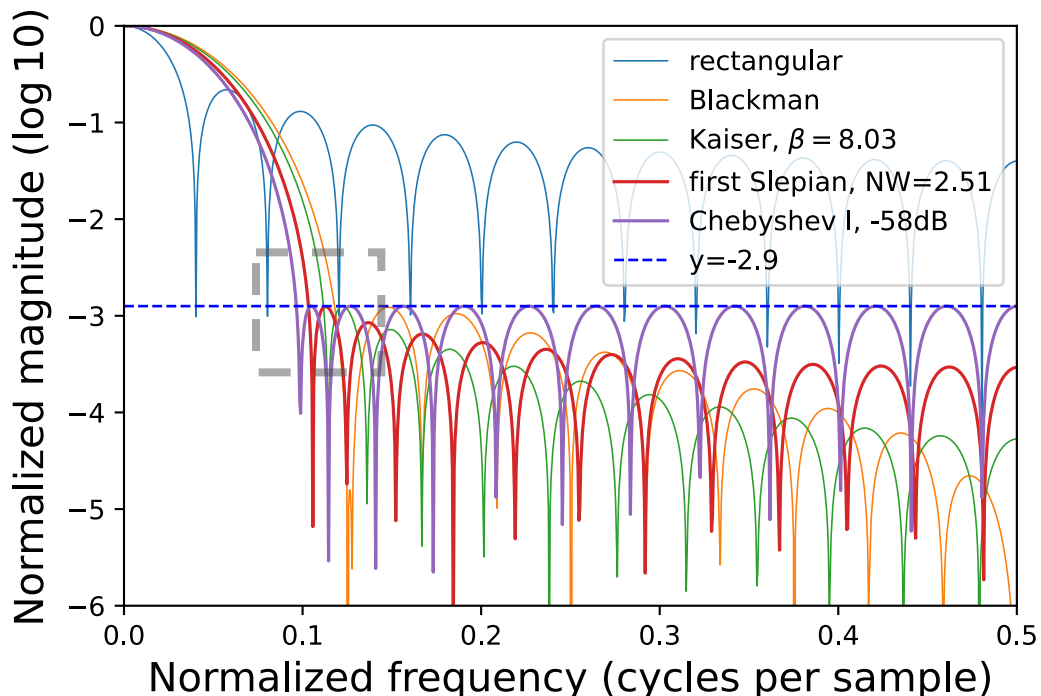


Figure 5-1: Frequency-domain representations of the rectangular trajectory, the Blackman trajectory, the Kaiser trajectory, the first Slepian trajectory and the Chebyshev trajectory I for  $N = 25$ . Their first sidelobe amplitudes match one another and are equal to the given threshold  $\gamma = 10^{-2.9} \approx 0.0013$  (except for the rectangular trajectory). The dashed gray box area is where we compare the different trajectories. See a zoom-in plot in Figure 5-2.

### 5.2.1 Type-I process: Move through the avoided crossing

Recall that in Section 4.5.4 the optimality criterion for the Type-I process is stated as follows:

**Optimality criterion:**

A control trajectory  $g[n]$  of length  $N$  is desired, where  $g[n]$  is normalized:

- (a)  $g[n] = 0$  when  $n < 0$  or  $n > N - 1$ ,

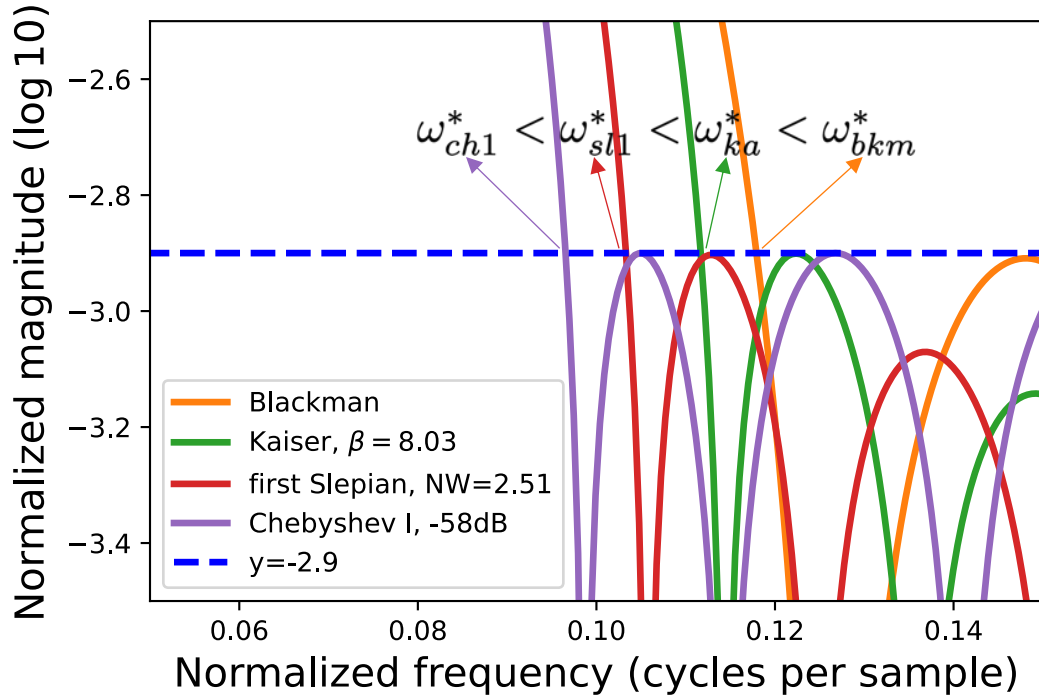


Figure 5-2: A zoom-in plot of the dashed gray box area in Figure 5-1. We find that  $\omega_{ch1}^* < \omega_{sl1}^* < \omega_{ka}^* < \omega_{bkm}^*$ .

(b)  $\sum_0^{N/2-1} g[n] = 1 = \sum_{N/2}^{N-1} g[n]$  for even  $N$ , or  $\sum_0^{(N-1)/2} g[n] = 1 = \sum_{(N-1)/2}^{N-1} g[n]$  for odd  $N$ ,

such that  $\omega^*$  is minimized, where  $\omega^*$  is defined as  $\omega^* = \min(\omega_c)$  such that

$$\text{for any } \omega \geq \omega_c, |G(e^{i\omega})| \leq \gamma,$$

where  $G(e^{i\omega})$  is the discrete time Fourier transform of  $g[n]$  and  $\gamma$  is given.

This formulation bears a close similarity to the problem formulated in Refs. [21, 46], i.e., minimizing the mainlobe width subject to a sidelobe amplitude specification, whose optimal solution has been shown in the literature to be the Chebyshev pulse I as we discussed in Section 2.2.5. Therefore, we propose the Chebyshev trajectory I  $g_{ch1}[n]$  to be a candidate solution in this problem. Figure 5-1 shows a comparison of the magnitude of Fourier transform of different control trajectories  $g_{rec}[n]$ ,  $g_{bkm}[n]$ ,  $g_{ka}[n]$ ,  $g_{ch1}[n]$  and  $g_{sl1}[n]$ , all of which are of length  $N = 25$ . We specifically choose

the parameters for each trajectory so that their first sidelobe amplitudes match one another (except for the rectangular trajectory) and are equal to the given threshold  $\gamma = 10^{-58/20} \approx 0.0013$ . The reason for choosing such a  $\gamma$  is that we would like to include the Blackman trajectory in comparison. Therefore, we match the first sidelobe amplitudes of the other trajectories (except for the rectangular trajectory) to the first sidelobe amplitude of the Blackman trajectory, which is solely determined by the length  $N = 25$ . To achieve this, we choose  $\beta = 8.03$  for the Kaiser trajectory and  $NW = 2.51$  for the first Slepian trajectory, and specify the sidelobe amplitudes of the Chebyshev trajectory I to be equal to  $\gamma$ . In principal, however,  $\gamma$  can be arbitrarily specified. If we pay special attention to the dashed gray box area in Figure 5-1, zoomed in as shown in Figure 5-2, we will find that  $\omega_{\text{ch1}}^* < \omega_{\text{sl1}}^* < \omega_{\text{ka}}^* < \omega_{\text{bkkm}}^*$ . With the optimality criterion defined in this thesis, the Chebyshev trajectory I  $g_{\text{ch1}}[n]$  is always the better option than control trajectories based on other finite-length discrete-time pulses. This option is better because, for any arbitrarily given threshold  $\gamma$ , the Chebyshev trajectory I  $g_{\text{ch1}}[n]$  always holds the smallest  $\omega^*$ .

### 5.2.2 Type-II process: Return from the avoided crossing

The optimality criterion for the Type-II process as stated in Section 4.5.4 is shown below.

**Optimality criterion:**

A control trajectory  $g[n]$  of length  $N$  is desired, where  $g[n]$  is normalized:

- (a)  $g[n] = 0$  when  $n < 0$  or  $n > N - 1$ ,
- (b)  $\sum_0^{N/2-1} g[n] = 1 = -\sum_{N/2}^{N-1} g[n]$  for even  $N$ , or  $\sum_0^{(N-1)/2} g[n] = 1 = -\sum_{(N-1)/2}^{N-1} g[n]$  for odd  $N$ ,

such that  $\omega^*$  is minimized, where  $\omega^*$  is defined as  $\omega^* = \min(\omega_c)$  such that

$$\text{for any } \omega \geq \omega_c, |G(e^{j\omega})| \leq \gamma,$$

where  $G(e^{j\omega})$  is the discrete time Fourier transform of  $g[n]$  and  $\gamma$  is given.

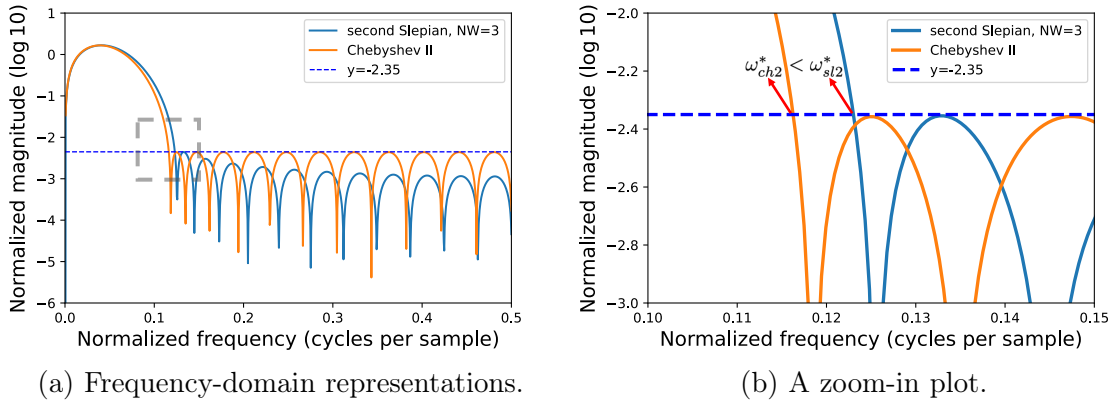


Figure 5-3: (a) The frequency-domain representations of the second Slepian trajectory and the Chebyshev trajectory II for  $N = 25$ , where their first sidelobe amplitudes match each other and are equal to the given threshold  $\gamma = 10^{-2.35} \approx 0.0045$ . (b) A zoom-in plot of the dashed gray box area in (a). We find that  $\omega_{ch2}^* < \omega_{sl2}^*$ .

The optimality criterion statement for the Type-II process differs from that for the Type-I process in that the normalization requirement implicitly leads to an anti-symmetric control trajectory  $g[n]$ . Inspired by the optimal solution proposed for the Type-I process, we propose the Chebyshev trajectory II  $g_{ch2}[n]$  to be utilized for the Type-II process, which potentially has an advantage over the second Slepian trajectory  $g_{sl2}[n]$ . The argument is similar in that as we allow higher sidelobe amplitude in larger frequency components, we can in turn decrease the mainlobe width. The major characteristics of the two control trajectories are that the Chebyshev trajectory II  $g_{ch2}[n]$  has equal sidelobe amplitude for all sidelobes, while the second Slepian trajectory  $g_{sl2}[n]$  has decreasing sidelobe amplitude. Therefore, we propose two methods for choosing the sidelobe amplitude of the Chebyshev trajectory II according to the second Slepian trajectory, or vice versa. We will show an example for each method in Figure 5-3 and 5-4.

First, we arbitrarily determine an second Slepian trajectory of length  $N = 25$  and  $NW = 3$  to be compared against. As depicted in Figure 5-3, we show a comparison of the frequency-domain representations of the Chebyshev trajectory II  $g_{ch2}[n]$  and the second Slepian trajectory  $g_{sl2}[n]$ . We specifically choose  $g_{ch2}[n]$  so that its sidelobe amplitude matches the first sidelobe amplitude of the specified second Slepian

trajectory  $g_{sl2}[n]$ , and both are equal to the given threshold  $\gamma = 10^{-2.35} \approx 0.0045$ . Pay attention to the dashed gray box area in Figure 5-3a, zoomed in as shown in Figure 5-3b, and we find that  $\omega_{ch2}^* < \omega_{sl2}^*$ . While satisfying the restriction on side-lobe amplitude, the Chebyshev trajectory II  $g_{ch2}[n]$  outperforms the second Slepian trajectory  $g_{sl2}[n]$  for incurring a smaller  $\omega^*$ .

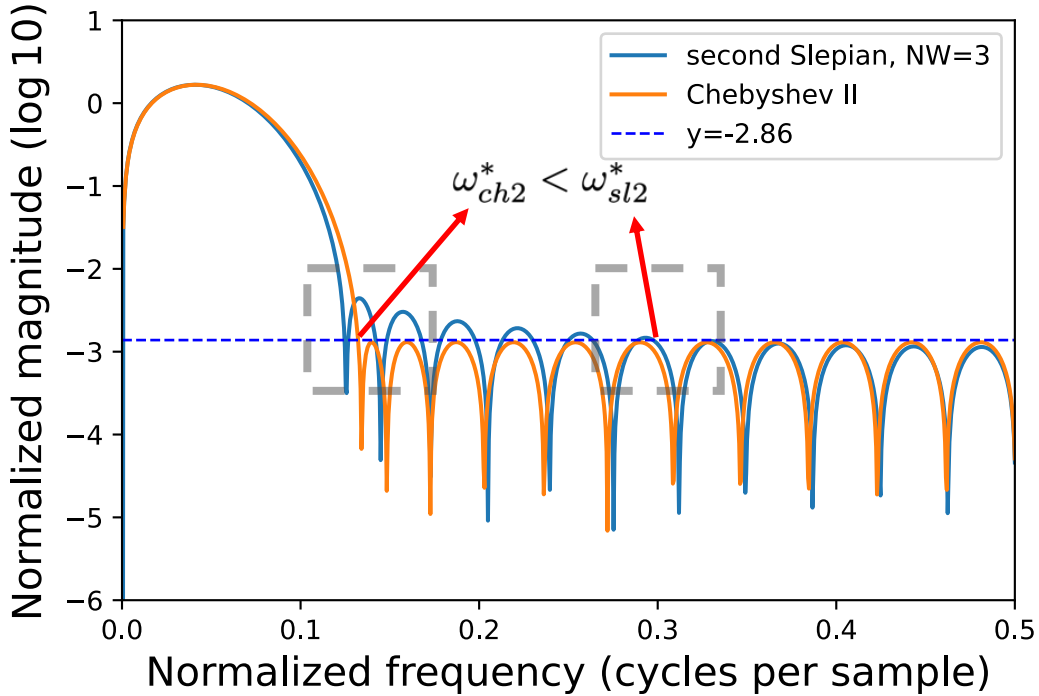


Figure 5-4: The frequency-domain representations of the second Slepian trajectory and the Chebyshev trajectory II for  $N = 25$ , where their sidelobe amplitudes match each other at the 7th sidelobe. The threshold is set to be  $\gamma = 10^{-2.86} \approx 0.0014$ . We find that  $\omega_{ch2}^* < \omega_{sl2}^*$ .

Figure 5-4 shows a further comparison where we specifically choose  $g_{ch2}[n]$  so that its sidelobe amplitude matches the 7th sidelobe of the specified second Slepian trajectory  $g_{sl2}[n]$  to allow for a lower threshold  $\gamma = 10^{-2.86} \approx 0.0014$ . As depicted in the dashed gray box areas in Figure 5-4, we find that  $\omega_{ch2}^* < \omega_{sl2}^*$  by a notable amount in this example ( $\omega_{ch2}^* \approx 0.14$  and  $\omega_{sl2}^* \approx 0.31$ ), while all the further sidelobes beyond  $\omega^*$  remain equal to or below the threshold  $\gamma$ .

## 5.3 Summary and discussion

In the theoretical analysis of the abstracted two-level system, we draw the following conclusions:

1. With the optimality criterion defined in this thesis, the Chebyshev trajectories outperform the Slepian trajectories for both the Type-I and Type-II processes. Specifically, this statement indicates that in order to achieve the same level of leakage error, the Chebyshev trajectories can be designed to be shorter in time than the Slepian trajectories.
2. The Chebyshev trajectories can be designed to satisfy different leakage error thresholds while maintaining its advantage of a shorter duration over the Slepian trajectories.

# Chapter 6

## Time-domain Simulation Using QuTiP

In Chapter 6, we show time-domain simulation results using QuTiP. Since, in this thesis, we are mostly interested in the process of a CZ gate between two coupled transmon qubits, we will only show simulation results regarding the Type II process. We concentrate on the comparison between the second Slepian trajectory and the Chebyshev trajectory II as proposed in Section 5.2.2.

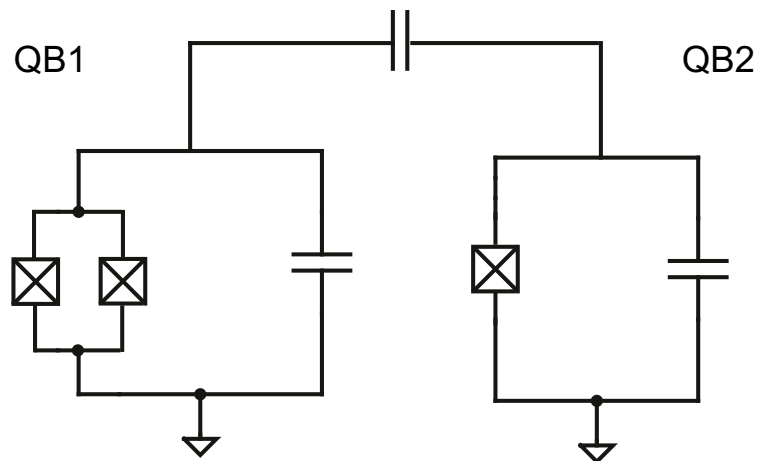


Figure 6-1: Circuit diagram of a flux-tunable transmon capacitively coupled to a fixed-frequency transmon. The flux-tunable transmon is referred to as QB1 and the fixed-frequency transmon is referred to as QB2. Same figure as Figure 3-6.

## 6.1 Setting and procedure

Consider two capacitively coupled transmon qubits, one of which is flux-tunable (QB1) and the other has fixed frequency (QB2). The circuit diagram is shown in Figure 6-1. The Hamiltonian of each of the transmon qubits can be written as (let  $\hbar = 1$ )

$$H_i = \omega_i a_i^\dagger a_i + \frac{\alpha_i}{2} a_i^\dagger a_i^\dagger a_i a_i, \quad i = 1, 2 \quad (6.1)$$

where  $a_i^\dagger$ ,  $a_i$  are the raising (creation) and lowering (annihilation) operators in the eigenbasis of the corresponding qubit,  $\omega_i$  is the qubit frequency of QB*i*, and  $\alpha_i$  is the anharmonicity of QB*i*. Note that  $\omega_1$  can be varied since QB1 is a flux-tunable transmon qubit.

The Hamiltonian of the coupling term can be written as

$$H_{12} = g(a_1^\dagger + a_1) \otimes (a_2^\dagger + a_2) \quad (6.2)$$

where  $g$  is the coupling strength and  $\otimes$  denotes tensor product.

Therefore, the whole system Hamiltonian can be written as a sum of the individual Hamiltonians mentioned above

$$\begin{aligned} H &= \sum_{i=1,2} H_i + H_{12} \\ &= \sum_{i=1,2} \left( \omega_i a_i^\dagger a_i + \frac{\alpha_i}{2} a_i^\dagger a_i^\dagger a_i a_i \right) + g(a_1^\dagger + a_1) \otimes (a_2^\dagger + a_2) \end{aligned} \quad (6.3)$$

In our simulation, we choose the parameters  $\omega_1 = 5.2$  GHz,  $\omega_2 = 4.7$  GHz,  $\alpha_1 = \alpha_2 = -0.3$  GHz, and  $g = 50$  MHz, which form a typical parameter set for transmon qubits. In order to perform a CPHASE gate, we would like to detune  $\omega_1$  so that  $\omega_1 + \omega_2 \approx 2\omega_1 + \alpha_1$ . If we move exactly into the avoided crossing between state  $|11\rangle$  and  $|20\rangle$ , then  $\omega_1 + \omega_2 = 2\omega_1 + \alpha_1$ , i.e.,  $\omega_1 = 5.0$  GHz. An energy spectrum diagram of the system to be simulated is shown in Figure 6-2. We will vary  $\omega_1$  from  $\omega_1 = 5.2$  GHz to approximately  $\omega_1 = 5.0$  GHz depending on the amplitude of the control pulse, and then back to  $\omega_1 = 5.2$  GHz.

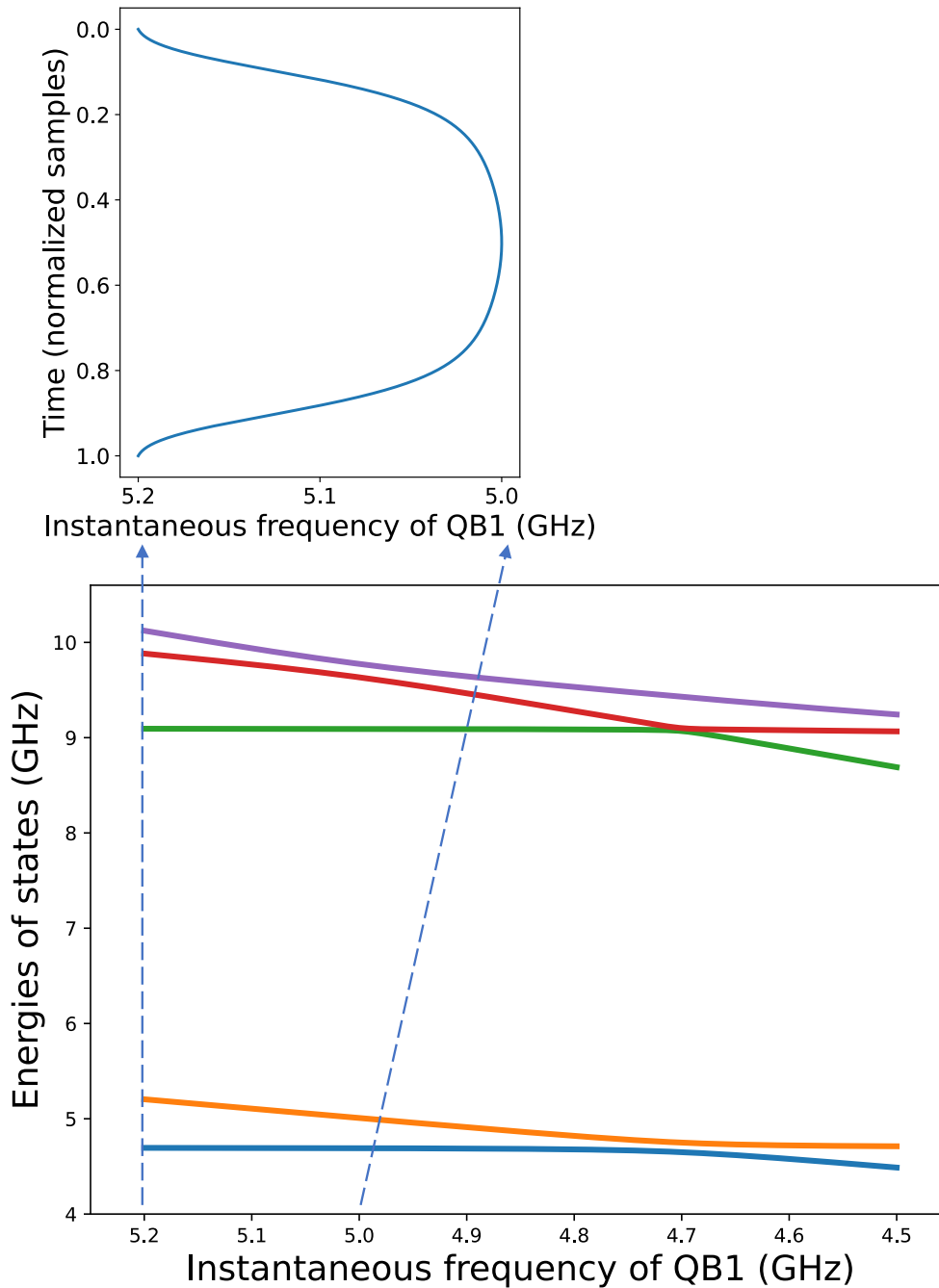


Figure 6-2: Energy spectrum diagram of two coupled transmons as depicted in Figure 6-1 as the frequency of QB1 is detuned by changing the local magnetic flux that threads its SQUID loop. The avoided crossing between the states  $|11\rangle$  and  $|20\rangle$  is used to implement the CPHASE gate. The upper plot shows an example of a Slepian-based pulse to vary  $\omega_1$  from  $\omega_1 = 5.2$  GHz to  $\omega_1 = 5.0$  GHz and then back to  $\omega_1 = 5.2$  GHz.

The procedure of our simulation is as follows:

1. Choose different control trajectories  $g_i[n]$  to compare.
2. Compute the corresponding control pulse  $\varepsilon_i[n]$  for each  $g_i[n]$  and use  $\varepsilon_i[n]$  as a control pulse to detune  $\omega_1$ .
3. For each control pulse  $\varepsilon_i[n]$ , scale  $\varepsilon_i[n]$  linearly in terms of duration and amplitude, and simulate a CPHASE gate for each duration and amplitude. Calculate the phase accumulation and leakage error as a function of duration and amplitude.
4. Collect the duration and amplitude pairs that obtain a phase accumulation  $\phi = \pi$ . Determine the corresponding leakage error as a function of duration.

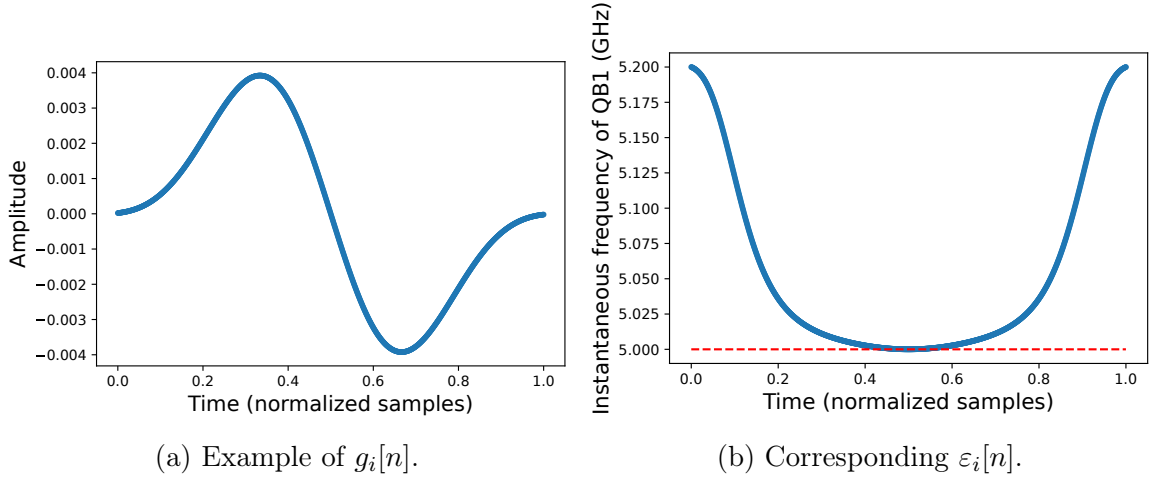


Figure 6-3: (a) An example of  $g_i[n]$  and (b) the corresponding  $\varepsilon_i[n]$  based on a second Slepian trajectory. In simulation,  $\varepsilon_i[n]$  and its linearly scaled versions indicate how the frequency detuning of QB1 varies through time, as shown in Figure 6-2.

There are a few subtleties in our simulation to mention, which are as follows:

1. In our simulation, we assume a design process mindset. In particular, we try to answer the question: given a control trajectory and some leakage error threshold, can we design another control trajectory that is shorter in duration while satisfying the given leakage error threshold. We will focus on comparing the

Chebyshev trajectory II and the second Slepian trajectory. We choose a specific trajectory from each family based on the two sidelobe matching strategies as discussed in Section 5.2.2.

2. To compute  $\varepsilon_i[n]$ , we first integrate  $g_i[n]$  to obtain  $\theta_i[n]$  and then calculate  $\varepsilon_i[n] = \Delta / \tan \theta_i[n]$ .
3. To scale  $\varepsilon_i[n]$ , we first obtain an interpolated function of  $\varepsilon_i[n]$  denoted as  $\varepsilon_i(t)$ . To scale linearly in duration, we perform  $\varepsilon_i(t/t_d)$  where  $t_d$  is the desired duration. To scale linearly in amplitude, we perform  $A\varepsilon_i(t)$  where  $A$  is the desired amplitude.
4. An example of implementing the control pulse to detune  $\omega_1$  is illustrated in Figure 6-2 and Figure 6-3.
5. We concentrate on the CZ gate in our simulation and require a suitable amplitude chosen so that a phase accumulation is  $\phi = \pi + 2k\pi$  with  $k = 0$ . In other words, we specifically focus on cases where the phase accumulation reaches  $\pi$  for the first time. This can be achieved by scanning the duration and amplitude of the control pulse in some range and selecting the suitable parameters.
6. Because the initial point when  $\omega_1 = 5.2$  GHz is not infinitely far away from the avoided crossing, state  $|11\rangle$  will suffer from the always-on  $z \otimes z$  interaction and accumulate an idling phase even though no control is applied. We will subtract the idling phase from the total phase accumulation in order to manifest the effect of the control pulse  $\varepsilon_i[n]$ .

## 6.2 Simulation results

We will show comparisons of multiple Chebyshev trajectories II  $g_{\text{ch2}}[n]$  against a second Slepian trajectory  $g_{\text{sl2}}[n]$  specified arbitrarily, whose time-domain and frequency-domain representations are shown in Figure 6-4. We specify  $g_{\text{sl2}}[n]$  in the Python function “`scipy.signal.windows.dpss()`” using the standardized half bandwidth  $NW = 3.15$

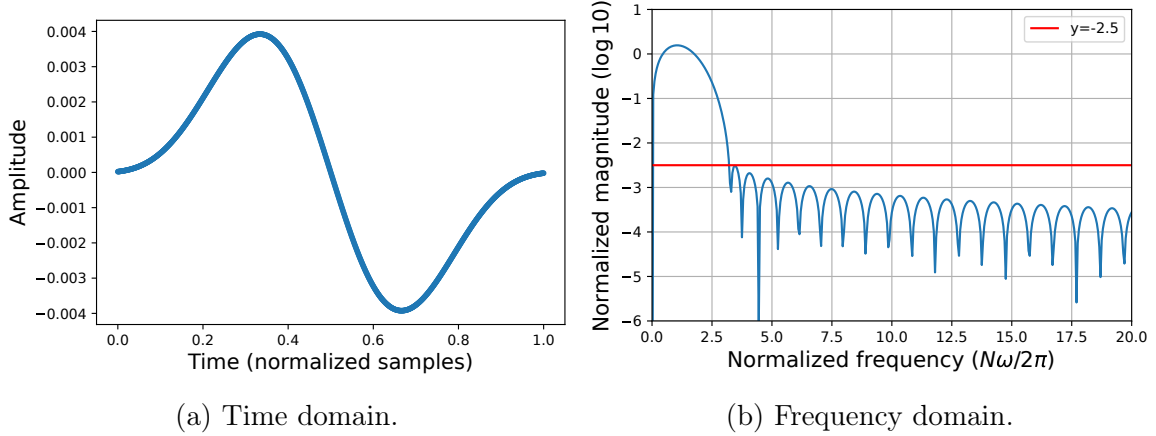


Figure 6-4: (a) Time-domain and (b) frequency-domain representations of the specified second Slepian trajectory  $g_{sl2}[n]$ . The red horizontal line  $y = -2.5$  in (b) indicates the first sidelobe amplitude of the specified second Slepian trajectory.

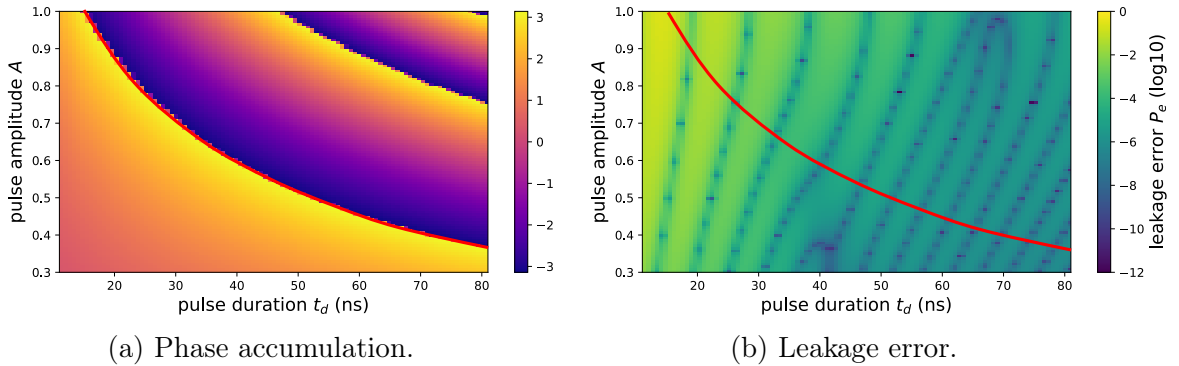


Figure 6-5: Simulation results of (a) phase accumulation  $\phi$  and (b) leakage error  $P_e$  as a function of control pulse duration  $t_d$  and amplitude  $A$  using the specified second Slepian trajectory  $g_{sl2}[n]$ . The red curve in (a) indicates the data points where the phase accumulation reaches  $\pi$  for the first time. The red curve in (b) indicates the corresponding leakage error data points.

and pulse length  $N = 1001$ . The Chebyshev trajectories II are chosen to match different sidelobe amplitudes of the specified second Slepian trajectory.

Figure 6-5 presents the phase accumulation and leakage error as a function of the control pulse duration  $t_d$  and amplitude  $A$  using  $g_{sl2}[n]$  as shown in Figure 6-4a. Following the procedure in Section 6.1, we first find out all the amplitude and duration pairs that result in the phase accumulation  $\phi = \pi$  described by the red curve in Figure 6-5a. Then we determine the corresponding leakage error data points

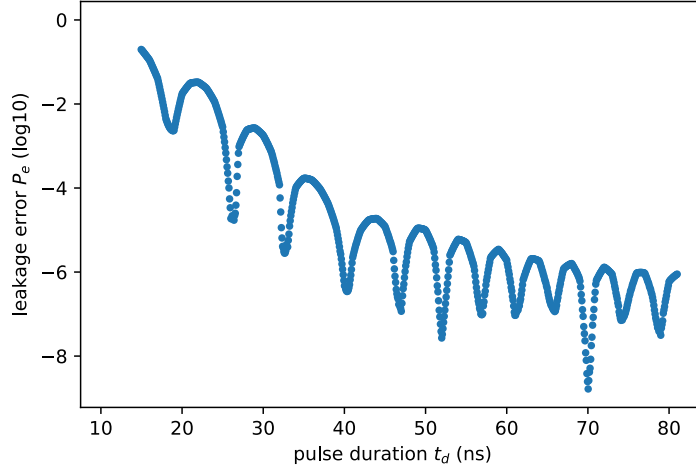


Figure 6-6: Leakage error  $P_e$  as a function of pulse duration  $t_d$  with phase accumulation of  $\phi = \pi$ .

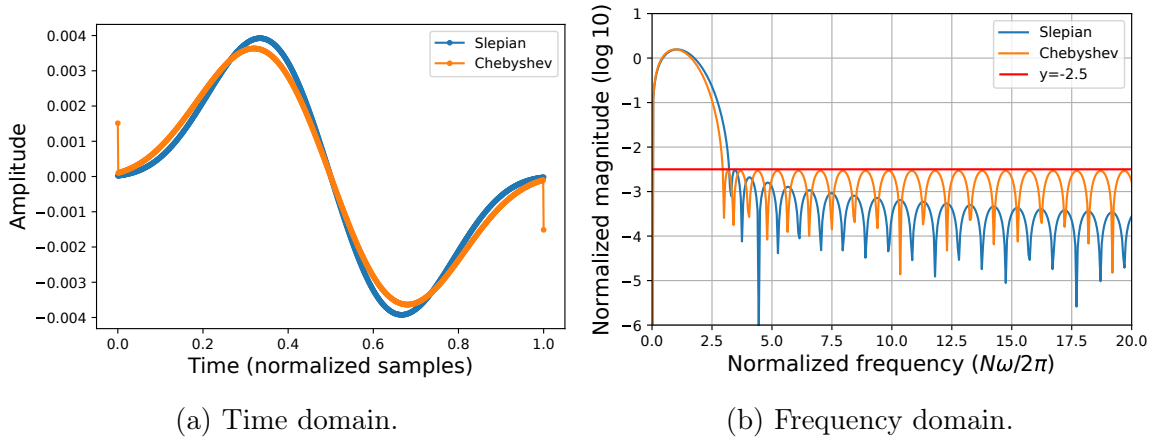


Figure 6-7: Comparison example 1. (a) Time-domain and (b) frequency-domain representations of the chosen Chebyshev trajectory II  $g_{\text{ch2}}[n]$  compared with the specified second Slepian trajectory  $g_{\text{sl2}}[n]$ .  $g_{\text{ch2}}[n]$  is chosen for its sidelobe amplitude to match the first sidelobe amplitude of  $g_{\text{sl2}}[n]$ . The red horizontal line in (b) indicates a given threshold  $\gamma = 10^{-2.5} \approx 0.32\%$ .

described by the same red curve in Figure 6-5b. We plot the corresponding leakage error  $P_e$  as a function of pulse duration  $t_d$  in Figure 6-6. Note that for pulse duration  $t_d \in [11.0, 14.9]$  the leakage error is invalid. This is because we constrain the pulse amplitude  $A$  to be  $A \leq 1$ , i.e., no further than exactly the avoided crossing, and therefore it is impossible for such a short pulse to obtain a phase accumulation of  $\phi = \pi$ .

### 6.2.1 Comparison example 1

In this comparison, we specifically choose a Chebyshev trajectory II  $g_{\text{ch2}}[n]$  so that its sidelobe amplitude matches the first sidelobe amplitude of the specified  $g_{\text{sl2}}[n]$  and is equal to the given threshold  $\gamma = 10^{-2.5} \approx 0.32\%$ . Note that here the error threshold  $\gamma$  is an indicator of the true leakage error for comparison, but the value of  $\gamma$  is not quite meaningful. The comparison of time-domain and frequency-domain representations are shown in Figure 6-7. In Figure 6-7a we note that the Chebyshev trajectory II  $g_{\text{ch2}}[n]$  has two impulses at the initial and last point. This is in fact a feature of the Chebyshev trajectories that partially contributes to equiripple sidelobes. As we will show in the following comparison examples, when the sidelobe amplitude of the Chebyshev trajectory II  $g_{\text{ch2}}[n]$  is specified to be smaller, the amplitude of the impulses at both ends will approximately align with their neighboring points.

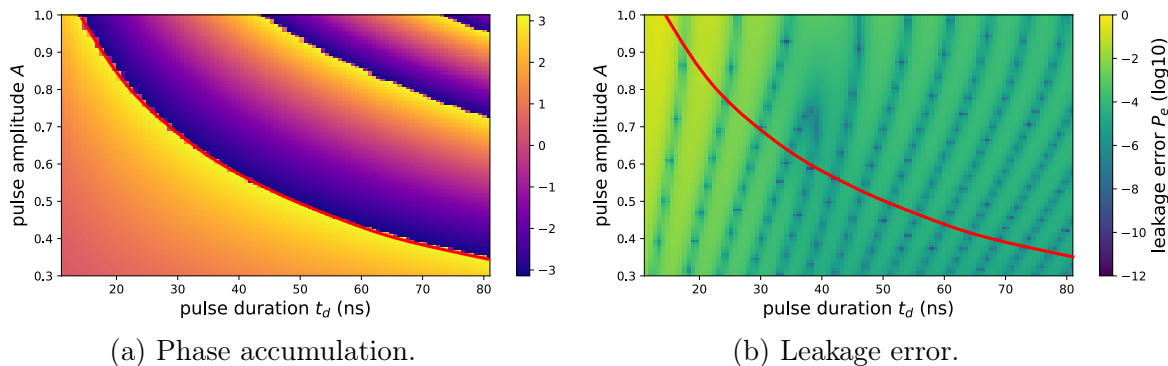


Figure 6-8: Comparison example 1. Simulation results of (a) phase accumulation  $\phi$  and (b) leakage error  $P_e$  as a function of control pulse duration  $t_d$  and amplitude  $A$  using the chosen Chebyshev trajectory II  $g_{\text{ch2}}[n]$ .

Figure 6-8 presents the phase accumulation and leakage error for a range of control pulse durations and amplitudes using  $g_{\text{ch2}}[n]$  as shown in Figure 6-7. We follow the procedure described in Section 6.1 and show the corresponding leakage error  $P_e$  as a function of the control pulse duration  $t_d$  in Figure 6-9. Note that the implicit variable here is the amplitude of the control pulse, which ensures a phase accumulation of  $\phi = \pi$ . As we observe in Figure 6-9, if the desired leakage error threshold is set to be  $P_e = 10^{-4.1} \approx 0.008\%$  as indicated by the horizontal red line, we find that the

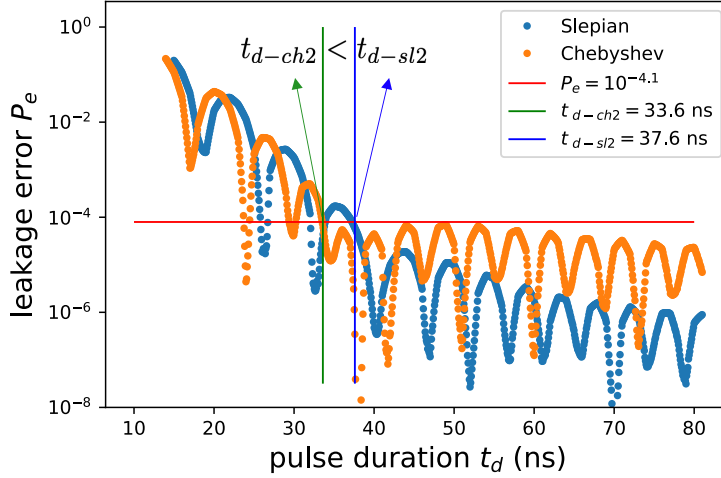


Figure 6-9: Comparison example 1. Leakage error  $P_e$  as a function of pulse duration  $t_d$  with phase accumulation of  $\phi = \pi$ . For leakage error threshold  $P_e = 10^{-4.1} \approx 0.008\%$ , we find that  $t_{d-\text{ch2}} = 33.6 \text{ ns} < t_{d-\text{sl2}} = 37.6 \text{ ns}$ .

smallest control pulse duration  $t_d$  for the two control trajectories are  $t_{d-\text{ch2}} = 33.6 \text{ ns}$  and  $t_{d-\text{sl2}} = 37.6 \text{ ns}$ .  $g_{\text{ch2}}[n]$  achieves a shorter duration than  $g_{\text{sl2}}[n]$  while satisfying the given leakage error threshold.

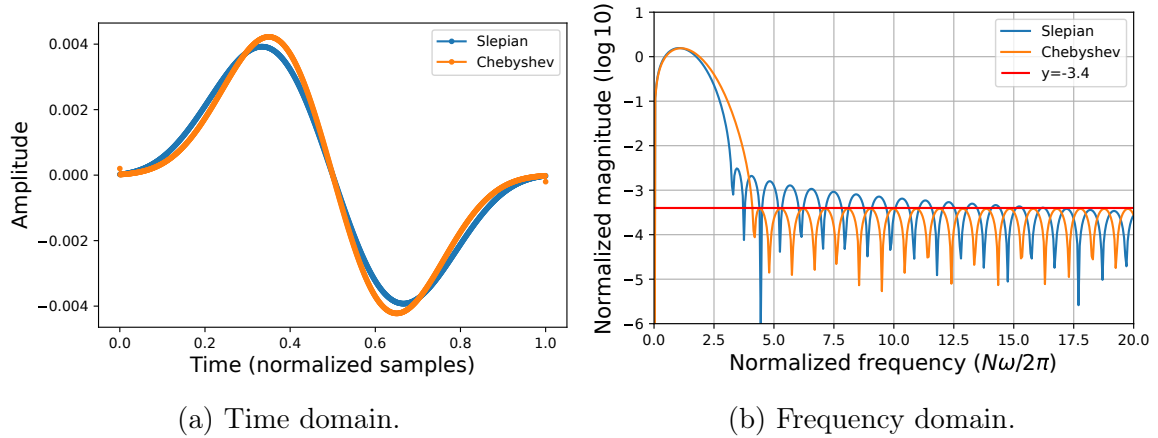


Figure 6-10: Comparison example 2. (a) Time-domain and (b) frequency-domain representations of the chosen Chebyshev trajectory II  $g_{\text{ch2}}[n]$  compared with the specified second Slepian trajectory  $g_{\text{sl2}}[n]$ .  $g_{\text{ch2}}[n]$  is chosen for its sidelobe amplitude to match the 16th sidelobe amplitude of  $g_{\text{sl2}}[n]$ . The red horizontal line in (b) indicates a given threshold  $\gamma = 10^{-3.4} \approx 0.04\%$ .

## 6.2.2 Comparison example 2

In this comparison, we perform the simulation following the same protocols. However, we utilize a different Chebyshev trajectory II  $g_{\text{ch2}}[n]$ , which is chosen so that the sidelobe amplitude of  $g_{\text{ch2}}[n]$  matches the 16th sidelobe of the specified second Slepian trajectory  $g_{\text{sl2}}[n]$ . The comparison of time-domain and frequency-domain representations are shown in Figure 6-10. Figure 6-11 presents the leakage error and phase accumulation for a range of control pulse durations and amplitudes utilizing the  $g_{\text{ch2}}[n]$ . Figure 6-12 shows the leakage error  $P_e$  as a function of the control pulse duration  $t_d$  where the phase accumulation of  $\phi = \pi$  is obtained. If the leakage error threshold is specified to be  $P_e = 10^{-5.8} \approx 0.00016\%$  as indicated by the horizontal red line in Figure 6-12, we find that the shortest control pulse duration for  $g_{\text{ch2}}[n]$  is significantly smaller than that of  $g_{\text{sl2}}[n]$ . To be more specific,  $t_{d-\text{ch2}} = 50.6 \text{ ns} < t_{d-\text{sl2}} = 68.5 \text{ ns}$ .

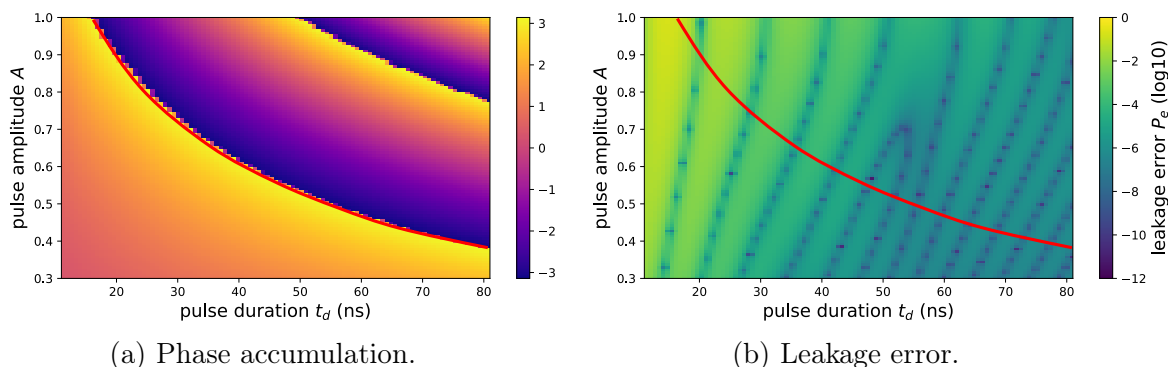


Figure 6-11: Comparison example 2. Simulation results of (a) phase accumulation  $\phi$  and (b) leakage error  $P_e$  as a function of control pulse duration  $t_d$  and amplitude  $A$  using the chosen Chebyshev trajectory II  $g_{\text{ch2}}[n]$ .

## 6.2.3 More comparison examples

We perform more comparisons by changing how the sidelobe amplitude of the Chebyshev trajectories II matches that of the second Slepian trajectory. Comparison example 1 in Section 6.2.1 and comparison example 2 in Section 6.2.2 are the two extreme examples in our consideration. The other comparison examples are such

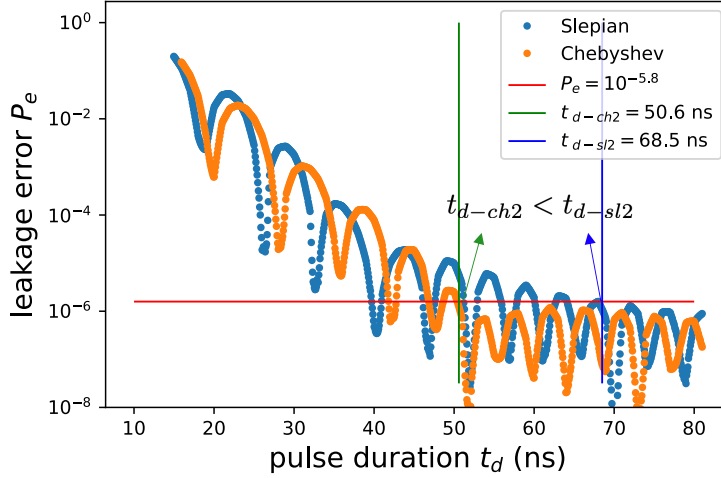


Figure 6-12: Comparison example 2. Leakage error  $P_e$  as a function of pulse duration  $t_d$  with phase accumulation of  $\phi = \pi$ . For leakage error threshold  $P_e = 10^{-5.8} \approx 0.00016\%$ , we find that  $t_{d\text{-ch}2} = 50.6 \text{ ns} < t_{d\text{-sl}2} = 68.5 \text{ ns}$ .

that the sidelobe amplitude of the Chebyshev trajectories II  $g_{\text{ch}2}[n]$  is matched to a sidelobe amplitude between the first and 16th sidelobe amplitude of the specified second Slepian trajectory  $g_{\text{sl}2}[n]$ . See Appendix A for more data details.

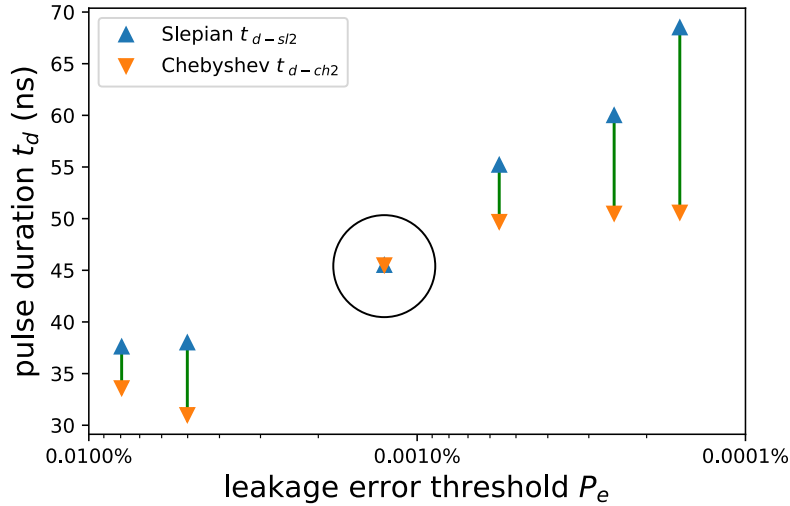


Figure 6-13: Comparisons of  $t_{d\text{-sl}2}$  and  $t_{d\text{-ch}2}$  for different leakage error thresholds  $P_e$  specified.

Figure 6-13 shows an aggregate of comparisons of  $t_{d\text{-ch}2}$  and  $t_{d\text{-sl}2}$  for different leakage error thresholds  $P_e$  specified in the examples shown in Section 6.2.1, 6.2.2

and Appendix A. We find that the Chebyshev trajectories II  $g_{\text{ch2}}[n]$  can be designed to achieve a shorter duration than the specified second Slepian trajectory  $g_{\text{sl2}}[n]$  for a range of leakage error thresholds, i.e.,  $t_{d-\text{ch2}} < t_{d-\text{sl2}}$ . The absolute value of the difference in between  $t_{d-\text{ch2}}$  and  $t_{d-\text{sl2}}$  varies depending on  $P_e$ . Note that for the threshold range around  $P_e \approx 0.001\%$ , which is indicated with a black circle in Figure 6-13, we find that  $t_{d-\text{ch2}}$  and  $t_{d-\text{sl2}}$  are approximately equal in order to satisfy the leakage error threshold.

### 6.3 Summary and discussion

In our simulation, we assume a design process mindset with the goal of designing a shorter control trajectory while satisfying a given leakage error threshold. Therefore, the comparison examples are chosen based on the question that, given some second Slepian trajectory and leakage error threshold, can the Chebyshev trajectory II be designed to be shorter in duration. The inference is that for a specified second Slepian trajectory and a given leakage error threshold, we can find a Chebyshev trajectory II with a shorter duration while satisfying the leakage error threshold in many cases, if not in all cases.

We discuss several limitations in our simulation results as follows:

1. There are some assumptions and approximations in deriving the formula for the leakage error in the abstracted two-level system. As discussed in the Landau-Zener example in Section 4.3.3, the formula derived for the leakage error can be used as an indicator for comparison between different control trajectories, but it is not exact. In our simulation, we first utilize the formula as a reference to determine which control trajectories to compare against and then perform the simulation. We find that the general trend of the simulation results agrees with the theoretical leakage error formula. However, the exact leakage error value and the corresponding shortest pulse duration are not consistent.
2. In the theoretical analysis in Chapter 5, we do not consider explicitly the phase

accumulation constraint of a CPHASE gate. In our simulation, the procedure requires that we choose the appropriate amplitude for the control pulse such that a phase accumulation of  $\phi = \pi$  is obtained. In fact, in order to acquire a phase accumulation of  $\phi = \pi$ , the returning point of the control trajectory is away from the avoided crossing in some cases where the pulse length is relatively large. Therefore, the advantage we observe in the simulation results may not be in agreement with what is predicted from the theoretical analysis.

3. We exclude interactions with higher energy levels when we consider a two-level abstraction of the system. In our simulation, we also consider a relatively simple model with two transmon qubits directly coupled by a capacitor, where interactions with higher energy levels are weak. In a more complicated system, the advantage of the Chebyshev trajectories could be impacted because of interactions with higher energy levels if such interactions are not negligible. One way around this issue is to deliberately choose appropriate operating regions so that higher energy levels are tuned away. Another way is to make further modifications to the trajectories based on more complicated physical models.

# Chapter 7

## Concluding Remarks and Future Work

In conclusion, the primary contribution of this thesis has three main parts. First of all, we formulate the problem of baseband flux control design of a CPHASE gate in superconducting circuits as a pulse design problem, and further as a control trajectory design problem. In this way, we are able to tackle the problem by taking advantage of expertise accumulated in other contexts of pulse design problems. Second, we propose the Chebyshev trajectory as an alternative to the widely used Slepian trajectory. We analytically show the advantage of the Chebyshev trajectory by using a two-level system abstraction. Finally, we compare the performance of the two types of trajectories by simulating a CZ gate in two capacitively coupled transmon qubits. Promising simulation results show that the Chebyshev trajectory can be designed to be shorter in duration while satisfying the same leakage error threshold in many cases. In other words, the Chebyshev trajectory can potentially enable faster CPHASE gates without sacrificing leakage error.

Looking forward, we would like to propose that the Chebyshev trajectory be considered in the context of a more widely used superconducting circuit scheme, i.e., two qubits coupled by a tunable coupler [40, 47]. Although the qubit-coupler-qubit scheme seems more complicated, it in fact provides more degrees of freedom to deconvolve and simplify the problem. In Chapter 6, we mentioned several limitations

in the simulation results, one of which is mainly due to the fact that the amplitude of the control pulse needs to be adjusted to obtain the desired phase accumulation. However, in the qubit-coupler-qubit scheme, we can design the operation parameters so that the phase accumulation is mainly dependent on the pulse of one of the qubits, while the leakage error is mainly dependent on the pulse of the coupler. Therefore, the dependence of phase accumulation and leakage error can be largely deconvolved, and the advantage of the Chebyshev trajectory is expected to manifest more readily.

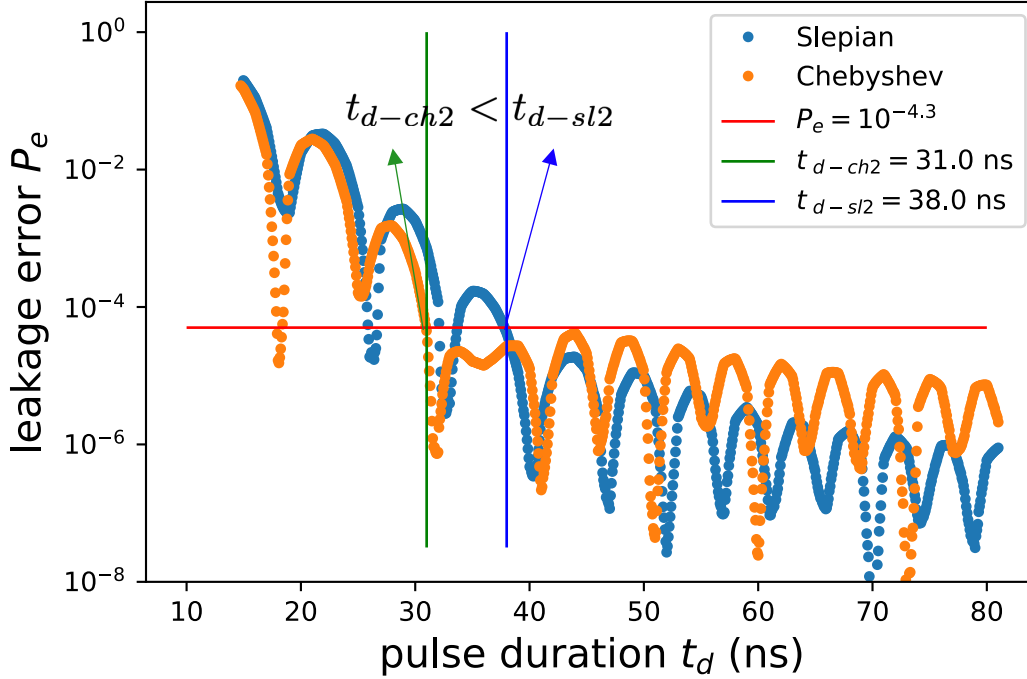
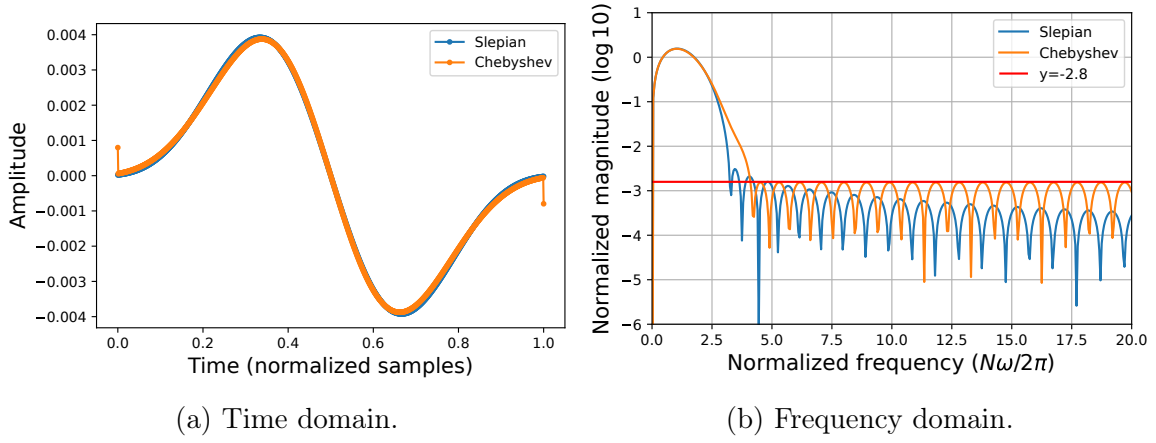
Furthermore, the methodology and perspectives in this thesis could potentially be employed in other pulse design problems in implementing quantum gates in superconducting circuits. Many desired characteristics, such as high fidelity and fast speed, of baseband flux-based gates in superconducting circuits depend largely on the design of the flux pulse. The weighted Chebyshev approximation is a generic method developed for designing pulses with specifications of interest. In this way, the methodology we take in this thesis could be modified to fit in the scenario of various control pulse design problems, thus serving as a step towards a systematic approach.

# Appendix A

## Additional Simulation Results

In this Appendix, we show more simulation results when matching the sidelobe amplitude of the Chebyshev trajectories II  $g_{\text{ch2}}[n]$  to different sidelobe amplitudes of the specified second Slepian trajectory  $g_{\text{sl2}}[n]$ . We follow the same data analysis procedure as discussed in Chapter 6. The chosen different sidelobe amplitudes of  $g_{\text{ch2}}[n]$  are in descending order as the example index number increases.

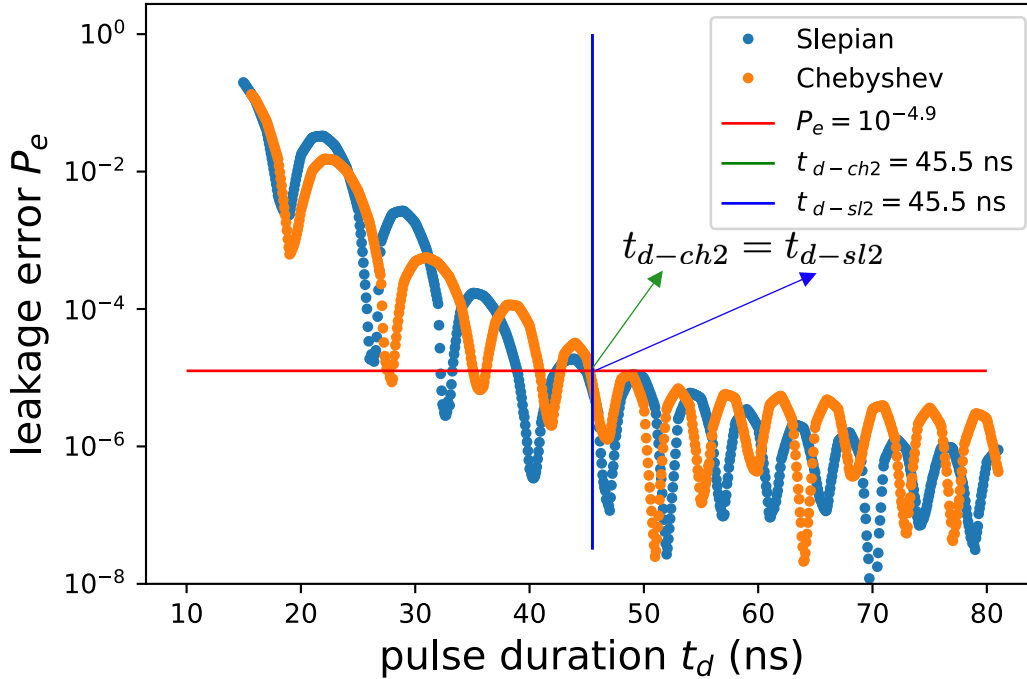
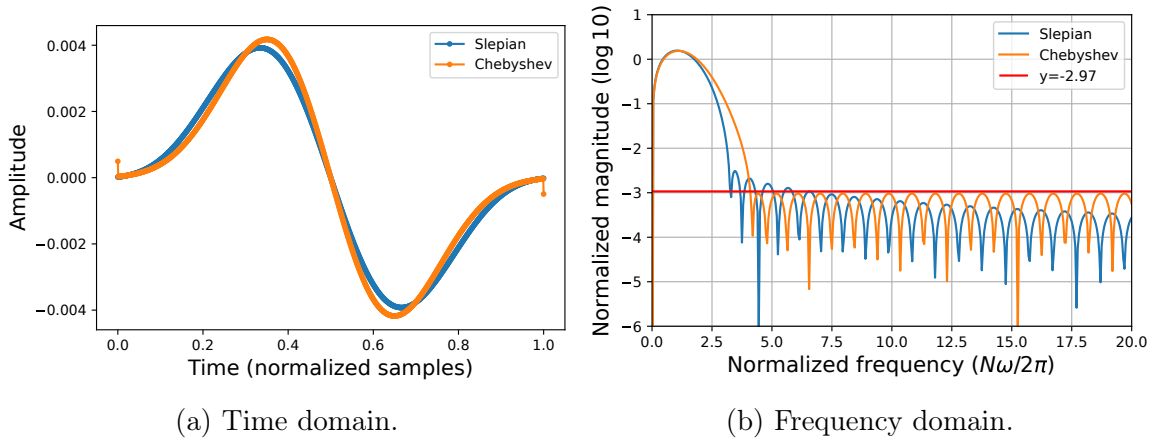
## Example 1



(c) Leakage error  $P_e$ .

Figure A-1: Example 1. (a) Time-domain and (b) frequency-domain representations of the chosen Chebyshev trajectory II  $g_{ch2}[n]$  compared with the specified second Slepian trajectory  $g_{sl2}[n]$ .  $g_{ch2}[n]$  is chosen for its sidelobe amplitude to match the 3rd sidelobe amplitude of  $g_{sl2}[n]$ . The red horizontal line in (b) indicates a given threshold  $\gamma = 10^{-2.8} \approx 0.16\%$ . (c) Leakage error  $P_e$  as a function of pulse duration  $t_d$  with phase accumulation of  $\phi = \pi$ . For leakage error threshold  $P_e = 10^{-4.3} \approx 0.005\%$ , we find that  $t_{d-ch2} = 31.0$  ns  $<$   $t_{d-sl2} = 38.0$  ns.

## Example 2



(c) Leakage error  $P_e$ .

Figure A-2: Example 2. (a) Time-domain and (b) frequency-domain representations of the chosen Chebyshev trajectory II  $g_{ch2}[n]$  compared with the specified second Slepian trajectory  $g_{sl2}[n]$ .  $g_{ch2}[n]$  is chosen for its sidelobe amplitude to match the 6th sidelobe amplitude of  $g_{sl2}[n]$ . The red horizontal line in (b) indicates a given threshold  $\gamma = 10^{-2.97} \approx 0.11\%$ . (c) Leakage error  $P_e$  as a function of pulse duration  $t_d$  with phase accumulation of  $\phi = \pi$ . For leakage error threshold  $P_e = 10^{-4.9} \approx 0.0013\%$ , we find that  $t_{d-ch2} = 45.5$  ns =  $t_{d-sl2} = 45.5$  ns.

### Example 3

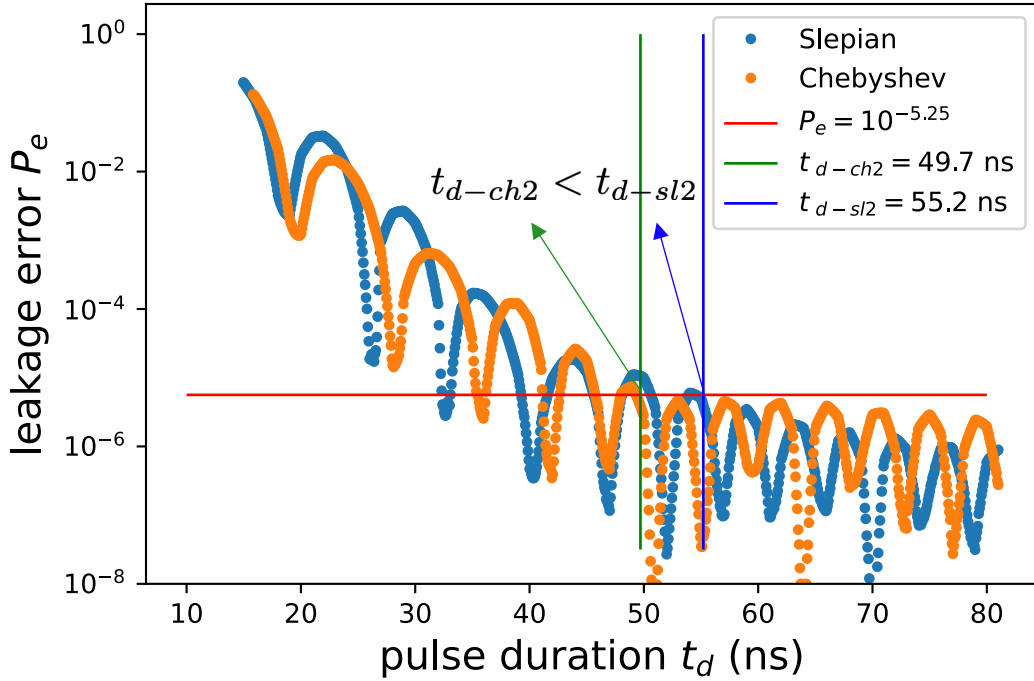
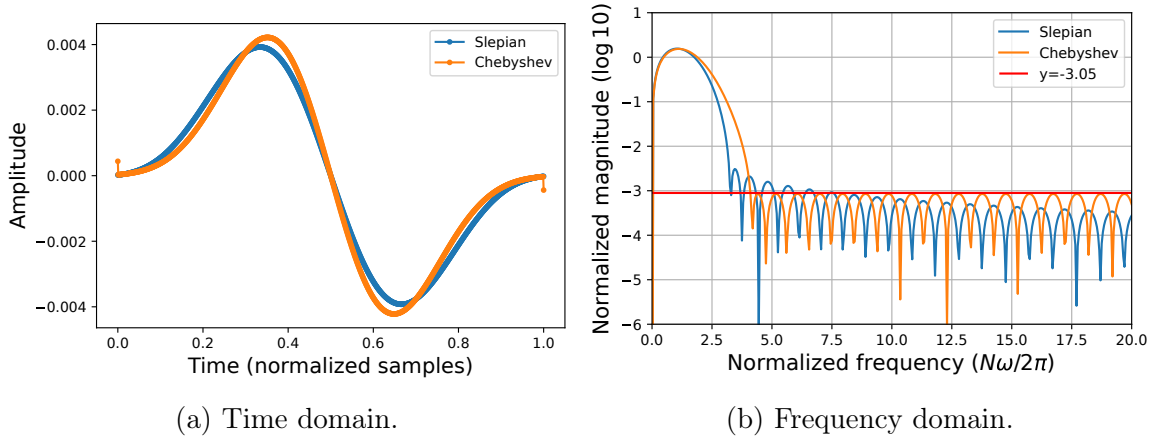
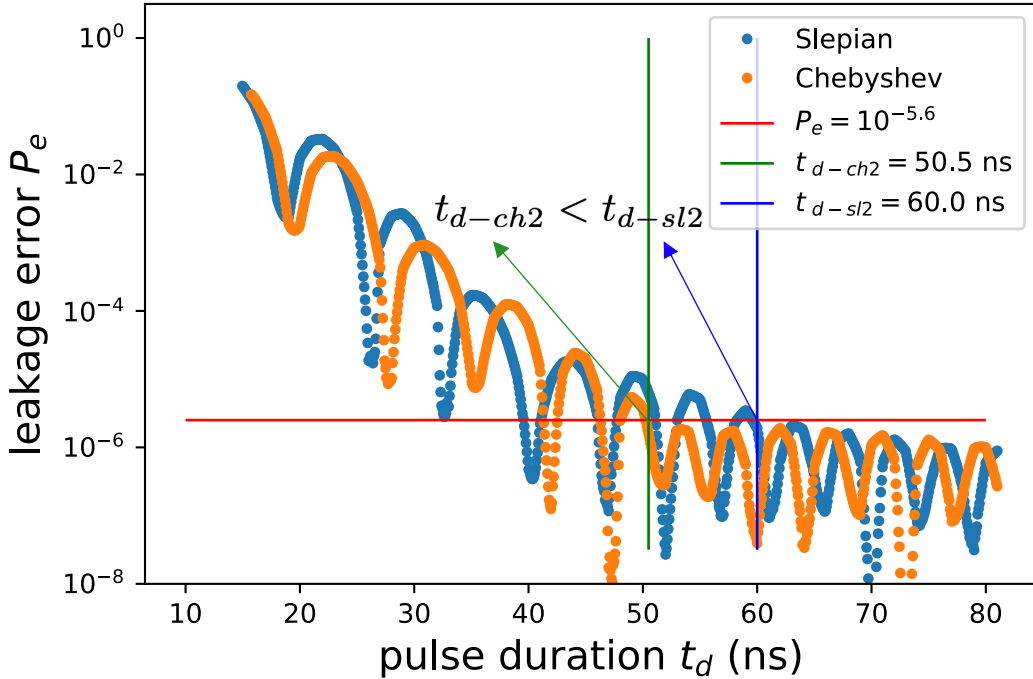
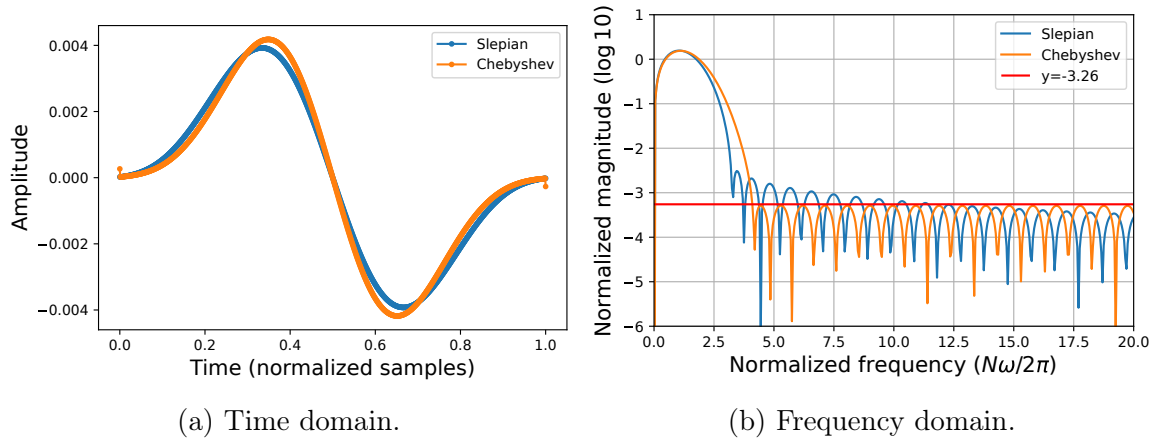


Figure A-3: Example 3. (a) Time-domain and (b) frequency-domain representations of the chosen Chebyshev trajectory II  $g_{ch2}[n]$  compared with the specified second Slepian trajectory  $g_{sl2}[n]$ .  $g_{ch2}[n]$  is chosen for its sidelobe amplitude to match the 7th sidelobe amplitude of  $g_{sl2}[n]$ . The red horizontal line in (b) indicates a given threshold  $\gamma = 10^{-3.05} \approx 0.089\%$ . (c) Leakage error  $P_e$  as a function of pulse duration  $t_d$  with phase accumulation of  $\phi = \pi$ . For leakage error threshold  $P_e = 10^{-5.25} \approx 0.00056\%$ , we find that  $t_{d-ch2} = 49.7 \text{ ns} < t_{d-sl2} = 55.2 \text{ ns}$ .

### Example 4



(c) Leakage error  $P_e$ .

Figure A-4: Example 4. (a) Time-domain and (b) frequency-domain representations of the chosen Chebyshev trajectory II  $g_{ch2}[n]$  compared with the specified second Slepian trajectory  $g_{sl2}[n]$ .  $g_{ch2}[n]$  is chosen for its sidelobe amplitude to match the 12th sidelobe amplitude of  $g_{sl2}[n]$ . The red horizontal line in (b) indicates a given threshold  $\gamma = 10^{-3.26} \approx 0.055\%$ . (c) Leakage error  $P_e$  as a function of pulse duration  $t_d$  with phase accumulation of  $\phi = \pi$ . For leakage error threshold  $P_e = 10^{-5.6} \approx 0.00025\%$ , we find that  $t_{d-ch2} = 50.5$  ns  $<$   $t_{d-sl2} = 60.0$  ns.

# Bibliography

- [1] R. P. Feynman, “Simulating physics with computers,” *International Journal of Theoretical Physics*, vol. 21, pp. 467–488, Jun. 1982.
- [2] J. J. Robinson, “On the hamiltonian game (a traveling salesman problem),” *RAND Research Memorandum RM 303*, 1949.
- [3] “IBM Unveils 400 Qubit-Plus Quantum Processor and Next-Generation IBM Quantum System Two.” <https://newsroom.ibm.com/2022-11-09-IBM-Unveils-400-Qubit-Plus-Quantum-Processor-and-Next-Generation-IBM-Quantum-System-Two>, Nov. 2022.
- [4] F. Arute, K. Arya, R. Babbush, D. Bacon, J. C. Bardin, R. Barends, R. Biswas, S. Boixo, F. G. S. L. Brandao, D. A. Buell, B. Burkett, Y. Chen, Z. Chen, B. Chiaro, R. Collins, W. Courtney, A. Dunsworth, E. Farhi, B. Foxen, A. Fowler, C. Gidney, M. Giustina, R. Graff, K. Guerin, S. Habegger, M. P. Harrigan, M. J. Hartmann, A. Ho, M. Hoffmann, T. Huang, T. S. Humble, S. V. Isakov, E. Jeffrey, Z. Jiang, D. Kafri, K. Kechedzhi, J. Kelly, P. V. Klimov, S. Knysh, A. Korotkov, F. Kostritsa, D. Landhuis, M. Lindmark, E. Lucero, D. Lyakh, S. Mandrà, J. R. McClean, M. McEwen, A. Megrant, X. Mi, K. Michielsen, M. Mohseni, J. Mutus, O. Naaman, M. Neeley, C. Neill, M. Y. Niu, E. Ostby, A. Petukhov, J. C. Platt, C. Quintana, E. G. Rieffel, P. Roushan, N. C. Rubin, D. Sank, K. J. Satzinger, V. Smelyanskiy, K. J. Sung, M. D. Trevithick, A. Vainsencher, B. Villalonga, T. White, Z. J. Yao, P. Yeh, A. Zalcman, H. Neven, and J. M. Martinis, “Quantum supremacy using a programmable superconducting processor,” *Nature*, vol. 574, pp. 505–510, Oct. 2019.
- [5] H.-S. Zhong, Y.-H. Deng, J. Qin, H. Wang, M.-C. Chen, L.-C. Peng, Y.-H. Luo, D. Wu, S.-Q. Gong, H. Su, Y. Hu, P. Hu, X.-Y. Yang, W.-J. Zhang, H. Li, Y. Li, X. Jiang, L. Gan, G. Yang, L. You, Z. Wang, L. Li, N.-L. Liu, J. J. Renema, C.-Y. Lu, and J.-W. Pan, “Phase-programmable gaussian boson sampling using stimulated squeezed light,” *Phys. Rev. Lett.*, vol. 127, p. 180502, Oct. 2021.
- [6] A. Montanaro, “Quantum algorithms: an overview,” *npj Quantum Information*, vol. 2, pp. 1–8, Jan. 2016.
- [7] P. W. Shor, “Polynomial-Time Algorithms for Prime Factorization and Discrete Logarithms on a Quantum Computer,” *SIAM Journal on Computing*, vol. 26, pp. 1484–1509, Oct. 1997.

- [8] L. K. Grover, “A fast quantum mechanical algorithm for database search,” in *Proceedings of the twenty-eighth annual ACM symposium on Theory of Computing*, STOC '96, (New York, NY, USA), pp. 212–219, Association for Computing Machinery, Jul. 1996.
- [9] J. R. Johansson, P. D. Nation, and F. Nori, “QuTiP: An open-source Python framework for the dynamics of open quantum systems,” *Computer Physics Communications*, vol. 183, pp. 1760–1772, Aug. 2012.
- [10] J. R. Johansson, P. D. Nation, and F. Nori, “QuTiP 2: A Python framework for the dynamics of open quantum systems,” *Computer Physics Communications*, vol. 184, pp. 1234–1240, Apr. 2013.
- [11] A. V. Oppenheim and R. W. Schaffer, *Discrete-time signal processing*. Pearson, 2014.
- [12] D. Slepian and H. O. Pollak, “Prolate spheroidal wave functions, fourier analysis and uncertainty — I,” *The Bell System Technical Journal*, vol. 40, pp. 43–63, Jan. 1961.
- [13] W. Heisenberg., “The actual content of quantum theoretical kinematics and mechanics,” *Z. Phys.*, 43:172, 1927.
- [14] H. J. Landau and H. O. Pollak, “Prolate spheroidal wave functions, fourier analysis and uncertainty — II,” *The Bell System Technical Journal*, vol. 40, pp. 65–84, Jan. 1961.
- [15] H. J. Landau and H. O. Pollak, “Prolate spheroidal wave functions, fourier analysis and uncertainty — III: The dimension of the space of essentially time- and band-limited signals,” *The Bell System Technical Journal*, vol. 41, pp. 1295–1336, Jul. 1962.
- [16] D. Slepian, “Prolate spheroidal wave functions, Fourier analysis and uncertainty — IV: Extensions to many dimensions; generalized prolate spheroidal functions,” *The Bell System Technical Journal*, vol. 43, pp. 3009–3057, Nov. 1964.
- [17] D. Slepian, “Prolate spheroidal wave functions, fourier analysis, and uncertainty — V: the discrete case,” *The Bell System Technical Journal*, vol. 57, pp. 1371–1430, May 1978.
- [18] D. Slepian, “Some Comments on Fourier Analysis, Uncertainty and Modeling,” *SIAM Review*, vol. 25, no. 3, pp. 379–393, 1983.
- [19] F. F. Kuo and J. F. Kaiser, *System Analysis by Digital Computer*. Wiley, 1966.
- [20] J. F. Kaiser, “Nonrecursive digital filter design using the  $I_0 - \sinh$  window function,” *IEEE International Symposium on Circuits & Systems*, 1974.

- [21] C. Dolph, “A Current Distribution for Broadside Arrays Which Optimizes the Relationship between Beam Width and Side-Lobe Level,” *Proceedings of the IRE*, vol. 34, pp. 335–348, Jun. 1946.
- [22] T. Parks and J. McClellan, “Chebyshev Approximation for Nonrecursive Digital Filters with Linear Phase,” *IEEE Transactions on Circuit Theory*, vol. 19, pp. 189–194, Mar. 1972.
- [23] T. Parks and J. McClellan, “A program for the design of linear phase finite impulse response digital filters,” *IEEE Transactions on Audio and Electroacoustics*, vol. 20, pp. 195–199, Aug. 1972.
- [24] J. McClellan and T. Parks, “A unified approach to the design of optimum FIR linear-phase digital filters,” *IEEE Transactions on Circuit Theory*, vol. 20, pp. 697–701, Nov. 1973.
- [25] L. R. Rabiner and B. Gold, *Theory and Application of Digital Signal Processing*. Prentice-Hall, 1975.
- [26] P. A. M. Dirac, *The Principles of Quantum Mechanics*. International Series of Monographs on Physics, Oxford, New York: Oxford University Press, fourth edition, fourth edition ed., Feb. 1982.
- [27] M. A. Nielsen and I. L. Chuang, “Quantum Computation and Quantum Information: 10th Anniversary Edition,” Dec. 2010.
- [28] N. P. de Leon, K. M. Itoh, D. Kim, K. K. Mehta, T. E. Northup, H. Paik, B. S. Palmer, N. Samarth, S. Sangtawesin, and D. W. Steuerman, “Materials challenges and opportunities for quantum computing hardware,” *Science (New York, N.Y.)*, vol. 372, p. eabb2823, Apr. 2021.
- [29] C. Lanczos, *The Variational Principles of Mechanics*. Dover Publications, 2012.
- [30] P. Krantz, M. Kjaergaard, F. Yan, T. Orlando, S. Gustavsson, and W. Oliver, “A quantum engineer’s guide to superconducting qubits,” *Applied Physics Reviews*, vol. 6, p. 021318, Jun. 2019.
- [31] B. D. Josephson, “Possible new effects in superconductive tunnelling,” *Physics Letters*, vol. 1, pp. 251–253, Jul. 1962.
- [32] M. Tinkham, *Introduction to Superconductivity*. Courier Corporation, Jan. 2004.
- [33] J. Koch, T. M. Yu, J. Gambetta, A. A. Houck, D. I. Schuster, J. Majer, A. Blais, M. H. Devoret, S. M. Girvin, and R. J. Schoelkopf, “Charge-insensitive qubit design derived from the Cooper pair box,” *Physical Review A*, vol. 76, p. 042319, Oct. 2007.
- [34] A. Y. Kitaev, “Quantum computations: algorithms and error correction,” *Russian Mathematical Surveys*, vol. 52, p. 1191, Dec. 1997.

- [35] C. M. Dawson and M. A. Nielsen, “The Solovay-Kitaev algorithm,” *Quantum Information & Computation*, vol. 6, pp. 81–95, Jan. 2006.
- [36] J. M. Martinis and M. R. Geller, “Fast adiabatic qubit gates using only  $\sigma_z$  control,” *Physical Review A*, vol. 90, p. 022307, Aug. 2014.
- [37] R. Barends, J. Kelly, A. Megrant, A. Veitia, D. Sank, E. Jeffrey, T. C. White, J. Mutus, A. G. Fowler, B. Campbell, Y. Chen, Z. Chen, B. Chiaro, A. Dunsworth, C. Neill, P. O’Malley, P. Roushan, A. Vainsencher, J. Wenner, A. N. Korotkov, A. N. Cleland, and J. M. Martinis, “Superconducting quantum circuits at the surface code threshold for fault tolerance,” *Nature*, vol. 508, pp. 500–503, Apr. 2014.
- [38] M. A. Rol, F. Battistel, F. K. Malinowski, C. C. Bultink, B. M. Tarasinski, R. Vollmer, N. Haider, N. Muthusubramanian, A. Bruno, B. M. Terhal, and L. DiCarlo, “Fast, high-fidelity conditional-phase gate exploiting leakage interference in weakly anharmonic superconducting qubits,” *Phys. Rev. Lett.*, vol. 123, p. 120502, Sept. 2019.
- [39] V. Negîrneac, H. Ali, N. Muthusubramanian, F. Battistel, R. Sagastizabal, M. S. Moreira, J. F. Marques, W. J. Vlothuizen, M. Beekman, C. Zachariadis, N. Haider, A. Bruno, and L. DiCarlo, “High-fidelity controlled- $z$  gate with maximal intermediate leakage operating at the speed limit in a superconducting quantum processor,” *Phys. Rev. Lett.*, vol. 126, p. 220502, Jun. 2021.
- [40] Y. Sung, J. Braumüller, A. Vepsäläinen, B. Kannan, M. Kjaergaard, A. Greene, G. O. Samach, C. McNally, D. Kim, A. Melville, B. M. Niedzielski, M. E. Schwartz, J. L. Yoder, T. P. Orlando, S. Gustavsson, and W. D. Oliver, “Realization of high-fidelity CZ and ZZ-free iSWAP gates with a tunable coupler,” *Physical Review X*, vol. 11, p. 021058, Jun. 2021. arXiv: 2011.01261.
- [41] J. Chu and F. Yan, “Coupler-Assisted Controlled-Phase Gate with Enhanced Adiabaticity,” *Physical Review Applied*, vol. 16, p. 054020, Nov. 2021.
- [42] J. Kelly, R. Barends, B. Campbell, Y. Chen, Z. Chen, B. Chiaro, A. Dunsworth, A. G. Fowler, I.-C. Hoi, E. Jeffrey, A. Megrant, J. Mutus, C. Neill, P. J. J. O’Malley, C. Quintana, P. Roushan, D. Sank, A. Vainsencher, J. Wenner, T. C. White, A. N. Cleland, and J. M. Martinis, “Optimal quantum control using randomized benchmarking,” *Phys. Rev. Lett.*, vol. 112, p. 240504, Jun. 2014.
- [43] C. Zener, “Non-adiabatic crossing of energy levels,” *Proc. R. Soc. Lond. A* 137, 1932.
- [44] L. D. Landau, “Theory of energy transfer. II,” *Physikalische Zeitschrift der Sowjetunion*, 1932.
- [45] J. R. Rubbmark, M. M. Kash, M. G. Littman, and D. Kleppner, “Dynamical effects at avoided level crossings: A study of the Landau-Zener effect using Rydberg atoms,” *Physical Review A*, vol. 23, pp. 3107–3117, Jun. 1981.

- [46] P. Lynch, “The Dolph–Chebyshev Window: A Simple Optimal Filter,” *Monthly Weather Review*, vol. 125, pp. 655–660, Apr. 1997.
- [47] F. Yan, P. Krantz, Y. Sung, M. Kjaergaard, D. L. Campbell, T. P. Orlando, S. Gustavsson, and W. D. Oliver, “Tunable coupling scheme for implementing high-fidelity two-qubit gates,” *Phys. Rev. Appl.*, vol. 10, p. 054062, Nov. 2018.